

CMS Draft Analysis Note

The content of this note is intended for CMS internal use and distribution only

2015/10/02
Head Id: 286171
Archive Id: 305122
Archive Date: 2015/04/25
Archive Tag: trunk

Search for new diboson resonances in semileptonic and hadronic final states at $\text{sqrt}(s) = 13 \text{ TeV}$

Sudha Ahuja¹, Nural Akchurin¹¹, Thea Arrestad⁶, Luca Brianza⁴, Yu-Hsiang Chang⁷, Jordan Damgov¹¹, Phil Dudero¹¹, Maxime Gouzevitch³, Andreas Hinzmann⁶, Ji-Kong Huang⁷, Raman Khurana⁷, Ben Kilmister⁶, Clemens Lange⁶, Sung-Won Lee¹¹, Qiang Li², Yun-Ju Lu⁷, Petar Maksimovic⁹, Jennifer Ngadiuba⁶, Sergio Novaes¹, Alexandra Oliveira⁵, Maurizio Pierini¹², Salvatore Rappoccio¹⁰, José Ruiz¹, Thiago Tomei¹, Henry Yee-Shian Tong⁷, Nhan Tran⁸, Qun Wang², Mengmeng Wang², Jun-Yi Wu⁷, Zijun Xu², and Shin-Shan Eiko Yu⁷

¹ SPRACE-UNESP, São Paulo, Brazil

² Peking University, Beijing, China

³ University of Lyon, Lyon, France

⁴ INFN Sezione di Milano-Bicocca, University of Milano-Bicocca, Italy

⁵ INFN Sezione di Padova, University of Padova, Padova, Italy

⁶ University of Zurich, Zurich, Switzerland

⁷ National Central University, Chung-Li, Taiwan

⁸ Fermi National Accelerator Laboratory, Batavia, USA

⁹ Johns Hopkins University, Baltimore, USA

¹⁰ State University of New York at Buffalo, Buffalo, USA

¹¹ Texas Tech University, Lubbock, USA

¹² California Institute of Technology, Pasadena, USA

Abstract

In this Early Analysis document we discuss the preparation for the search for heavy BSM resonances in the VW, VZ and VV channels, where V stands for a hadronically-decaying W/Z boson. We use the standard reconstruction techniques for high pT leptons and jets with substructure. We recommission our frameworks from Run 1, and are able to run the three channels from preselection through optimisation and final limits. We are also able to combine the results from the different channels and also with the Run 1 data. We foresee to either have better limits than those obtained with Run 1 data with 3/fb of 13 TeV data, or a strong evidence of a BSM resonance.

This box is only visible in draft mode. Please make sure the values below make sense.

PDFAuthor:

Thiago R. F. P. Tomei

PDFTitle:

Search for new diboson resonances in semileptonic and hadronic final states
at $\sqrt{s} = 13$ TeV

PDFSubject:

CMS

PDFKeywords:

CMS, physics, software, computing

Please also verify that the abstract does not use any user defined symbols

DRAFT

1 Log of Changes of AN-15-037

- 2 • Version 0:** 2015-04-21, version delivered for reading by the EXOTICA conveners.

DRAFT

3 **Contents**

4	1	Introduction	3
5	2	CMS Detector	5
6	3	Samples	6
7	4	Trigger Criteria	7
8	4.1	Trigger criteria for VZ analysis	7
9	4.2	Trigger criteria for VW analysis	9
10	4.3	Trigger criteria for dijet analysis	11
11	5	Detector Objects and Boson Candidates	16
12	5.1	Electron Identification	16
13	5.2	Muon Reconstruction and Identification	17
14	5.3	Jet Identification and Substructure	21
15	5.4	B-tagging	22
16	5.5	Leptonic Z Candidate Reconstruction	23
17	5.6	Leptonic W Candidate Reconstruction	23
18	5.7	Hadronic V Candidate Reconstruction	23
19	6	Analysis Strategy	29
20	6.1	Strategy Overview	29
21	6.2	VZ channel Preselection	30
22	6.3	VW channel Preselection	35
23	6.4	Dijet channel Preselection	38
24	6.5	N-subjettiness Optimization	40
25	6.6	VZ channel Optimization and Final Selection	43
26	6.7	VW channel Optimization and Final Selection	44
27	6.8	Dijet channel Optimization and Final Selection	49
28	7	Theoretical Framework	55
29	7.1	Theory Context Overview	55
30	7.2	RS Graviton at 13 TeV	55
31	7.3	Bulk Graviton at 13 TeV	56
32	7.4	HVT Model at 13 TeV	57
33	8	Fits, Results and Strategy for Discovery	61
34	8.1	Background Estimation Overview	61
35	8.2	VZ Channel fits	64
36	8.3	VW Channel fits	67
37	8.4	Dijet Channel fits	71
38	8.5	Limits	72
39	8.6	Combination of Run2 data	80
40	8.7	Combination of Run1 and Run2 data	80
41	8.8	Strategy for Discovery	84
42	9	Conclusion and Outlook	90

43 1 Introduction

44 This note documents the LHC Run 2 Early Analysis (EA) efforts on the search for new reso-
 45 nances (X) that decay to a pair of vector bosons (V). The channels under investigation are $X \rightarrow$
 46 $VV \rightarrow \text{jet} + \text{jet}$, $X \rightarrow VW \rightarrow \text{jet} + \ell + E_T^{\text{miss}}$, and $X \rightarrow VZ \rightarrow \text{jet} + \ell\ell$. In all cases, at least one
 47 of the bosons decays hadronically, where the decay products are clustered in a single jet. This
 48 analysis is an continuation and improvement of the EXO-12-021 ($X \rightarrow VW \rightarrow \text{jet} + \ell + E_T^{\text{miss}}$),
 49 EXO-12-022 ($X \rightarrow VZ \rightarrow \text{jet} + \ell\ell$) and EXO-12-024 ($X \rightarrow VV \rightarrow \text{jet} + \text{jet}$) analyses that have
 50 previously been performed using collision data at a centre-of-mass energy of $\sqrt{s} = 8 \text{ TeV}$. The
 51 leptonic analysis were published together as EXO-13-009. No signal was observed.

52 There are several theory models that motivate the existence of heavy particles that decay to
 53 pairs of bosons. These models usually aim to explain open questions of the Standard Model
 54 (SM) such as the integration of gravity into the SM using extra dimensions. The aim of the
 55 analyses is to test a large set of different models and model parameters to make the results as
 56 useful as possible to the theory community. Among the models under scrutiny are the Randall-
 57 Sundrum Warped Extra Dimensions model [1, 2], and the bulk graviton model [3–5], which in
 58 particular yield differences in the polarisation of the produced vector bosons leading to differ-
 59 ent kinematic distributions. Another interesting model, which is tested by the analyses pre-
 60 sented here is the heavy vector triplet (HVT) model [6]. HVT generalises a large number of
 61 explicit models predicting spin-1 resonances, which can be described by a rather small set of
 62 parameters; therefore, it allows theorists to cast their particular models into a common frame-
 63 work.

64 The analyses are based on proton-proton collision data at $\sqrt{s} = 13 \text{ TeV}$ collected by the CMS
 65 experiment at the CERN Large Hadron Collider (LHC) during 2015 and corresponding to an
 66 integrated luminosity of 1 to 10 fb^{-1} . The signal studied in the analyses is the production of
 67 a resonance with mass above 0.8 TeV , decaying the final states listed above. No assumptions
 68 on additional particles produced in the final state are made. It is assumed that the resonance is
 69 narrow, i.e. that its natural width is much smaller than the experimental resolution.

70 The challenge of the analyses described here are the reconstruction of the highly energetic de-
 71 cay products. Since resonances under study have masses of $\mathcal{O}(\text{TeV})$, its decay products, i.e.
 72 the bosons, have on average transverse momenta of several hundred GeV and above. As a
 73 consequence, the particles emerging from the boson decays are very collimated. In particular,
 74 the decay products of the hadronically decaying bosons cannot be resolved anymore, but are
 75 instead reconstructed as a single jet object. Dedicated techniques are applied to exploit the
 76 substructure of this object. For the leptonic decays of the bosons, special high-momentum re-
 77 construction algorithms are employed. Additionally, isolation requirements are optimised in
 78 order to avoid efficiency losses when two leptons from a Z boson decay are very close to each
 79 other.

80 As for the Run 1 analysis, the Run 2 diboson analyses aim to reconstruct the full event in or-
 81 der to be able to search for a local enhancement in the diboson invariant mass spectrum. The
 82 hadronically decaying vector bosons are reconstructed using information from jet substructure
 83 to perform so-called jet “V tagging”. This also helps to suppress the SM background, which
 84 mainly originates from the production of $V + \text{jets}$ and non-resonant VV events. Leptonically
 85 decaying V bosons are reconstructed by identifying isolated high-momentum leptons (elec-
 86 trons or muons). In case of a W boson, the measured missing transverse energy (E_T^{miss}) in the
 87 event is used to estimate the neutrino. An estimate of the neutrino longitudinal momentum is
 88 derived by imposing the constraint of the W mass on the invariant mass of the $\ell\nu$ system. The
 89 background contributions after signal selection are estimated using a data-driven technique in

90 sidebands of the jet mass distribution of the reconstructed hadronic V boson candidates.
 91 The three analysis channels mentioned above are chosen for the LHC Run 2 Early Analysis
 92 campaign, since they promise highest sensitivity to new physics in diboson events already with
 93 comparably low statistics. They are the most robust ones with respect to object calibration and
 94 understanding with early data. The expected sensitivity of the different diboson analyses that
 95 have already been performed at a centre-of-mass energy of 8 TeV is shown in Fig. 1. In addition
 96 to the different W and Z boson final state combinations, also final states with Higgs bosons were
 97 analysed. These, however, require the use of b-tagging and τ identification, which will require
 98 more detailed studies and will therefore only be performed a few weeks later. Nevertheless, in
 99 contrast to the $\sqrt{s} = 8$ TeV approach, the Higgs signal region will be blinded already for the
 100 early VV analyses to allow combination with the later Higgs final state analyses.

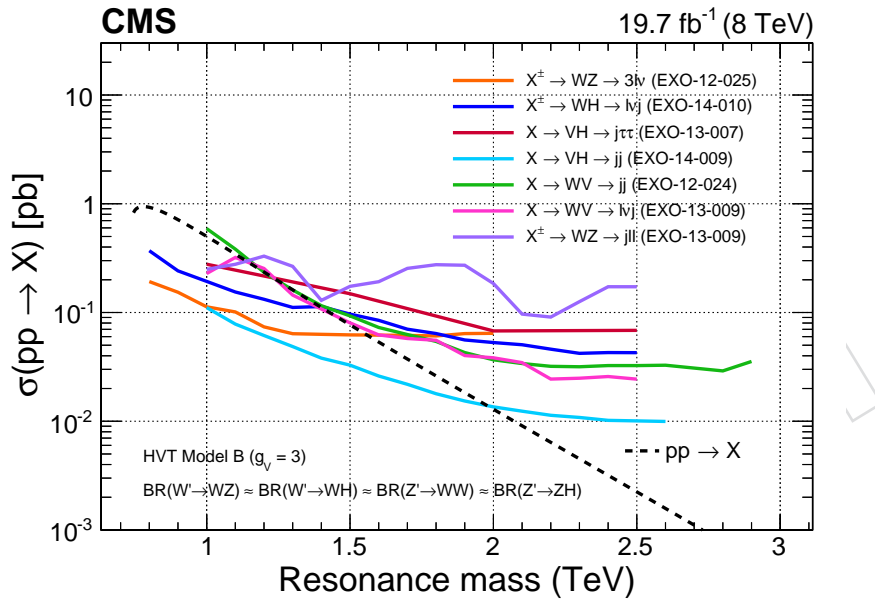


Figure 1: Comparison of the expected limits on the production cross section of a heavy resonance $X \sigma(pp \rightarrow X)$, as a function of the resonance mass in the HVT model for the different diboson analysis channels at a centre-of-mass energy of 8 TeV. For technical reasons, observed limits are shown for the WW and WZ semileptonic channels.

101 This note aims to give a full overview over the diboson resonance analysis strategy. In partic-
 102 ular, new studies performed so far and the differences to the Run 1 analyses are highlighted.
 103 The note is organised as follows. Section 2 contains a brief description of the CMS detector and
 104 in Section 3 the simulation samples used are summarised. Sections 4 and 5 describe the trigger
 105 and detector objects for the different analysis channels followed by the overall analysis strategy
 106 in Section 6. A brief account of the theoretical framework that supports these studies is given
 107 in Section 7. Finally, the results are given in Section 8 with conclusion and outlook in Section 9.

108 2 CMS Detector

109 The central feature of the CMS apparatus is a superconducting solenoid of 6 m internal diameter,
 110 providing a magnetic field of 3.8 T. Within the superconducting solenoid volume are a
 111 silicon pixel and strip tracker, a lead tungstate crystal electromagnetic calorimeter (ECAL), and
 112 a brass and scintillator hadron calorimeter (HCAL), each composed of a barrel and two endcap
 113 sections. Muons are measured in gas-ionization detectors embedded in the steel flux-return
 114 yoke outside the solenoid. Extensive forward calorimetry complements the coverage provided
 115 by the barrel and endcap detectors.

116 The particle-flow event algorithm reconstructs and identifies each individual particle with
 117 an optimized combination of information from the various elements of the CMS detector.
 118 The energy of photons is directly obtained from the ECAL measurement, corrected for zero-
 119 suppression effects. The energy of electrons is determined from a combination of the electron
 120 momentum at the primary interaction vertex as determined by the tracker, the energy of the
 121 corresponding ECAL cluster, and the energy sum of all bremsstrahlung photons spatially com-
 122 patible with originating from the electron track. The energy of muons is obtained from the
 123 curvature of the corresponding track. The energy of charged hadrons is determined from a
 124 combination of their momentum measured in the tracker and the matching ECAL and HCAL
 125 energy deposits, corrected for zero-suppression effects and for the response function of the
 126 calorimeters to hadronic showers. Finally, the energy of neutral hadrons is obtained from the
 127 corresponding corrected ECAL and HCAL energy.

128 Jet momentum is determined as the vectorial sum of all particle momenta in the jet, and is
 129 found from simulation to be within 5% to 10% of the true momentum over the whole p_T spec-
 130 trum and detector acceptance. An offset correction is applied to jet energies to take into account
 131 the contribution from additional proton-proton interactions within the same bunch crossing.
 132 Jet energy corrections are derived from simulation, and are confirmed with in situ measure-
 133 ments of the energy balance in dijet and photon+jet events. Additional selection criteria are
 134 applied to each event to remove spurious jet-like features originating from isolated noise pat-
 135 terns in certain HCAL regions.

136 Muons are measured in the pseudorapidity range $|\eta| < 2.4$, with detection planes made using
 137 three technologies: drift tubes, cathode strip chambers, and resistive plate chambers. Matching
 138 muons to tracks measured in the silicon tracker results in a relative transverse momentum
 139 resolution for muons with $20 < p_T < 100$ GeV of 1.3–2.0% in the barrel and better than 6% in
 140 the endcaps. The p_T resolution in the barrel is better than 10% for muons with p_T up to 1 TeV.

141 Electrons are measured in the electromagnetic calorimeter, in the pseudorapidity range $|\eta| <$
 142 2.5. The electron momentum is estimated by combining the energy measurement in the ECAL
 143 with the momentum measurement in the tracker. The momentum resolution for electrons with
 144 $p_T \approx 45$ GeV from $Z \rightarrow ee$ decays ranges from 1.7% for nonshowering electrons in the barrel
 145 region to 4.5% for showering electrons in the endcaps.

146 A more detailed description of the CMS detector, together with a definition of the coordinate
 147 system used and the relevant kinematic variables, can be found in Ref. [7].

148 3 Samples

149 All studies described in this Note use the Phys14 exercise samples, unless explicitly indicated.
 150 Those samples were a re-reconstruction of the Fall13 GEN-SIM samples, originally
 151 produced with CMSSW_6_2_X. This re-reconstruction was done with CMSSW_7_2_0. The
 152 samples were used in the MINIAODSIM format, which is proposed to become the standard
 153 format for physics analyses in Run 2. Some private background and signal samples were also
 154 produced, both to test the group's capability to produce those samples if need be, as well as
 155 cover some samples which were not originally requested in PHYS14. All the samples were
 156 produced aiming for the "intermediate" configuration for Run 2: 25ns operation and pileup
 157 20, corresponding to an instantaneous luminosity $\mathcal{L} = 7 \times 10^{33} \text{ cm}^{-2} \text{ s}^{-1}$. We considered almost
 158 all relevant SM backgrounds – QCD multijets, inclusive W and DY production, $t\bar{t}$ and single
 159 top production, and WW non-resonant production. For the signal samples, we considered
 160 primarily RS Graviton samples.

Table 1: Hadronic samples.

Sample name	Cross section[pb]	N _{events}
/QCD_HT_250To500_13TeV-madgraph/	6.705E5	663953
/QCD_HT_250To500_13TeV-madgraph/ (EXT)	6.705E5	2004219
/QCD_HT-500To1000_13TeV-madgraph/	2.674E4	849033
/QCD_HT-500To1000_13TeV-madgraph/ (EXT)	2.674E4	3214312
/QCD_HT_1000ToInf_13TeV-madgraph/	769.7	333733
/QCD_HT_1000ToInf_13TeV-madgraph/ (EXT)	769.7	1130720
/RSGravitonToWW_kMpl01_M_1000_Tune4C_13TeV_pythia8/	2.37	27614
/RSGravitonToWW_kMpl01_M_2000_Tune4C_13TeV_pythia8/	4.80E-2	39068
/RSGravitonToWW_kMpl01_M_3000_Tune4C_13TeV_pythia8/	2.92E-3	28983
/RSGravitonToWW_kMpl01_M_4000_Tune4C_13TeV_pythia8/	2.74E-4	28687

Table 2: VW semileptonic samples. Signal samples are the same as hadronic.

Sample name	Cross section[pb]	N _{events}
/WJetsToLNu_HT-100to200_Tune4C_13TeV-madgraph-tauola/	1817	5262265
/WJetsToLNu_HT-200to400_Tune4C_13TeV-madgraph-tauola/	471.6	4936077
/WJetsToLNu_HT-400to600_Tune4C_13TeV-madgraph-tauola/	55.61	4640594
/WJetsToLNu_HT-600toInf_Tune4C_13TeV-madgraph-tauola/	18.81	4581841
/WJetsToLNu_13TeV-madgraph-pythia8-tauola/	2.049E4	10017462
/TTJets_MSDecaysCKM_central_Tune4C_13TeV-madgraph-tauola/	831.76	25446880
/TToLeptons_s-channel-CSA14_Tune4C_13TeV-aMCatNLO-tauola/	7.2	500000
/TToLeptons_t-channel-CSA14_Tune4C_13TeV-aMCatNLO-tauola/	136.05	3991000
/T_tW-channel-DR_Tune4C_13TeV-CSA14-powheg-tauola/	35.6	986100
/TBarToLeptons_s-channel-CSA14_Tune4C_13TeV-aMCatNLO-tauola/	4.16	250000
/TBarToLeptons_t-channel_Tune4C_CS14_13TeV-aMCatNLO-tauola/	80.97	1999800
/Tbar_tW-channel-DR_Tune4C_13TeV-CSA14-powheg-tauola	35.6	971800
/LOWW-Ivjj-PTWgt180 (Private sample in prod/phys03)	0.29	19800

Table 3: VZ semileptonic samples.

Sample name	Cross section[pb]	N _{events}
/DYJetsToLL_M-50_HT-100to200_Tune4C_13TeV-madgraph-tauola/	194.3	4054159
/DYJetsToLL_M-50_HT-200to400_Tune4C_13TeV-madgraph-tauola/	52.24	4666496
/DYJetsToLL_M-50_HT-400to600_Tune4C_13TeV-madgraph-tauola/	6.546	4931372
/DYJetsToLL_M-50_HT-600toInf_Tune4C_13TeV-madgraph-tauola/	2.179	4493574
/RSGravitonToZZ_kMpl01_M_1000_Tune4C_13TeV_pythia8	1.202	30000
/RSGravitonToZZ_kMpl01_M_2000_Tune4C_13TeV_pythia8	2.284E-2	29744
/RSGravitonToZZ_kMpl01_M_3000_Tune4C_13TeV_pythia8	1.454E-3	29209
/RSGravitonToZZ_kMpl01_M_4000_Tune4C_13TeV_pythia8	1.357E-4	30000
/RSGravToZZ_kMpl01_M-4500_Tune4C_13TeV-pythia8	N/A	195818

161 4 Trigger Criteria

162 4.1 Trigger criteria for VZ analysis

163 Based on our studies, lowest threshold, un-prescaled and non-isolated double lepton triggers
 164 have been selected, as given below:

- 165 • HLT_DoubleEle33_CaloIdL_GsfTrkIdVL

166 for the SingleElectron dataset, and

- 167 • HLT_Mu30_TkMu11

168 for the SingleMuon dataset.

169 The triggers are present in the Phys14 samples listed in Section 3. The double lepton triggers
 170 have lower thresholds compared to single lepton ones, leading to our selection. Also of note
 171 is the fact that those paths are seeded by single-object L1 triggers, which should allow us to
 172 avoid inefficiencies coming from collimated leptons interfering with each other in the online
 173 selection.

174 Figure 2 (3) shows the double electron (muon) trigger efficiency curves for the RS Graviton
 175 signal as a function of: the electron (muon) p_T (for the leading and sub-leading lepton), Z
 176 boson p_T and ΔR between the two electrons (muons) for the 4.5 TeV signal mass sample. The
 177 efficiency is calculated with respect to the reco objects passing the offline object identification
 178 criteria as explained in Section 5.1 but without the isolation criteria. Each plot has two curves,
 179 where the black curve is simply the efficiency of events being triggered by the respective HLT
 180 path while the red curve is the efficiency of triggered events which fulfil the condition that the
 181 reco object in the event is also matched to a trigger object (by considering the closest trigger
 182 object in ΔR distance to the reco object).

The efficiency is defined as the ratio:

$$\epsilon_{HLT} = \frac{N_{HLT+ID}}{N_{ID}} \quad (1)$$

183 where, N_{HLT+ID} is the number of events with two electrons (muons) passing the identification
 184 criteria (see Sections 5.1 and 5.2) and also passing the trigger, and N_{ID} is simply the number
 185 of events with two electrons (muons) passing the identification criteria. The HLT efficiency
 186 varies between 90–98% for the double electron trigger and about 75–95 % for the double muon
 187 trigger, in both cases for the 4.5 TeV signal mass point. From the plots it is clear that there is
 188 a residual dependence on the lepton kinematics, even well above the turn-on point. The effect
 189 is more dramatic in the muon channel, and studies will continue to be performed after the de-
 190 livery of this Early Analysis document. One of the first possibilities under investigation is to
 191 take as trigger selection the “OR” of both a double muon and a single muon path. Notwith-
 192 standing the fact that such a choice would make it more difficult to calculate efficiencies and
 193 data/simulation scale factors, the prospects of a larger and more stable trigger efficiency out-
 194 weigh those difficulties. For the measurement of trigger efficiencies in data, we plan on using
 195 both prescaled triggers like Mu27_TkMu8 and also the “Reference Method” developed in the
 196 context of the Muon POG (but also applicable to electron triggers) [8].

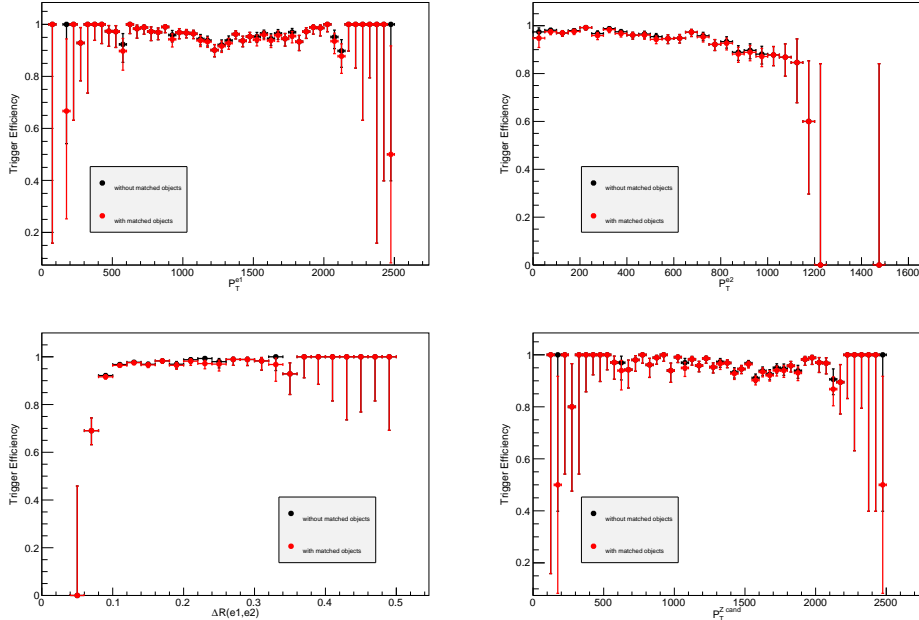


Figure 2: The top plots shows the double electron trigger efficiency as a function of the leading (left) and sub-leading electron p_T (right). The bottom plots show the efficiency as a function of ΔR between the two electrons (left) and the Z p_T (right), respectively.

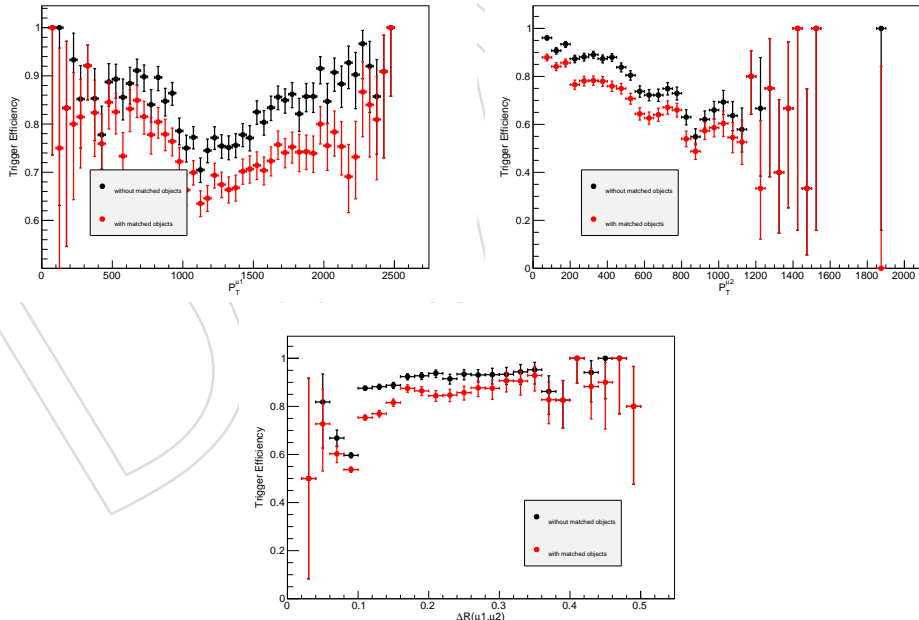


Figure 3: The top plots shows the double muon trigger efficiency as a function of the leading (left) and sub-leading muon p_T (right). The bottom plot shows the efficiency as a function of ΔR between the two muons.

4.2 Trigger criteria for VW analysis

Following the same strategy as for the corresponding 8 TeV analysis[9] the lowest threshold un-prescaled, non-isolated, single-lepton triggers have been considered:

- HLT_Mu45_eta2p1

for the SingleMu dataset, and

- HLT_Ele105_CaloIdVT_GsfTrkIdT

for the SingleElectron dataset.

These triggers are part of the final HLT trigger menu and they are not present in the Phys14 samples listed in Section 3. In order to study them, the Bulk Graviton signal has been privately simulated with CMSSW_7_4_0_pre8 for several mass points.

Figure 4 (5) shows the single muon (electron) trigger efficiency for the Bulk Graviton signal as a function of the muon (electron) p_T and η and as a function of the W p_T reconstructed from the E_T^{miss} and the muon (electron), for two signal mass points. The efficiency is calculated as the ratio:

$$\epsilon_{\text{HLT}} = \frac{N_{\text{HLT}+\text{ID}}^{\text{lep}}}{N_{\text{ID}}^{\text{lep}}} \quad (2)$$

where $N_{\text{HLT}+\text{ID}}^{\text{lep}}$ is the number of leptons passing the identification criteria (see Sections 5.1 and 5.2) and the trigger, and $N_{\text{ID}}^{\text{lep}}$ is the number of leptons passing the identification criteria. The signal efficiency is found to be about 97% (95%) in the plateau of the single electron trigger for the 1 (2) TeV signal mass point and about 94% (94.5%) in the plateau of the single muon trigger for the 1 (2) TeV signal mass point.

The lepton p_T threshold defined by the triggers also defines the minimum lepton p_T required in the analysis selections. Since the trigger threshold has been raised compared to Run 1, the same p_T requirement used in Ref. [9] can not be applied here; while, in principle, the p_T threshold for the muon channel can stay the same at 50 GeV, for the electron channel it should move to around 120 GeV and causing a signal inefficiency of about 14% (2%) for a signal with a mass of 0.8 (2) TeV. Hence, other options will be studied such as the use of isolated lepton triggers with lower p_T thresholds. However, for this version of the Early Analysis document we keep the same lepton p_T requirement used in the corresponding Run 1 analysis (see the summary of final selection in Section 6.7). For the measurement of the trigger efficiency in data, we plan on using prescaled lower threshold triggers with the exact same configuration as the signal triggers: HLT_Mu27 for the muon channel, HLT_Ele80 for the electron channel. We also consider using tag-and-probe techniques with the Z boson.

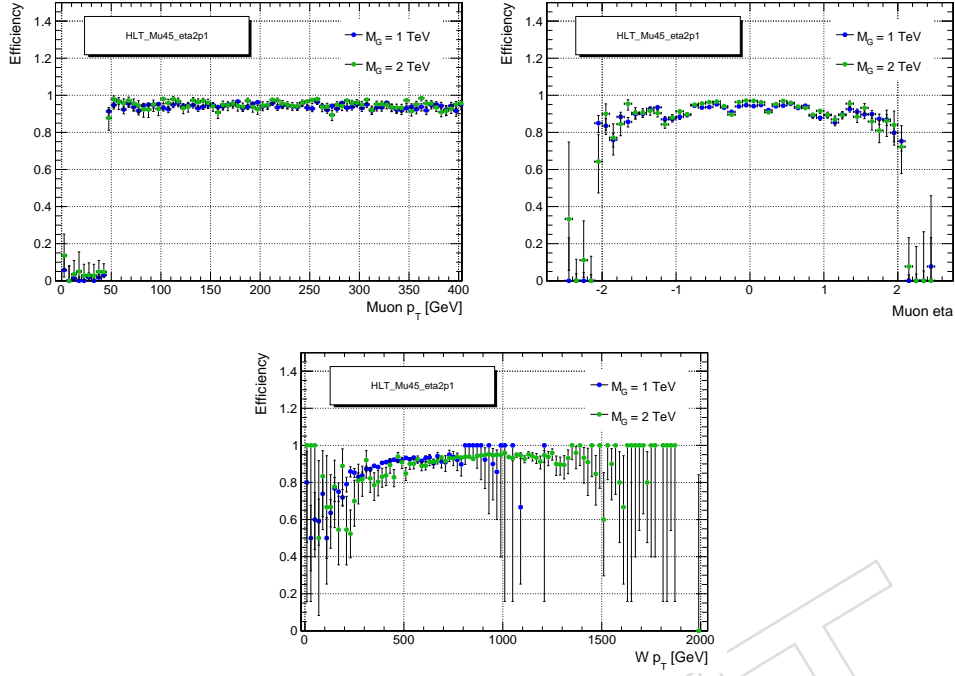


Figure 4: On the top, the single muon trigger efficiency as a function of the muon p_T (left) and η (right) is shown. On the bottom, the efficiency as a function of the $W p_T$ is shown for two signal mass points.

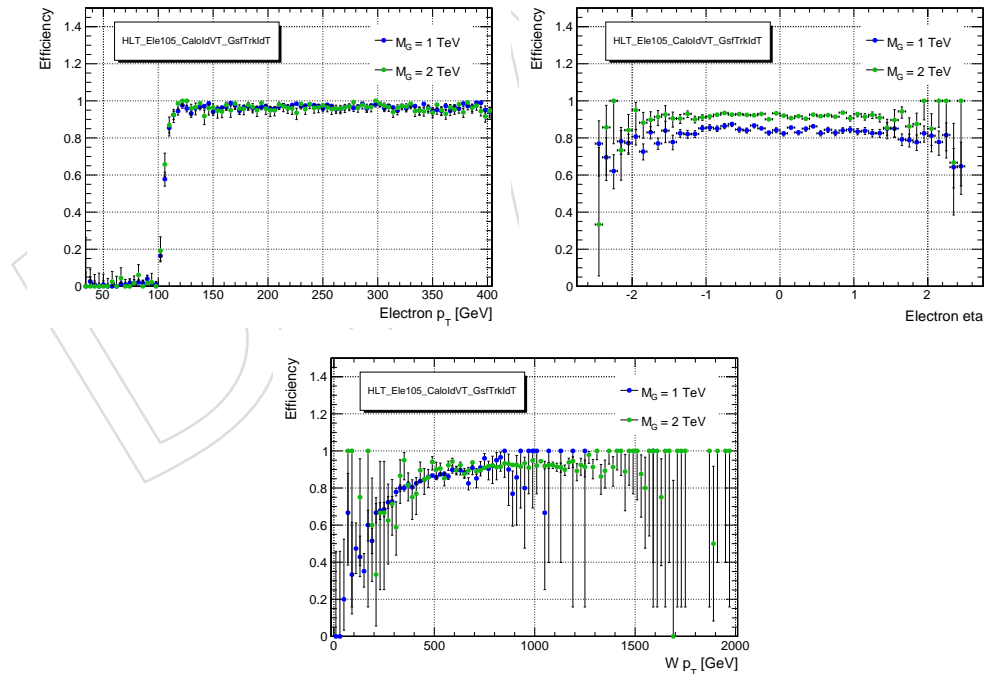


Figure 5: On the top, the single electron trigger efficiency as a function of the electron p_T (left) and η (right) is shown. On the bottom, the efficiency as a function of the $W p_T$ is shown for two signal mass points.

4.3 Trigger criteria for dijet analysis

The triggers used for the fully hadronic channel place requirements on the scalar sum of jet transverse energy, H_T , or on the jet groomed mass. The following inclusive triggers are studied

- HLT_PFHT650_WideJetMJJ900DEtaJJ1p5
- HLT_PFHT650_WideJetMJJ950DEtaJJ1p5
- HLT_PFHT900

as well as three grooming triggers cutting on the jet trimmed mass

- HLT_AK8PFJet360_TrimMass30_v1
- HLT_AK8DiPFJet280_200_TrimMass30_BTagCSV0p41_v1
- HLT_AK8PFHT700_TrimR0p1PT0p03Mass50_v1

This exercise has been performed using a QCD RelVal sample¹ with 50k events produced in CMSSW 7.4.X as the full list of triggers we are interested in is unavailable in higher statistics Phys14 samples.

Figure 6 shows the trigger turn-on curve for the three inclusive triggers as a function of dijet invariant mass for jets where

- (i) the two leading jets pass loose jet requirements as defined in Section 5.3. This is the “no tag category”.
- (ii) for jet pairs where one jet has a pruned mass in 60–100 GeV window, generically called a “W mass window”. This is the “single tag category”.
- (iii) for jet pairs where both jets have a pruned mass between in the W mass window. This is the “double tag category”.

The low statistics after applying mass cuts to both jets makes the trigger turn-on hard to define in category (III), but a sharp turn-on for all triggers is observed in the remaining categories, reaching the 100% efficiency plateau for dijet masses of around 1.0–1.1 TeV.

Trigger efficiencies as a function of pruned-jet (left) and softdrop-jet (right) mass for the grooming triggers are shown in Figure 7. Here the jet transverse momentum is required to be at least 500 GeV and no other mass cut is applied. The trigger with the earliest turn-on is the HLT_AK8PFJet360_TrimMass30_v1 trigger, requiring one jet to have a trimmed mass above 30 GeV at HLT level. This trigger reaches the 99% trigger efficiency threshold for groomed-jet masses around 45 GeV. Using the OR of the three triggers, a 99% efficiency is reached for jet pruned (softdrop) masses of 46 (45) GeV.

¹/RelValQCD_FlatPt_15_3000HS_13/CMSSW_7_4_0_pre9_ROOT6-MCRUN2_74_V7-v1/

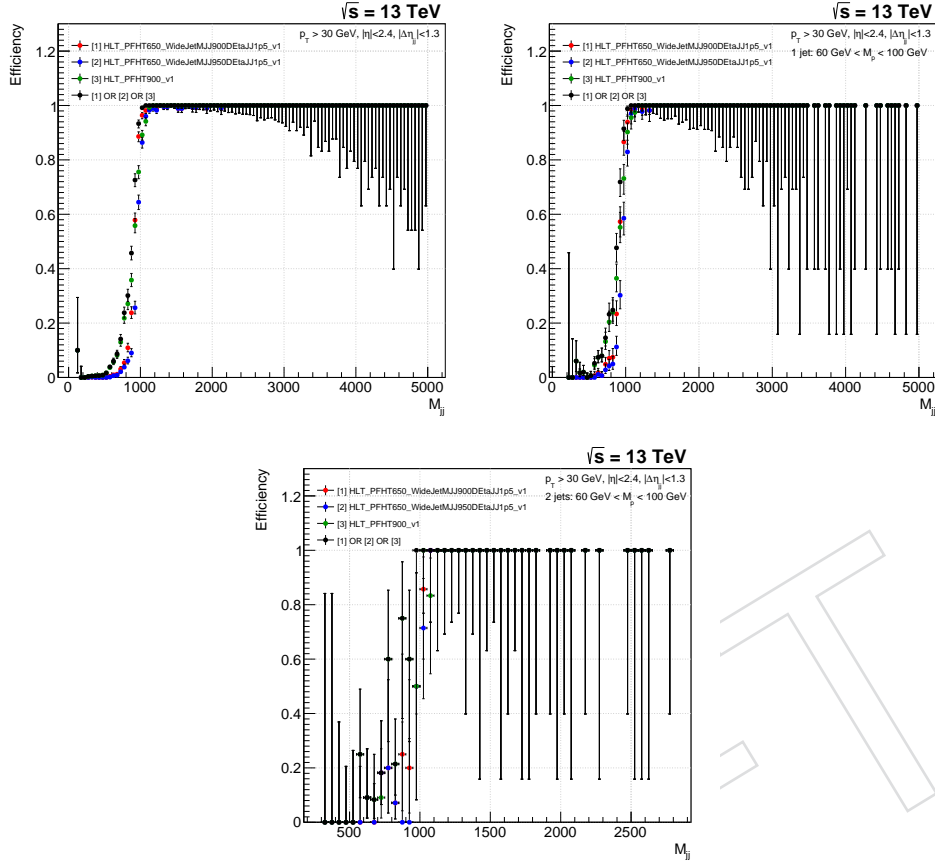


Figure 6: Efficiency for the inclusive triggers as a function of dijet invariant mass for all jets passing loose jet requirements (top left), for jet pairs where one jet has a pruned mass between 60 and 100 GeV (top right) and for jet pairs where both jets have a pruned mass between 60 and 100 GeV (bottom).

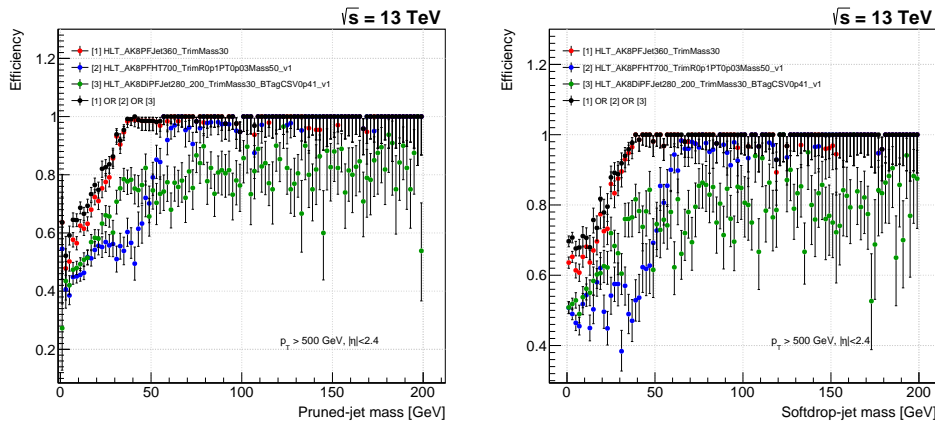


Figure 7: Efficiency for grooming triggers as a function of pruned-jet (left) and softdrop-jet mass (right) for jets with $p_T > 500 \text{ GeV}$.

Trigger efficiencies for the grooming triggers as a function of dijet invariant mass are shown in Figure 8. Again we are limited by statistics in the double tag (requiring two jets with pruned masses in W mass window) category, but the single tag category indicates a quicker turn-on for the HLT_AK8PFHT700_TrimR0p1PT0p03Mass50_v1 trigger. This trigger requires a particle-flow $H_T > 700 \text{ GeV}$ and the highest-mass jet to have a trimmed mass above 50 GeV. The HLT_AK8DIPFJet280_200_TrimMass30_BTagCSV0p41_v1 dijet trigger, requiring one b-tag at HLT level and one jet with a trimmed mass above 30 GeV, performs unexpectedly well with an efficiency of around 80%. This is surprising as this path should catch very few QCD events and its high efficiency is something that needs to be investigated further. Notice, however, that this b-tagging trigger is perfectly suitable for the V(qq)H(bb) dijet analysis [10].

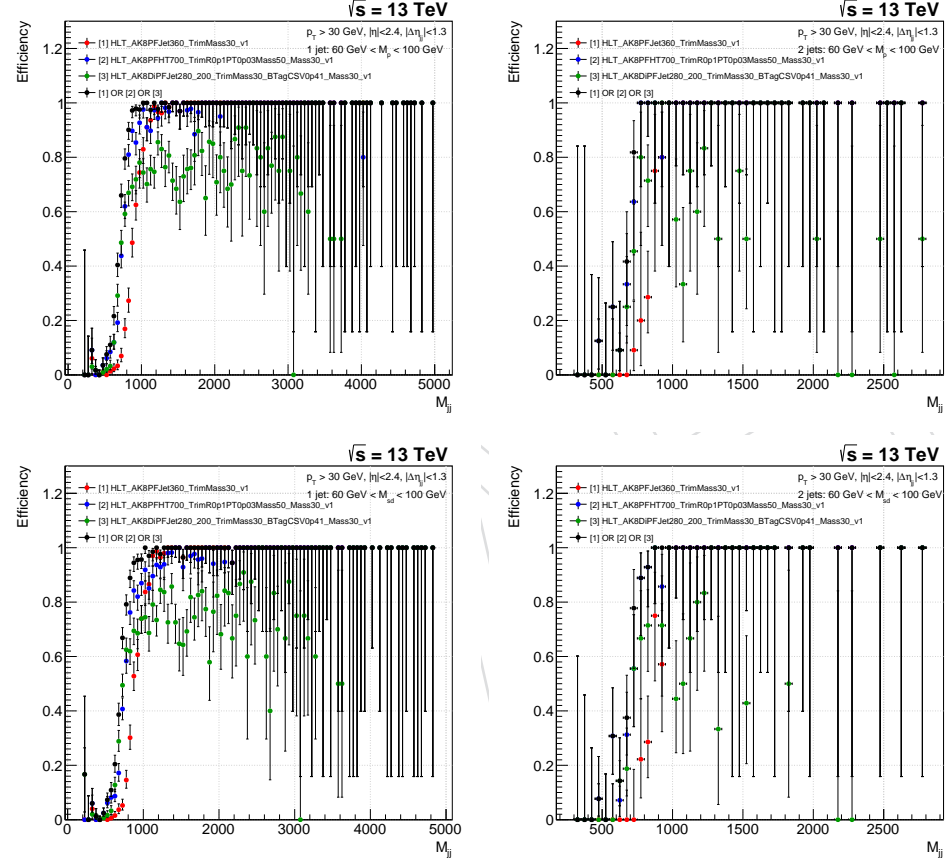


Figure 8: Efficiency for grooming triggers as a function of dijet invariant mass for jet pairs where one jet is required to have a pruned mass between 60 and 100 GeV (top left) and requiring both jets to have a pruned mass between 60 and 100 GeV (top right). The corresponding efficiencies when cutting on softdrop-jet masses are shown on the bottom, requiring one jet to have a softdrop mass between 60 and 100 GeV (bottom left) and requiring both jets to have a softdrop mass between 60 and 100 GeV (bottom right).

268

Figure 9 compares the trigger turn-on curves as a function of dijet invariant mass for jets passing one of the three inclusive triggers only and when including substructure triggers. The turn-on curves are shown for all jet pairs passing loose selections (top left), jet pairs where one jet has a pruned mass between 60 and 100 GeV (top right) and requiring both jets to have a pruned mass between 60 and 100 GeV (bottom). The 99% efficiency threshold is reached for lower dijet invariant masses when including substructure taggers in all cases.

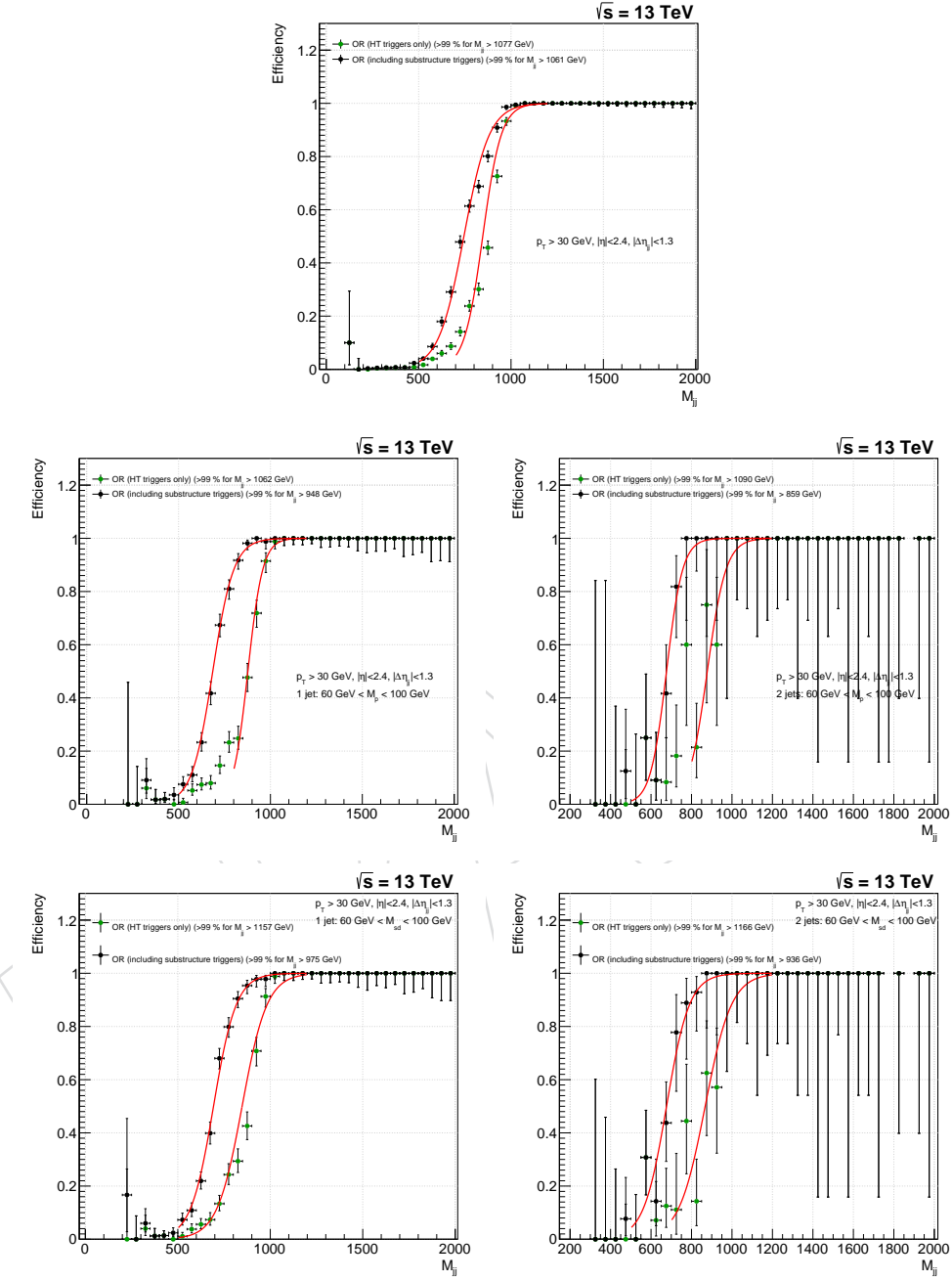


Figure 9: Trigger efficiency as a function of dijet invariant mass for all jet pairs passing loose selections (top), jet pairs where one jet has a pruned mass between 60 and 100 GeV (middle left) and requiring both jets to have a pruned mass between 60 and 100 GeV (middle right). The bottom plots show the trigger efficiencies when requiring one jet (bottom left) and both jets (bottom right) to have a softdrop mass between 60 and 100 GeV.

275 For comparison trigger turn-on curves using higher-statistics Phys14 samples are shown in Figure 10 for the two triggers available, HLT_PFHT900_v1 and HLT_AK8PFJet360_TrimMass30_v1.
 276 We see that the performance in 74X confirms expectations from the Phys14 exercise and that
 277 the analysis can start with a fully efficient trigger around dijet invariant masses of 1 TeV. In-
 278 cluding grooming triggers can lower the 99% trigger efficiency threshold by typically 50-100
 279 GeV once substructure is requested on the analysis level. The exact position of the trigger turn
 280 on would need to be estimated from data; our plan is to do so using lower threshold prescaled
 281 H_T triggers and a cross check with lepton triggers.

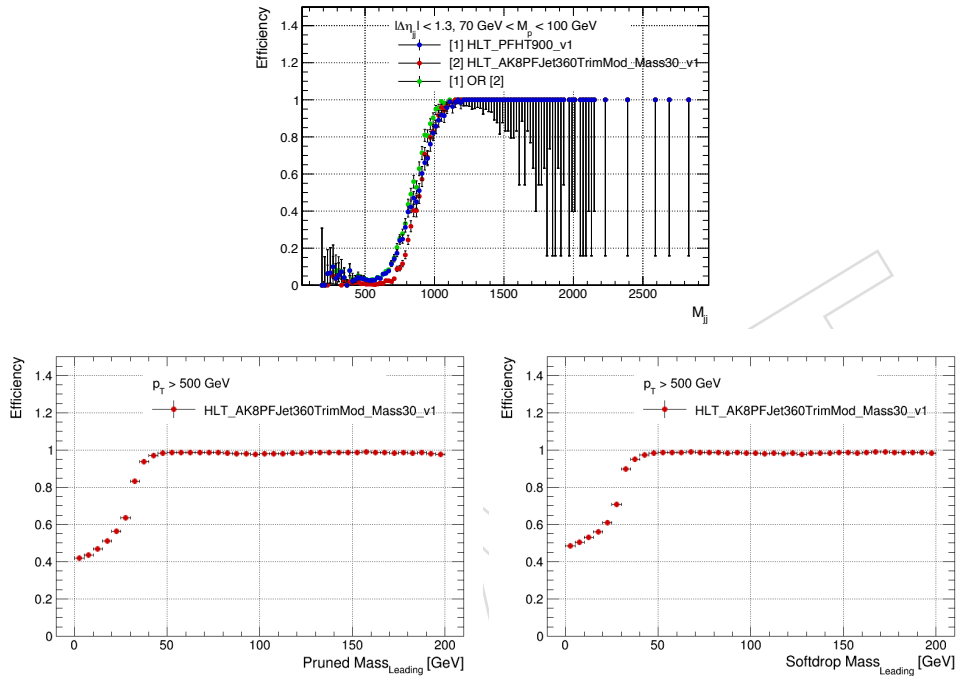


Figure 10: Trigger efficiencies using Phys14 simulated samples. Here as a function of dijet invariant mass (top) and as a function of pruned-jet (bottom left) and softdrop-jet (bottom right) mass.

283 5 Detector Objects and Boson Candidates

284 5.1 Electron Identification

285 The electron identification is based on the recommendation of the EGamma POG for high p_T
 286 electrons (version 5.1) as given at the HEEP ID Twiki [11]. Since the HEEP identification is
 287 developed in the context of the Z' search, which uses isolated electrons, the standard HEEP
 288 identification is adequate for the VW channel, and we plan to use their studies on efficiencies
 289 and scale factors for that channel. For the VZ channel, however, we consider a modified HEEP
 290 ID + particle flow isolation. The reason for that choice is that the isolation requirements defined
 291 in the HEEP ID are detector-based and not suited for boosted dielectron systems with a small
 292 ΔR between them - the footprint of one of the electrons tends to appear in the isolation cone
 293 of the other, leading to very low efficiencies. In the Run 1 analysis we solved that problem by
 294 applying special techniques to treat the isolation; it is expected that the same techniques would
 295 apply to the Run 2. While those techniques are not developed, we choose to apply the different
 296 isolation technique explained below. We will proceed to present this strategy to the EGamma
 297 POG as an official ID working point. A backup solution would be to use the standard EGamma
 298 POG ID solution (as opposed to the HEEP ID); that solution will not be further pursued in this
 299 Early Analysis document.

300 Firstly, electron candidates are required to have $p_T > 40 \text{ GeV}$ and $|\eta| < 2.5$. Further, the
 301 HEEP electron identification criteria used in the analysis consists of the following requirements
 302 (where B and E denote cuts for barrel and endcaps respectively):

- 303 • corrected transverse supercluster energy $E_T^{SC} > 35 \text{ GeV}$
- 304 • pseudo rapidity of the electron's supercluster $\eta^{SC} < 1.4442$ (B), $1.566\text{--}2.5$ (E)
- 305 • driven by calorimetric deposits (`isEcalDriven`)
- 306 • difference in η between the track position as measured in the inner layer, extrapolated
 307 to the interaction vertex and then extrapolated to the calorimeter and the η of
 308 the seed cluster of the supercluster < 0.004 (B), 0.006 (E)
- 309 • the difference in ϕ between the track position as measured in the inner layer, extrapolated
 310 to the interaction vertex and then extrapolated to the calorimeter and the ϕ of
 311 the supercluster < 0.06
- 312 • ratio of the hadronic energy of the CaloTowers in a cone of radius 0.15 centred on the
 313 electron's position in the calorimeter to the electromagnetic energy of the electron's
 314 supercluster $< 2/E + 0.05$ (B), $12.5/E + 0.05$ (E)
- 315 • the spread in eta in units of crystals of the electrons energy in 5x5 block centred on
 316 the seed crystal < 0.03 (only E)
- 317 • fraction of energy in 2x5 crystals around seed to the energy in 5x5 crystals around
 318 the seed > 0.94 , or fraction of energy in 1x5 crystals around seed to the energy in 5x5
 319 crystals around the seed > 0.84
- 320 • the number of inner tracker layer lost hits is smaller than 1
- 321 • have $|d_{xy}|$ smaller than 0.02cm (B), 0.05cm (E)

322 For completeness, the HEEP ID isolation criteria are as follows.

- 323 • EM + Had Depth 1 Isolation $< 2 + 0.03 \cdot E_T + 0.028 \cdot \rho$ (B)
- 324 • EM + Had Depth 1 Isolation $< 2.5 + 0.28 \cdot \rho$ for $E_T < 50 \text{ GeV}$ (E)
- 325 • EM + Had Depth 1 Isolation $< 2.5 + 0.03 \cdot E_T - 50 + 0.28 \cdot \rho$ for $E_T > 50 \text{ GeV}$ (E)

- 326 • Tracker Isolation (sum of tracks p_T) < 5 GeV (B and E).

The alternative isolation is similar to the cut used in the medium working point of the cut-based electron ID as described in the EGamma Twiki [12]. It is a particle flow based isolation with delta Beta pileup corrections calculated in a cone size of 0.3. The isolation variable I_{rel} is calculated as:

$$I_{rel} = \frac{\sum_{CH} p_T + \max(0.0, \sum_{NH} E_T + \sum_{\gamma} E_T - 0.5 \times \sum_{PU} p_T)}{p_T} < 0.1 \quad (3)$$

327 where $\sum_{CH} p_T$ is the sum of the transverse momenta of the charged hadrons, $\sum_{NH} E_T$ is the sum
 328 of transverse energies of the neutral hadrons, $\sum_{\gamma} E_T$ is the sum of the transverse energy of par-
 329 ticle flow photons and $\sum_{PU} p_T$ is the sum of transverse momenta of the charged particles in the
 330 cone of interest but with particles not originating from the primary vertex (for pileup correc-
 331 tions). Notice that with this definition of the isolation the other electron of the system does not
 332 enter the calculation. Figure 11 shows the distribution of transverse energy of a generator level
 333 electron (left) and the electron ID efficiency as a function of the electron transverse energy at
 334 the generator level for one of the signal mass points for the RS Graviton signal. The efficiency
 335 is found to be between 70–80% for electrons with the modified HEEP identification criteria.

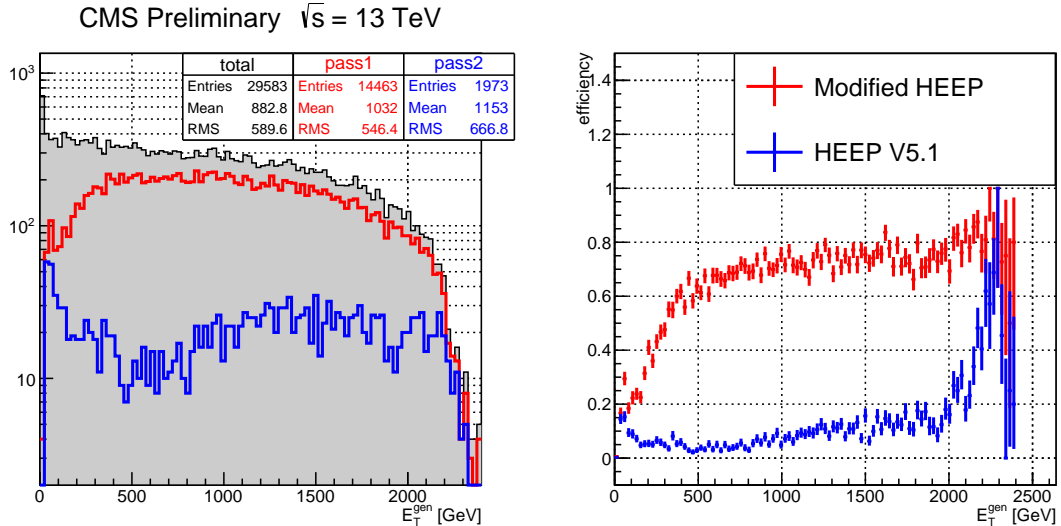


Figure 11: Distribution of transverse energy of the electron (left) and the electron ID efficiency as a function of the transverse energy (right) for the modified HEEP ID.

336 5.2 Muon Reconstruction and Identification

337 For the analysis that requires a leptonic-Z candidate, the muon reconstruction efficiency should
 338 be as high as possible in order to maximize the reconstruction efficiency of the Z boson. As
 339 discussed in Ref. [13], the Run 1 global muon reconstruction suffers from the “greedy muon”
 340 problem when another muon is close-by, i.e. the reconstruction efficiency of global muon drops
 341 as $\Delta R_{\mu\mu}$ decreases. The efficiency-drop is a consequence of the seeding algorithm, which takes
 342 by mistake in the seed some segments from the other muon. At the end of the exhaustive
 343 muon trajectory builder, a cleaning is applied based on the number of segments and the χ^2 of
 344 the muon trajectory. After the cleaning, only one muon trajectory is selected among the group
 345 of trajectories that share segments. The efficiency could be recovered partially by removing
 346 the cleaning inside the exhaustive trajectory builder. In addition, one could also reduce the

347 matching window when matching the track segments in the muon chamber to those in the
 348 tracker, which decreases the probability of including segments from nearby muons.

349 The Run 2 muon standard reconstruction has removed the cleaning in the exhaustive trajectory
 350 builder. The matching window is kept at $\Delta\phi = 0.25$ and $\Delta\eta = 0.2$. We first use the Run 2
 351 default settings and study reconstruction efficiencies for the following three scenarios: (i) two
 352 global muons, (ii) at least one global muon (the other could be a global or a tracker muon), (iii)
 353 two tracker muons. Then, we vary the $\Delta\phi$ window from $\Delta\phi = 0.05$ to $\Delta\phi = 0.25$, with steps
 354 of 0.05, and compare the muon reconstruction efficiencies. Note, the three scenarios are not
 355 exclusive from each other, i.e. scenarios (i) and (ii) are the subsets of scenario (iii) while scenario
 356 (i) is the subset of scenario (ii). We use the 4.5 TeV RS Graviton sample with GEN-SIM-RAW
 357 content. sample (see Section 3) to perform this study. The variation of $\Delta\phi$ window requires a
 358 re-reconstruction of the sample and the configuration file could be found in Ref. [14].

359 In order to compute the reconstruction efficiency, we first look for a pair of status-1 muons at
 360 the generator level in each event. The mother of status-1 muons must be either a Z-boson or a
 361 status-2 muon. Both muons must have $p_T > 20 \text{ GeV}$ and $|\eta| < 2.4$.

362 Then, we check how often each generator-muon pair is matched in ΔR to a pair of arbitrated
 363 reconstruction-level muons satisfying the following requirements:

- 364 • $p_T > 10 \text{ GeV}$ and $|\eta| < 2.4$
- 365 • The inner tracks of these two reconstructed muons must be different
- 366 • The muons have to pass the Arbitrated Tracker Muon requirement:
`muon::isGoodMuon (*mu, muon::TrackerMuonArbitrated) == true`

368 The matching ΔR must be less than 0.1.

369 Figures 12–14 show the reconstruction efficiencies of two global muons, global + tracker muons,
 370 and two tracker muons, with the Run 2 default settings, as a function of ΔR , $|\Delta\eta|$, and $|\Delta\phi|$
 371 between the two generator-level muons, respectively. One could find that the efficiency of re-
 372 constructing two global muons is not unity even for large ΔR since the large value of ΔR could
 373 be a combination of small $\Delta\phi$ and large $\Delta\eta$ or vice versa. Figures 15 show the reconstruction
 374 efficiencies of the two global muons with various $\Delta\phi$ match windows. Although the global-
 375 global efficiency has improved significantly with respect to Run 1, it is still not large enough to
 376 allow an efficient reconstruction of leptonic Z bosons. Therefore, we have decided to select at
 377 least one global muon (instead of two global muons) when reconstructing the leptonic Z boson.

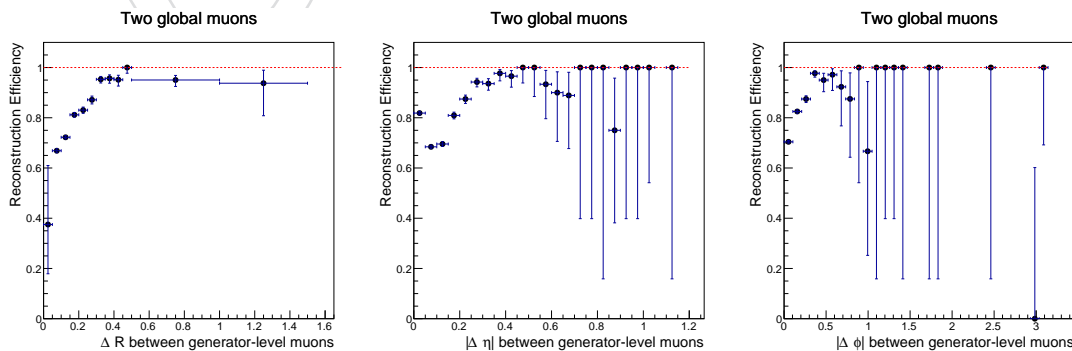


Figure 12: Reconstruction efficiency of two global muons as a function of ΔR (left), $|\Delta\eta|$ (middle), and $|\Delta\phi|$ (right) between the two generator-level muons. The muon-tracker segment matching window $\Delta\phi$ is set to 0.25.

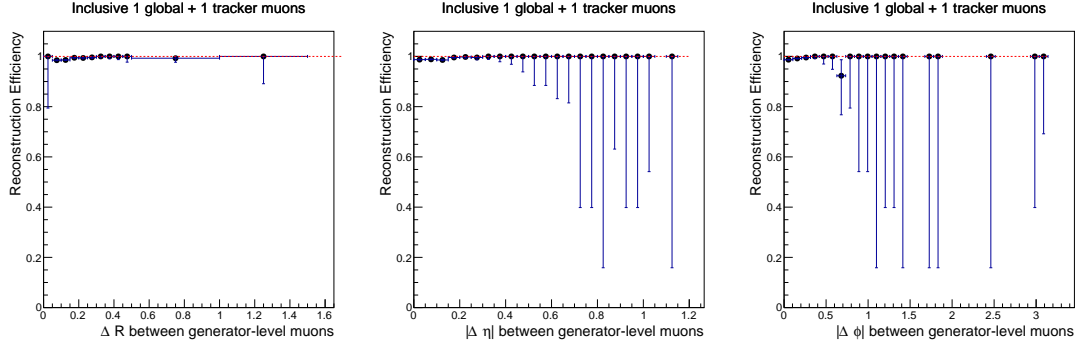


Figure 13: Reconstruction efficiency of global + tracker muons as a function of ΔR (left), $|\Delta\eta|$ (middle), and $|\Delta\phi|$ (right) between the two generator-level muons. The muon-tracker segment matching window $\Delta\phi$ is set to 0.25.

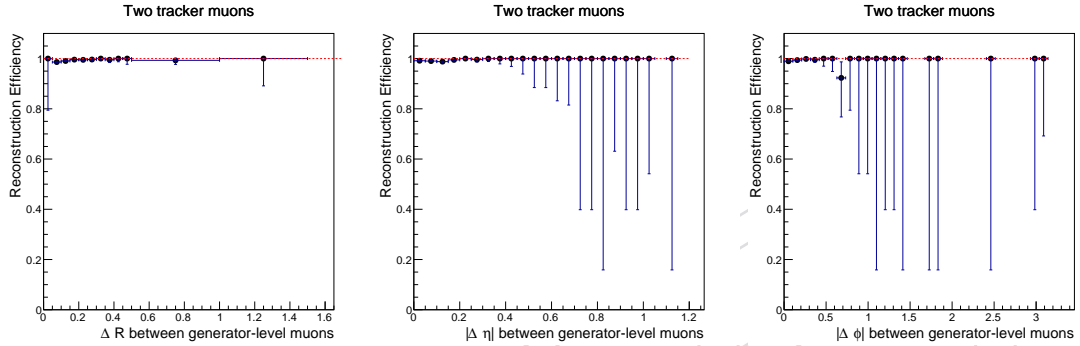


Figure 14: Reconstruction efficiency of two tracker muons as a function of ΔR (left), $|\Delta\eta|$ (middle), and $|\Delta\phi|$ (right) between the two generator-level muons. The muon-tracker segment matching window $\Delta\phi$ is set to 0.25.

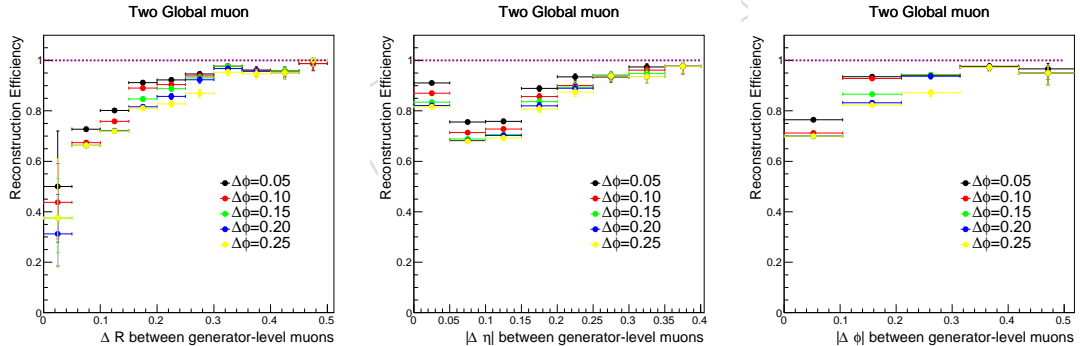


Figure 15: Reconstruction efficiency of two global muons as a function of ΔR (left), $|\Delta\eta|$ (middle), and $|\Delta\phi|$ (right) between the two generator-level muons. The muon-tracker segment matching window is varied from $\Delta\phi = 0.05$ to $\Delta\phi = 0.25$.

378 For muon identification and their momentum assignment we follow the recommendation of
 379 the Muon POG Twiki [15]. The new versions (after CMSSW_5_3_6_patch1) of the HighPT muon
 380 ID and the TuneP momentum assignment are used, leading to the requirements:

- 381 • muon identified as global muon;
- 382 • at least one muon chamber hit included in the global-muon track fit;
- 383 • muon segments in at least two muon stations;
- 384 • tracker track transverse impact parameter $d_{xy} < 2\text{mm}$ w.r.t. the primary vertex;
- 385 • analogously, longitudinal impact parameter $d_z < 5\text{mm}$;
- 386 • number of pixel hits larger than zero;
- 387 • number of tracker layers with hits > 5 .
- 388 • the track used to obtain the muon momentum needs to pass $dp_T/p_T < 0.3$.

389 Notice that some of these muon identification criteria cannot be applied to tracker muons,
 390 which will be needed by the VZ channel. We are on the course of developing modified criteria,
 391 which will be presented to the Muon POG.

On top of the identification cuts, muon candidates are requested to pass a relative isolation cut

$$I_{rel} = \frac{\sum p_T^{\text{tracks}}}{p_T^{\mu\text{on}}} < 0.1 \quad (4)$$

392 where $\sum p_T^{\text{tracks}}$ is the scalar sum of tracks' p_T in a cone of $\Delta R < 0.3$ around the muon direction,
 393 and $p_T^{\mu\text{on}}$ is the transverse momentum of the muon itself. For the VZ channel, this isolation
 394 criteria should be modified to take out the track matched to the other muon.

“Tight” muon candidates have to pass the HighPT muon ID and isolation described above and need to have $p_T > 50\text{ GeV}$ and $|\eta| < 2.1$ (to be in the plateau of the trigger efficiency). “Loose” muon candidates (used for the lepton veto selection) are required to pass the same ID and isolation with less stringent kinematic cuts of $p_T > 20\text{ GeV}$ and $|\eta| < 2.4$. Figure 16 shows the HighPT muon ID efficiency for the Bulk Graviton signal as a function of the muon p_T and η for different signal mass points. The efficiency is calculated as the ratio:

$$\varepsilon_{ID} = \frac{\text{number of matched HighPT muons}}{\text{number of matched reconstructed muons}} \quad (5)$$

and it is found to be around 95% for muons with p_T above 60 GeV.

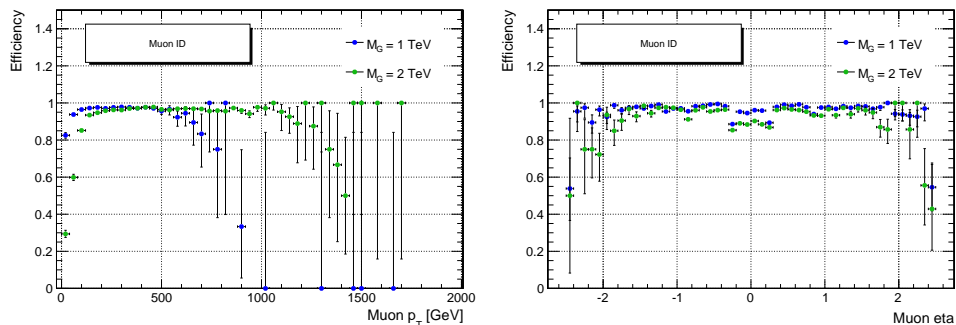


Figure 16: Muon ID efficiency as a function of the muon p_T (left) and η (right) for two signal mass points, $M_{RS} = 1\text{ TeV}$ (green points) and 2 TeV (blue points).

396 5.3 Jet Identification and Substructure

397 Events in the CMS detector are reconstructed using the the particle-flow algorithm [16] which
398 combines information from all sub-detectors in order to reconstruct stable particles (muons,
399 electrons, photons, neutral and charged hadrons). Charged hadrons not associated to the pri-
400 mary vertex are discarded in the jet reclustering in order to remove contributions from pileup
401 (*charged hadron subtraction*) [17]. The remaining particles are further used as input to jet cluster-
402 ing algorithms to reconstruct particle-flow jets. The jets used in the fully hadronic and semi-
403 leptonic analyses are first clustered with the anti- k_T jet clustering algorithm [18] with a clus-
404 tering parameter of $R = \sqrt{(\Delta\eta)^2 + (\Delta\phi)^2} = 0.8$ using the FASTJET package [19]. All jets are
405 further required to pass loose jet identification requirements provided by the JetMET POG [20].
406 These are as follows:

- 407** • Number of Constituents > 1 , for all jet η
- 408** • Neutral Hadron (Photon) Energy Fraction $< 0.99 (< 0.99)$, for all jet η
- 409** • Muon (electron) energy fraction $< 0.8 (< 0.9)$
- 410** • Charged Hadron Multiplicity > 0 , for jet $|\eta| < 2.4$
- 411** • Charged Hadron (EM) Energy Fraction $> 0 (< 0.99)$, for jet $|\eta| < 2.4$

412 Subsequent to this procedure, the constituents of these jets are reclustered with the Cambridge-
413 Achen algorithm [21, 22], requiring 2 exclusive subjets. Two different jet grooming algorithms
414 are investigated in this Early Analysis document. The first is the “jet pruning” algorithm [23,
415 24], which attempts to remove soft and wide-angle contributions to jets after reclustering. This
416 algorithm was used extensively during Run 1 of the LHC at CMS. However, after extensive
417 theoretical work to understand and calculate the jet mass from first principles in QCD (see,
418 for instance, Ref. [25] and [26]), a new algorithm was developed to accomplish jet grooming
419 in a theoretically safer way, the “soft drop” algorithm [27]. This removes soft and wide-angle
420 components of the jets in a more theoretically controlled way.

In addition to these jet grooming algorithms, the “n-subjettiness” of jets [28] is also extensively used to identify boosted vector bosons that decay hadronically. This method uses the distribution of jet constituents relative to the jet axis in order to quantify how well the jet can be divided into N subjets. The computation is done by reclustering the jet using the k_T -algorithm until N protojets are left. The direction of the remaining jets are then used to compute the “N-subjettiness” as

$$\tau_N = \frac{1}{d_0} \sum_k p_{T,k} \times \min(\Delta R_{1,k}, \Delta R_{2,k}, \dots, \Delta R_{N,k}) \quad (6)$$

with the normalization factor d_0 :

$$d_0 = \sum_k p_{T,k} \times R_0 \quad (7)$$

421 and R_0 is the clustering parameter of the original jet, $p_{T,k}$ is the p_T of the k -th jet constituent and
422 $\Delta R_{n,k}$ is its distance to the n -th subjet. In particular, the ratio of the “2-subjettiness” to the “1-
423 subjettiness” ($\tau_2 / \tau_1 = \tau_{21}$) has excellent capability at separating jets originating from boosted
424 vector bosons from jets originating from quarks and gluons.

425 Jets are corrected for nonlinearities in p_T and rapidity using standard jet energy corrections at
426 CMS as described in Ref. [29] for $R=0.8$ anti- k_T jets. Additionally, the contribution from ad-
427 ditional proton-proton interactions within the same bunch crossing (pileup) is corrected using
428 the approach outlined in Ref. [30]. The median p_T per unit area (ρ) is computed using a fixed

grid approach, and the jet area (A) is calculated with a "ghosting" procedure. The product of $\rho \times A$ is subtracted from the jet four-vector. This estimated pileup contribution is then modulated versus rapidity by an offset correction derived from minimum bias data. While for the early analysis we stick to the methods described above, there are new techniques available to better correct the softdrop jet mass and N-subjettiness distributions for pileup effect, such as jet-mass-aware-area-subtraction, constituent subtraction, softkill, PUPPI, that can potentially improve the resolution of these variables.

For the purposes of this Early Analysis document, we are still using the jet pruning algorithm to define the hadronic V boson tagger. However, the plan for all the analyses with jet substructure is to move to the soft drop algorithm, due to its superior theoretical qualities. Of course, all final optimisations for the jet substructure techniques will have to be redone with the same version of the reconstruction that is going to be used for data taking, and studies for hadronic V scale factors will have to be done when the data arrives.

5.4 B-tagging

The B-tagging algorithms for Run 2 have undergone substantial development and have been improved with respect to their Run 1 analogues. Previously used Combined Secondary Vertex (CSV) discriminant is replaced by the new CSVv2+IVF. The main difference between them is switching from likelihood ratio (CSV) to neural network based (CSVv2) discriminator with use of additional variables to improve track quality and selection, and using Inclusive Vertex Finder (IVF) as input. The preliminary working points (WP) defined by the BTV POG correspond to thresholds of 0.423 (loose), 0.814 (medium) and 0.941 (tight) as is described at the BTV Twiki [31]. The mistag efficiencies are 10%, 1% and 0.1%, respectively.

In the signal selection events are vetoed in presence of AK4 jets tagged as b quarks to reduce the contribution from $t\bar{t}$ and single- top background processes. The relative contribution from these processes is increased at 13 TeV, and the importance of these backgrounds is higher for the VW channel than for the VZ or hadronic channels. Given that the b-tag algorithms are also modified, we have reevaluated the choice of the working point for the Run 2 version of the analyses. As figure of merit we use the Punzi significance:

$$P = \frac{\epsilon_S}{1 + \sqrt{B}} \quad (8)$$

where ϵ_S is the selection efficiency for RS gravitons and B is the number of background events passing the selection. The medium WP is found to be the optimal choice for the analysis. The veto preserves about 90% of the signal events. The details about the veto performance are given in Table 4, which uses the Phys14 simulation samples.

Table 4: Summary of the b-jet veto performance as a function of the choice of the WP. CSVv2+IVF discriminant is used. The figure of merit is the Punzi significance. Results are segregated by RS graviton mass and lepton type. The medium WP is found to be universally the best match for these analyses.

Working Point	Muon Channel		Electron Channel	
	$M_{RS} = 1 \text{ TeV}$	$M_{RS} = 2 \text{ TeV}$	$M_{RS} = 1 \text{ TeV}$	$M_{RS} = 2 \text{ TeV}$
loose	7.39	0.73	5.93	0.63
medium	7.47	0.78	6.13	0.68
tight	7.12	0.77	5.83	0.69

455 **5.5 Leptonic Z Candidate Reconstruction**

456 Leptonic Z boson candidates are reconstructed from a pair of same-flavour and opposite-charge
 457 leptons $\ell^+\ell^-$, where $\ell = e, \mu$. Candidates formed by electrons $Z(e^+e^-)$ and by muons $Z(\mu^+\mu^-)$
 458 are merged into one single collection. The selected candidates satisfy requirements on the
 459 invariant mass $m_{\ell\ell}$ and transverse momentum $p_T^{\ell\ell}$, as described in Section 6.2.

460 As explained above, the two leptons originated from the decays of high- p_T Z bosons are ex-
 461 pected to be closer to each other (small ΔR). In this boosted regime, one lepton may spoil
 462 the isolation of the other due to the coarse detector resolution in the muon chambers and the
 463 calorimeters. For smaller values of $\Delta R(\ell^+\ell^-)$ a drop in efficiency may occur, unless we take
 464 explicit measures to avoid that during the lepton identification, as explained in Sections 5.1 and
 465 5.2.

466 **5.6 Leptonic W Candidate Reconstruction**

The $W \rightarrow \ell\nu$ candidate in the event is formed from the charged lepton passing the selection requirements (electron or muon) and the E_T^{miss} (representing the transverse component of the neutrino momentum) reconstructed in the event. In order to reconstruct the m_{WW} mass, an estimate of the longitudinal component of the neutrino momentum, $p_{z\nu}$, is needed. This can be evaluated imposing a constraint on the lepton-neutrino system invariant mass, that must be equal to $m_W = 80.4$ GeV. Starting from this, the p_z of the neutrino can be calculated by solving the following second-order equation:

$$m_\ell^2 + m_\nu^2 + 2 \cdot (E_\ell E_\nu - px_\ell px_\nu - py_\ell py_\nu - pz_\ell pz_\nu) = m_W^2 = (80.4 \text{ GeV})^2 \quad (9)$$

The solutions are:

$$pz_\nu^\pm = \frac{-B \pm \sqrt{\Delta}}{2A} \quad (10)$$

where:

$$\begin{aligned} a &= m_W^2 - m_\ell^2 + 2px_\ell px_\nu + 2py_\ell py_\nu \\ A &= 4(E_\ell E_\nu - pz_\ell pz_\nu) \\ B &= -4apz_\nu \\ C &= 4E_\ell E_\nu(px_\nu^2 + py_\nu^2) - a^2 \\ \Delta &= B^2 - 4AC \end{aligned} \quad (11)$$

467 If $\Delta > 0$ there are two real solutions and $p_{z\nu}$ is set equal to the one with the smaller absolute
 468 value. If $\Delta < 0$ there are two complex solutions and $p_{z\nu}$ is set equal to the real part of the two
 469 solutions ($p_{z\nu} = -B/2A$).

470 A study is underway on more sophisticated methods to estimate the neutrino longitudinal
 471 momentum. One of those methods, currently being studied in our group, is documented in
 472 Ref. [32], and its implementation can be found online [33]. Essentially it treats differently the
 473 case in which you have an imaginary solution. The resolution of the m_{WW} mass slightly im-
 474 proves and the resulting W mass has more physical meaning.

475 **5.7 Hadronic V Candidate Reconstruction**

476 For heavy resonances decaying into vector bosons, the bosons emerging from such a decay
 477 would usually be highly energetic and their hadronic decay products would be merged into
 478 one single jet [34]. The identification of such a boson takes advantage of the substructure topol-
 479 ogy introduced by the merged quark pair in order to differentiate them from quark- and gluon-
 480 induced jets [35], a method called "W/Z-tagging". One high- p_T jet is required to have a

481 pruned or softdrop jet mass in a window around the W/Z mass, separating it from the QCD
 482 multijet background which peaks at lower masses. To discriminate between two-pronged jets
 483 from a vector boson decay and jets stemming from the multijet background, the n-subjetness
 484 ratio $\tau_{21} = \tau_2 / \tau_1$ is used, with τ_N as defined in Section 5.3. The pruned mass and τ_{21} distributions
 for signal and background are shown in Figure 17.

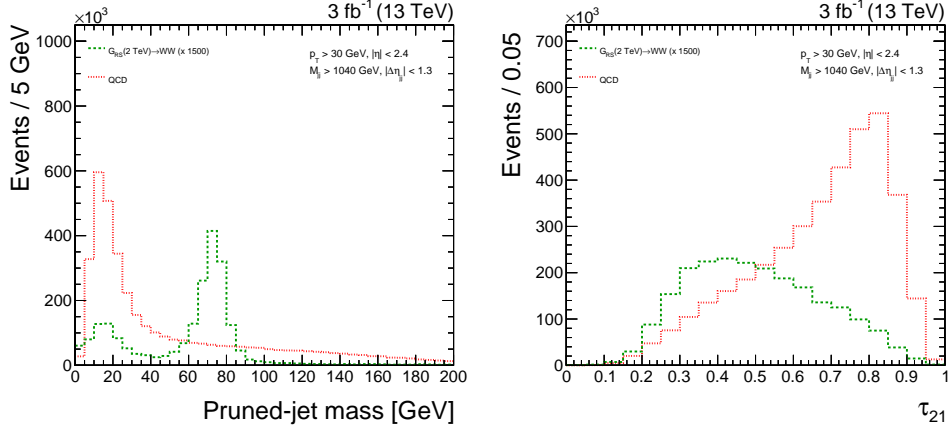


Figure 17: Pruned-jet mass (left) and τ_{21} distribution for signal and background. Here a signal cross section of 1 pb is assumed and the signal is scaled by a factor of 1500.

485
 486 To understand the performance of groomed and substructure variables on merged V bosons,
 487 a control sample of pure hadronic W's can be isolated in data, looking at the high p_T $t\bar{t}$ sam-
 488 ple. Background scale factors and mass scale/resolution uncertainties are estimated from data
 489 following the same procedure as for the Run 1 analysis in Ref. [9].

490 Control plots in ttbar control sample

491 To select this control sample, we use the kinematic selections that will be described described
 492 in Section 6.7, but changing the requirement on the number of b-tagged AK4 jets: looking at the
 493 AK4 reconstructed jets, outside of the AK8 jet cone, it is required at least one CSV "medium"
 494 AK4 jet. To have a greater data sample, we choose the AK8 jet in the opposite hemisphere of
 495 the lepton, with the highest mass and $p_T > 200$ GeV. This is different from the standard signal
 496 selection, which uses the highest p_T AK8 jet in the event, with a minimum p_T threshold at 200
 497 GeV.

498 Making these requirements, we have a nearly pure sample of $t\bar{t}$ events, with a small contam-
 499 ination from single top, W+jets and VV events. The jet mass, jet p_T , $m_{\ell v j}$, and τ_{21} variables
 500 are shown in Figure 18 for the muon channel and Figure 19 for the electron one. These plots
 501 include statistical uncertainties from the simulation.

502 Background scale factors and mass scale/resolution uncertainties

503 The $t\bar{t}$ control sample is used to extract data/simulation scale factors for non-dominant back-
 504 ground contributions: $t\bar{t}$, single top, WW/WZ, as well as for the signal. For the $t\bar{t}$ and single top
 505 contributions, we compute a scale factor based on the difference between data and simulation
 506 expectation in the signal region of the control sample. On the contrary, for the WW/WZ and
 507 signal contributions, we are only concerned with the efficiency for pure W-jet signal, so it is
 508 necessary to subtract background contributions to get the correct signal efficiency scale factor.
 509 For the $t\bar{t}$ and single top contributions, we apply all the cuts used to define the $t\bar{t}$ control region,
 510 defined previously in this section. Then, looking only inside the jet mass signal region (m_j in

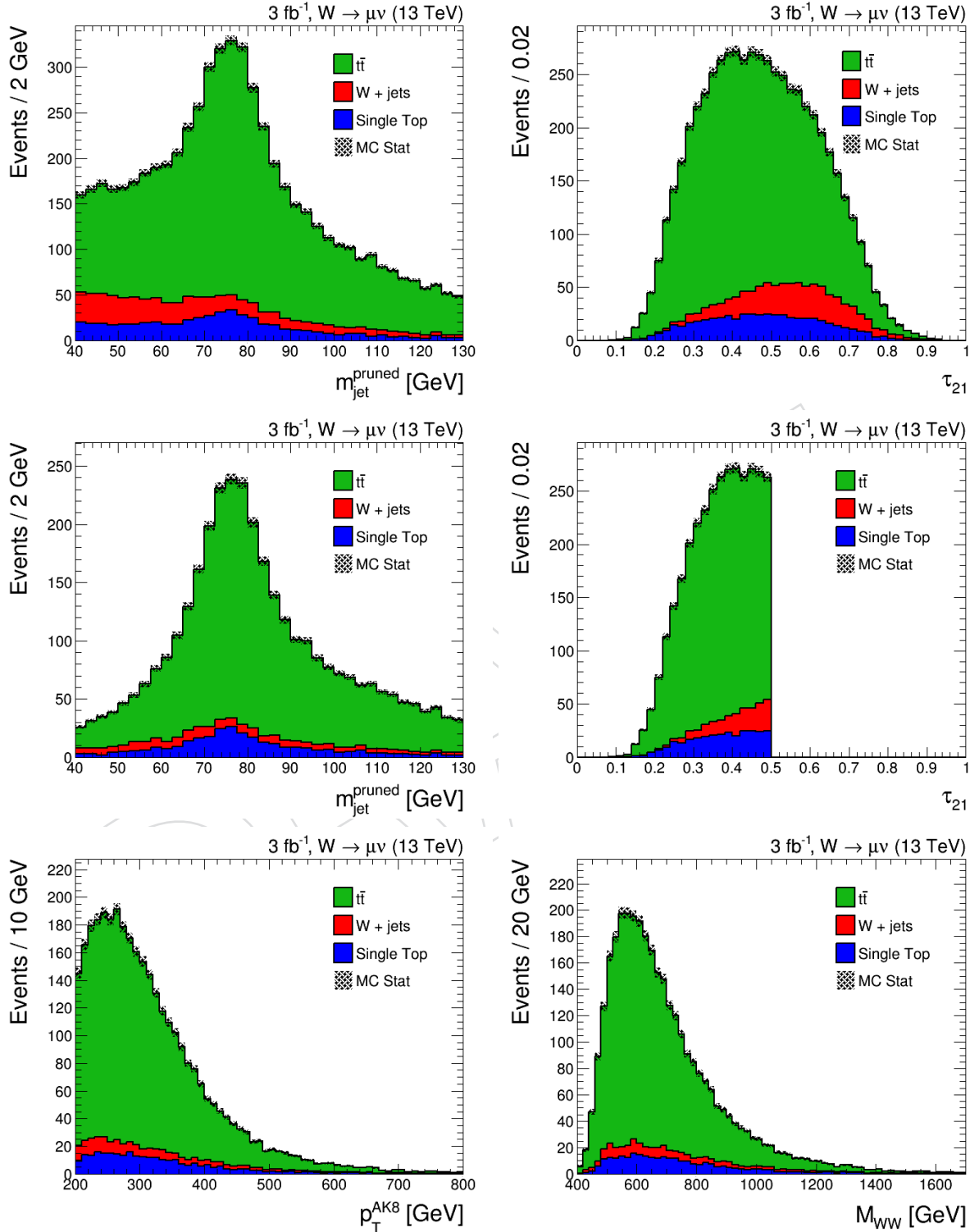


Figure 18: Distributions in the $t\bar{t}$ control sample for muon+jet final state. The top two plots are before making any cut on τ_{21} , while the remaining ones are after $\tau_{21} < 0.5$.

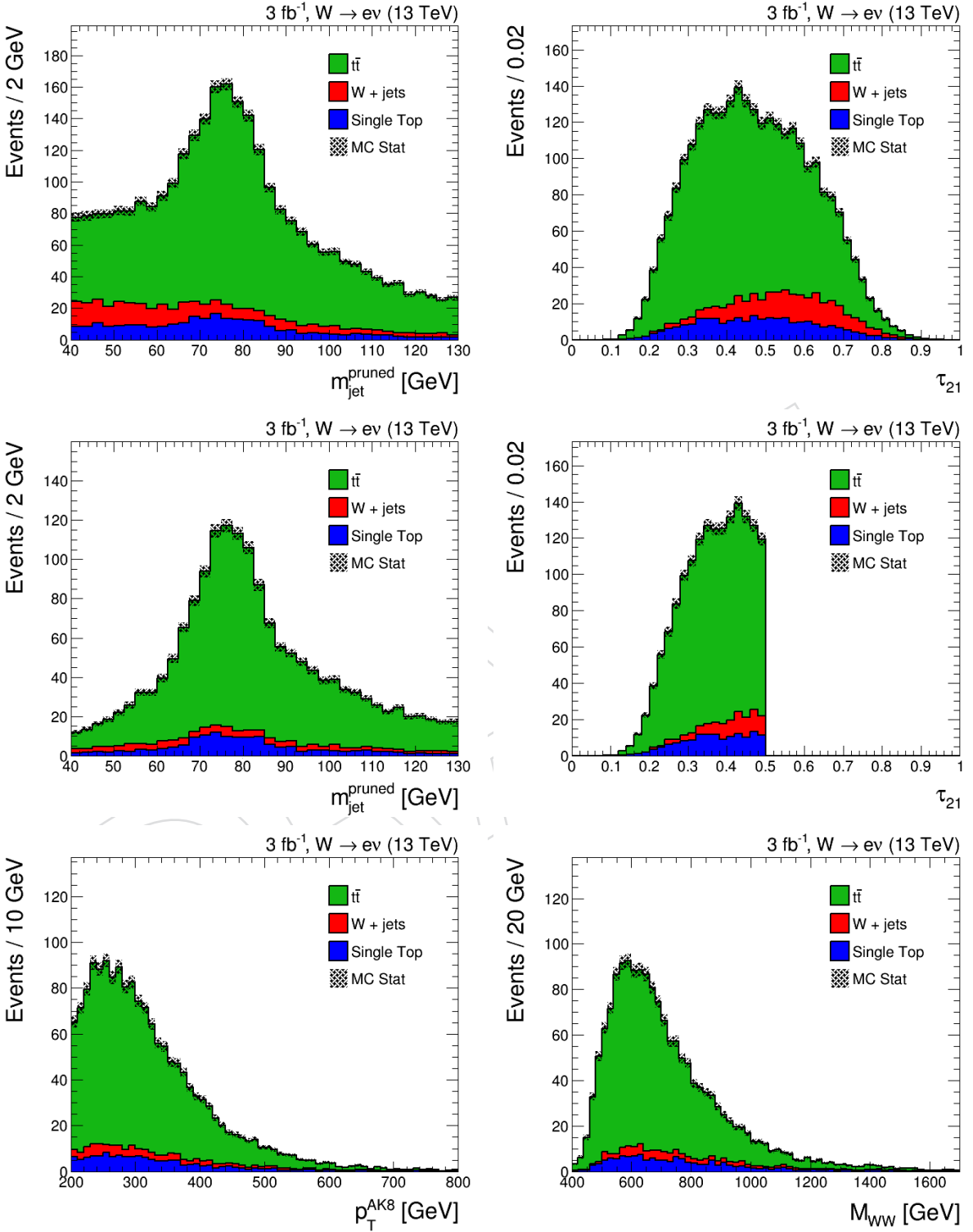


Figure 19: Distributions in the $t\bar{t}$ control sample for electron+jet final state. The top two plots are before making any cut on τ_{21} , while the remaining ones are after $\tau_{21} < 0.5$.

the 60–100 GeV range) and applying the N-subjettiness τ_{21} selection, we account for the difference after the τ_{21} cut, to get the data/simulation scale factor for both the Low Purity ($\tau_{21} \in [0.5, 0.75]$) and High Purity category ($\tau_{21} < 0.5$)².

To estimate the data/simulation scale factor for the *pure* W-jet tagging efficiency, we need to separate the W-jets from combinatorial background. In order to understand the part of the $t\bar{t}$ jet mass distribution which contains “real” merged Ws and pure combinatorial background, we use the $t\bar{t}$ simulated sample. By matching the AK8 jet with the hadronic W at generator level, in a cone of $\Delta R < 0.3$, we can get the “real” merged Ws (matched) and pure combinatorial background (unmatched) shapes. The matched and unmatched samples that passed and failed the N-subjettiness selection $\tau_{21} < 0.5$ are then fit with the following chosen functions:

- $f_{\text{bkg}}(m_j) = F_{\text{ExpErf}} = e^{c_0 m_j} \cdot \frac{1 + \text{Erf}((m_j - a)/b)}{2}$ for both the unmatched-passed and unmatched-failed sample;
- $f_{\text{pass}}^{\text{sig}}(m_j) = F_{\text{2Gaus}}(m_j) = c_0 \cdot e^{-(m_j - m_{j0})^2/2\sigma_0^2} + c_1 \cdot e^{-(m_j - m_{j1})^2/2\sigma_1^2}$ for the matched-passed sample.
- $f_{\text{fail}}^{\text{sig}}(m_j) = F_{\text{Gaus}}(m_j) + F_{\text{Chebychev}}^{II}(m_j)$ for the matched-failed sample.

The W-tagger scale factors (SF_{HP}), for the high purity selection ($\tau_2/\tau_1 < 0.5$), are extracted estimating the cut efficiency on both data and simulated samples fitting, simultaneously, “pass” and “fail” samples:

$$L_{\text{pass}} = \prod_i^{N_{\text{evt}}^{\text{pass}}} \left[N_W \cdot \epsilon_{HP} \cdot f_{\text{pass}}^{\text{sig}}(m_j) + N_2 \cdot f_{\text{pass}}^{\text{bkg}}(m_j) + N_{\text{pass}}^{\text{sTop}} \cdot f_{\text{pass}}^{\text{sTop}} + N_{\text{pass}}^{\text{VV}} \cdot f_{\text{pass}}^{\text{VV}} + N_{\text{pass}}^{\text{wjet}} \cdot f_{\text{pass}}^{\text{wjet}} \right] \quad (12)$$

$$L_{\text{fail}} = \prod_i^{N_{\text{evt}}^{\text{fail}}} \left[N_W \cdot (1 - \epsilon_{HP}) \cdot f_{\text{fail}}^{\text{sig}}(m_j) + N_3 \cdot f_{\text{fail}}^{\text{bkg}}(m_j) + N_{\text{rmfail}}^{\text{sTop}} \cdot f_{\text{fail}}^{\text{sTop}} + N_{\text{fail}}^{\text{VV}} \cdot f_{\text{fail}}^{\text{VV}} + N_{\text{fail}}^{\text{wjet}} \cdot f_{\text{fail}}^{\text{wjet}} \right] \quad (13)$$

The ratio between data and simulation efficiencies are taken as the W-tagging scale factor.

$$SF_{HP} = \frac{\epsilon_{HP}(\text{data})}{\epsilon_{HP}(\text{sim})} \quad (14)$$

Considering that, both for data and simulation, $\epsilon_{HP} + \epsilon_{LP} + \epsilon_{fail} = 1$, the scale factor for low purity category can be defined as:

$$SF_{LP} = \frac{1 - \epsilon_{HP}(\text{data}) - \epsilon_{fail}(\text{data})}{1 - \epsilon_{HP}(\text{sim}) - \epsilon_{fail}(\text{sim})} \quad (15)$$

where, ϵ_{fail} is obtained fitting the failing samples ($\tau_2/\tau_1 > 0.75$) with a pdf given by the sum of two exponential, one for the fail-matched sample and another for the fail-unmatched one.

To extract the jet mass scale and resolution correction, we use the mean and sigma value of the narrower Gaussian in $f_{\text{pass}}^{\text{sig}}(x)$. Since we do not expect that the jet mass scale and resolution

²The purity categories are common to all three channels, and will be more explicitly treated in Sections 6.6, 6.7 and 6.8

530 should differ between electron and muon channels, we fit the muon and electron data simulta-
531 neously, constraining the mean and sigma of the narrower Gaussian to be the same between
532 electron and muon channels during fitting.

DRAFT

533 6 Analysis Strategy

534 6.1 Strategy Overview

535 As previously mentioned, the object of this search is the production of heavy resonances, with
 536 masses above approximately 1 TeV and above, decaying into pairs of massive bosons (W, Z), of
 537 which at least one decays hadronically ($W \rightarrow q\bar{q}', Z \rightarrow q\bar{q}$). In this note we detail the Phys14
 538 studies for only three cases:

- 539 • The $W_{\text{lep}} V_{\text{had}}$ case, hereafter referred to as the VW channel.
- 540 • The $Z_{\text{lep}} V_{\text{had}}$ case, hereafter referred to as the VZ channel.
- 541 • The $V_{\text{had}} V_{\text{had}}$ case, hereafter referred to as the VV and/or hadronic channel.

542 Since the masses of the W and Z bosons are very close, we choose to not try to distinguish
 543 between them in the hadronically-decaying case. Instead, the analyses will interpret a hadronic
 544 V boson as either a W or a Z , and put limits in the corresponding model.

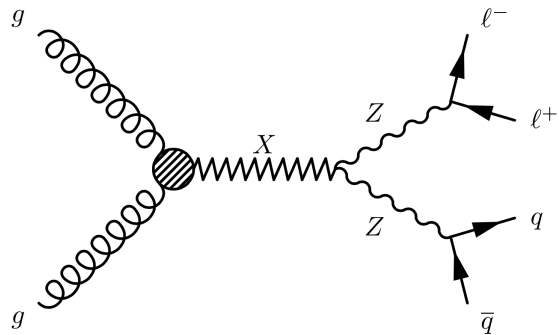
545 As discussed before, one of the main characteristics of this analysis is that, due to high mass of
 546 the BSM resonances, the bosons produced in the reaction $X \rightarrow VV$ have generally very high
 547 energy and very high p_T – in the jargon, they are called *boosted bosons*. For the leptonic decays,
 548 this phenomenon leads to high- p_T leptons and high E_T^{miss} (in the case of a W boson) or pairs of
 549 high- p_T leptons (in the case of a Z boson). The W boson case can be treated with techniques
 550 analogous to those used in analyses like W' – special reconstruction and identification for high
 551 energy leptons and MET corrections. The Z boson case presents an extra difficulty: for higher
 552 resonance masses, the leptons from the Z boson become very close together (very small ΔR) and
 553 inefficiencies may arise due to misassignment of hits (for muons) and merging of calorimetric
 554 clusters (for electrons). The techniques to minimize those effects are described in Sections 5.1
 555 and 5.2 and are similar to those used in Run 1.

556 On the side of the hadronic decay, a similar situation arises. Due to the close ΔR between the
 557 quark products of the decay of the boson, the products of the showering and hadronization
 558 appear on the detector as a single hadronic jet. That jet, however, has internal substructure
 559 which can be characterised by its invariant mass and by the energy flow inside the jet. The invariant
 560 mass, especially after the application of techniques to reduce the effect of low-energy and
 561 collinear emissions, offers a clear distinction between boosted bosons and jets from pure QCD
 562 processes; the usage of substructure allows for fine selection on top of that. We plan on using
 563 similar techniques as those used in Run 1, as described in Section 5.3.

564 The analysis tries to reconstruct two boson candidates, either hadronic or leptonic, and combines
 565 them into a resonance candidate. In general, there may be more than one resonance
 566 candidate reconstructed in the same event. This is usually because more than one jet is tagged
 567 as a V boson; more rarely, multilepton events may contain more than one leptonic W or Z .
 568 The procedure we use to choose among different candidates of the same type is to pick the
 569 one with largest p_T . The distribution of the invariant mass of the resonance candidates should
 570 cluster around the mass of the produced resonance, in case of signal events, while it should be
 571 a rapidly falling distribution in the case of background events. The statistical analysis of the
 572 data takes the form of a search for structures ("bumps") on top of that falling distribution.

573 6.2 VZ channel Preselection

574 The search for narrow resonances in the VZ semi-leptonic channel requires the selection of
 575 events with an intermediate state consisting of a pair of vector bosons V, where V can be either
 576 a W or Z boson. The final state contains a pair of opposite sign leptons ($\mu^+\mu^-$ or e^+e^-) and
 577 one jet. The jet in the final state results from the hadronization of two boosted quarks coming
 578 from the V boson. The pair of leptons come from the Z boson, and are expected to be close to
 579 each other. Figure 20 shows the diagram of the signal process, where X represents the exotic
 580 resonance decaying into a pair of Z bosons.



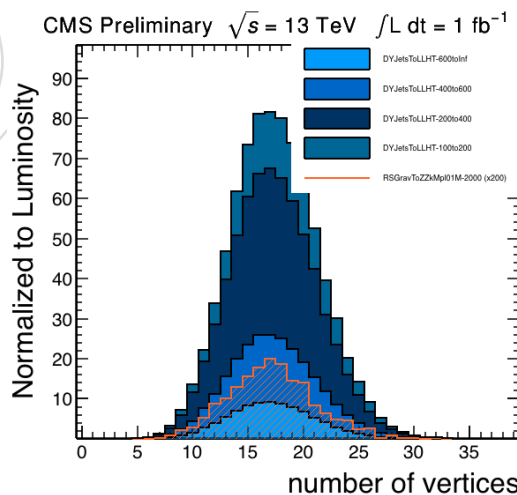
580 Figure 20: Exotic resonance decay in the ZZ semi-leptonic channel.

581 Offline primary vertex

582 Good events are required to have at least one good offline primary vertex with:

- 583 • longitudinal coordinate $|z| < 24$ cm
- 584 • transverse position $\rho < 2$ cm
- 585 • vertex fit variable $\chi^2 \neq 0$
- 586 • number of degrees of freedom $n_{\text{dof}} > 4$

The distribution in the number of primary vertices can be found in Figure 21.



587 Figure 21: Distribution of the number of primary vertices in the VZ semi-leptonic samples.

588 **Muon selection**

589 Muon candidates are selected from the `slimmedMuons` collection satisfying the following re-
590 quirements:

- 591 • $p_T > 50$ GeV and $|\eta| < 2.4$
- 592 • `isGlobalMuon` and `isPFMuon`
- 593 • `globalTrack.normalizedChi2 < 10`
- 594 • `globalTrack.hitPattern().numberOfValidMuonHits > 0`
- 595 • `globalTrack.hitPattern().numberOfValidPixelHits > 0`
- 596 • `numberOfMatchedStations() > 1`
- 597 • `db() < 0.2`

598 We are aware that this distribution is suboptimal for the VZ channel, and are working on de-
599 veloping a better set of muon identification criteria.

600 **Electron selection**

601 Electron candidates are selected from the `slimmedElectrons` collection satisfying the follow-
602 ing acceptance requirements:

- 603 • $p_T > 40$ GeV and $|\eta| < 2.5$
- 604 • $|\eta_{SC}| < 1.442$ or $|\eta_{SC}| > 1.566$

605 During the preselection we don't include any further electron identification. As discussed be-
606 fore, the EGamma POG recommendation for high- p_T electrons is not an option for us, because
607 of the detector-based isolation included in HEEP which reduces the efficiency of our boosted
608 signal. Alternatively, the particle flow isolation could be more appropriate, as shown in Fig-
609 ure 11.

610 **Leptonic Z selection**

611 Selected Z boson candidates satisfy the following requirements:

- 612 • $p_T^{\ell\ell} > 100$ GeV
- 613 • $70 < m_{\ell\ell} < 110$ GeV

614 Figure 22 shows kinematic distributions of the leptonic Z boson. The p_T of the Z boson peaks
615 around 1000 GeV for the signal sample, while the background peaks at a lower value around
616 200 GeV. The invariant mass in both cases peaks around 90 GeV which is the expected value of
617 the Z boson invariant mass.

618 The distribution of the transverse momentum of the leptons and the ΔR separation is shown
619 in Figure 23. In the ΔR distribution we observed a peak below 0.5, which is a characteristic
620 signature of boosted leptons.

621 **Hadronic V selection**

622 The selected jet candidates satisfy the following requirements:

- 623 • $p_T > 100$ GeV and $|\eta| < 2.4$
- 624 • Clean from overlaps with muons and electrons

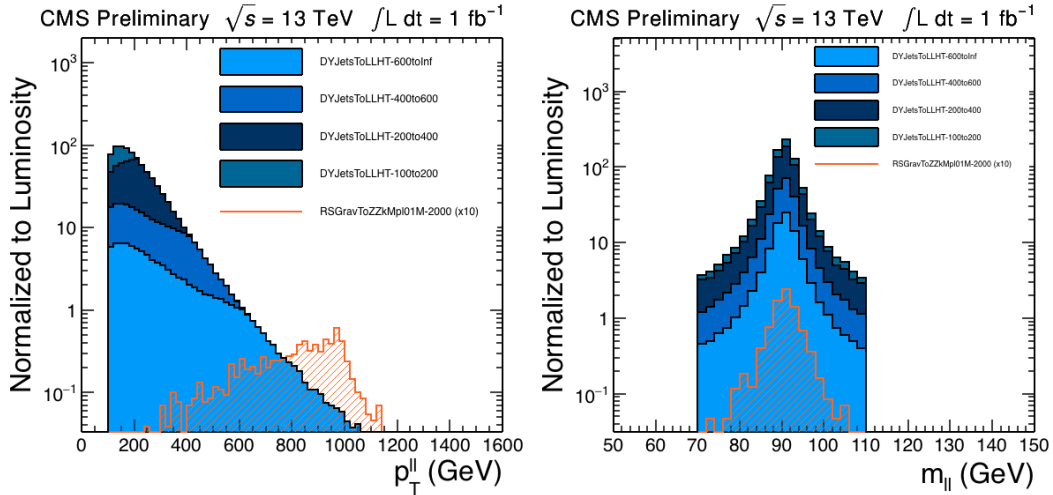


Figure 22: Distribution of the transverse momentum (left) and invariant mass (right) of the leptonic Z boson.

625 Figure 24 shows the distributions of the jet transverse momentum and the pruned mass. The jet
 626 mass is very powerful to discriminate signal events from the dominating Z+jets background,
 627 and allow us to define two regions:

- 628 • **Signal region:** $70 < M_J < 110 \text{ GeV}$
 629 • **Sideband region:** $50 < M_J < 70 \text{ GeV}$

630 VZ candidate reconstruction

631 Those events containing at least one leptonic Z candidate and one hadronic V candidate, are
 632 kept for reconstructing a VZ candidate. The preselection ends with a requirement in the VZ
 633 invariant mass:

- 634 • $M_{ZZ} > 180 \text{ GeV}.$

635 The distribution of the VZ invariant mass is shown in Figure 25. The analysis of this distribution
 636 is fundamental to determine the sensitivity of the analysis. In Section 8.2, we will use a
 637 data-driven technique to determine the normalisation and the shape. Finally, we will exploit
 638 all this information in Section 8.5 for the obtention of the expected limits.

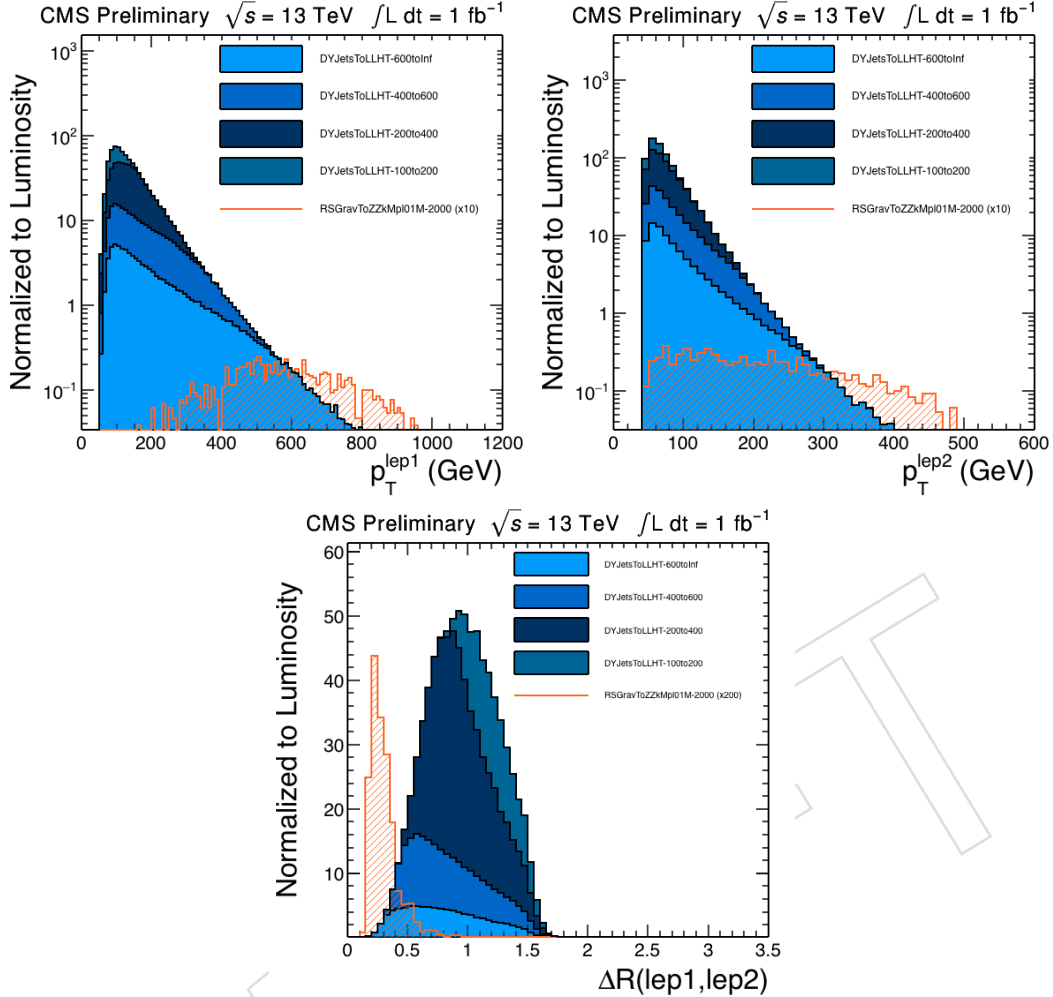


Figure 23: Distribution of the transverse momentum for the leading (top-left) and sub-leading (top-right) leptons. ΔR separation (bottom).

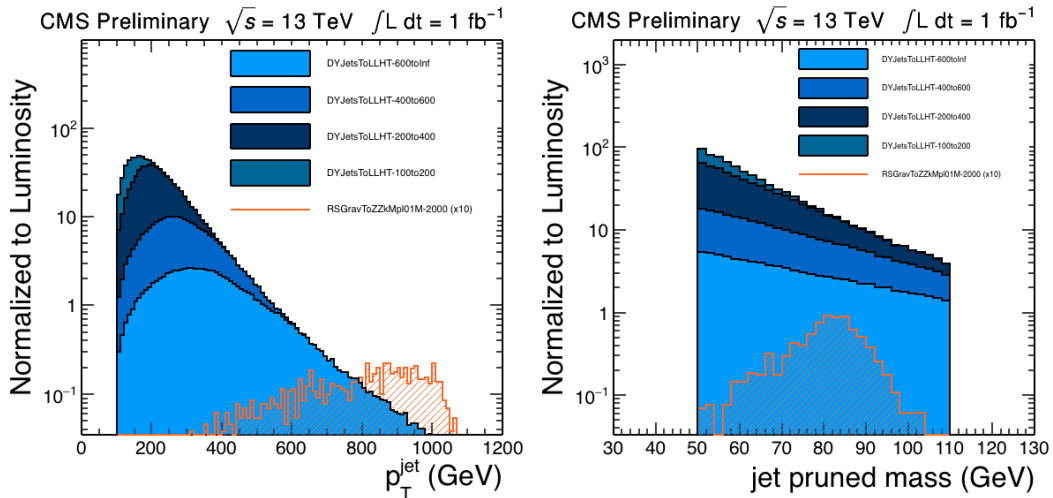


Figure 24: Distribution of the transverse momentum (left) and invariant mass (right) of the hadronic Z boson.

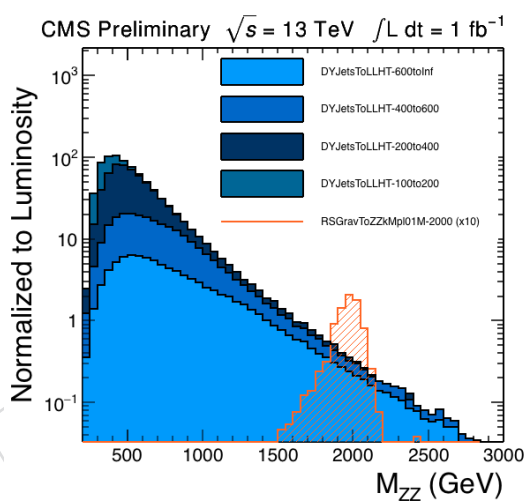


Figure 25: Distribution of the invariant mass of the reconstructed candidate after the preselection.

639 **6.3 VW channel Preselection**

640 For the search for in the VW channel, the final state contains one lepton (electron or muon),
 641 one fat jet and E_T^{miss} . The lepton and E_T^{miss} come from the W boson, and the jet is from the
 642 hadronization of two boosted quarks coming from the V boson.

643 **Lepton selection**

644 For the muon identification and reconstruction of muon momentum assignment we follow
 645 the recommendations of the Muon POG, as described in Section 5.2. We select Tight muon
 646 candidates passing the HighPT muon ID+ISO with $p_T > 40 \text{ GeV}$ and $|\eta| < 2.4$. Loose muon
 647 candidates (used for lepton veto) are required to pass the HighPT muon ID+ISO with $p_T >$
 648 20 GeV and $|\eta| < 2.4$.

649 For the electron identification we select Tight electron candidates passing the HEEP 5.1 electron
 650 ID+ISO with $p_T > 90 \text{ GeV}$ and $0.0 < |\eta| < 1.442$ OR $1.56 < |\eta| < 2$. Loose electron candidates
 651 (used for the lepton veto selection) are required to pass the HEEP 5.1 electron ID+ISO with p_T
 652 $> 35 \text{ GeV}$ (this p_T cut is included by default in the HEEP 5.1 selection) and the same η range of
 653 the tight electrons.

654 Notice that in both cases the p_T threshold will be modified to take into account the tighter
 655 triggers which will be deployed on data.

656 **Jet Selection**

657 Jets are reconstructed from the list of particle flow candidates reconstructed in the event, as
 658 described in Section 5.3. We use two jet collections:

- 659 • anti- k_T algorithm with distance parameter $R = 0.8$ (AK8) to select V candidates de-
 660 caying to jets in boosted regime;
- 661 • anti- k_T algorithm with distance parameter $R = 0.4$ (AK4) to require or veto the pres-
 662 ence of b-tagged jets in the event.

663 In all cases, we use jets with charged hadron subtraction jets. All jets are corrected applying the
 664 L1L2L3 corrections for simulation, derived by the JetMET POG and available by the default in
 665 the samples.

666 For the fat jets which give rise to the hadronic V candidates, we select AK8 jet candidates with
 667 $p_T > 100 \text{ GeV}$ and $|\eta| < 2.4$. In addition, jets are subject to the standard loose jet identification
 668 criteria, as described in Section 5.3. If an AK8 jet is within $\Delta R < 1.0$ of any tight electron or
 669 tight muon defined in the previous sections, the jet is not used in the analysis.

670 For additional jets in the event, we select AK4 jets with $p_T > 30 \text{ GeV}$ and $|\eta| < 2.4$, again passing
 671 the loose jet identification criteria. Additionally, if an AK4 jet is within $\Delta R < 0.3$ of any tight
 672 electron or tight muon, or $\Delta R < 0.8$ of any selected AK8 jets, the jet is not used in the analysis.
 673 The main usage of these jets is to veto b-tagged jets in order to minimize $t\bar{t}$ and single
 674 top background.

675 **Event selection**

676 We report below the final event selection for both muon channel and electron channel:

- 677 1. one charged lepton: as defined in the previous sections;
 678 2. lepton veto: no additional loose electron or muon;

- 679 3. missing transverse energy: an additional requirement $E_T > 80$ GeV for the electron chan-
- 680 nel and $E_T > 40$ GeV for the muon channel.
- 681 4. leptonic W p_T : the p_T of reconstructed leptonic W must be greater than 200 GeV. This cut
- 682 is required to select the boosted W topology;
- 683 5. hadronic V p_T : the p_T of reconstructed hadronic V (AK8 leading jet) must be greater than
- 684 200 GeV. This cut is required to select the boosted W topology;
- 685 6. btag veto: the event is required to have no AK4 jets tagged as b-jet accordingly with the
- 686 CSVv2 algorithm, medium working point.
- 687 7. diboson-like topology:
- 688 • $\Delta R(\ell, W_{\text{had}}) > \pi/2$
 - 689 • $\Delta\phi(W_{\text{had}}, E_T^{\text{miss}}) > 2$
 - 690 • $\Delta\phi(W_{\text{had}}, W_{\text{lep}}) > 2$

691 Furthermore, we define three orthogonal samples of events using the reconstructed pruned jet

692 mass of the V hadronic candidate:

- 693 • Signal region: $65 < m_{\text{jet}}^{\text{pruned}} < 105$ GeV;
- 694 • Lower sideband region: $40 < m_{\text{jet}}^{\text{pruned}} < 65$ GeV;
- 695 • High sideband region: $105 < m_{\text{jet}}^{\text{pruned}} < 130$ GeV;

696 Those regions will be later used for the background estimation.

697 With all the selections mentioned, Figures 26 to 29 show the various kinematical distribution

698 relevant at the preselection.

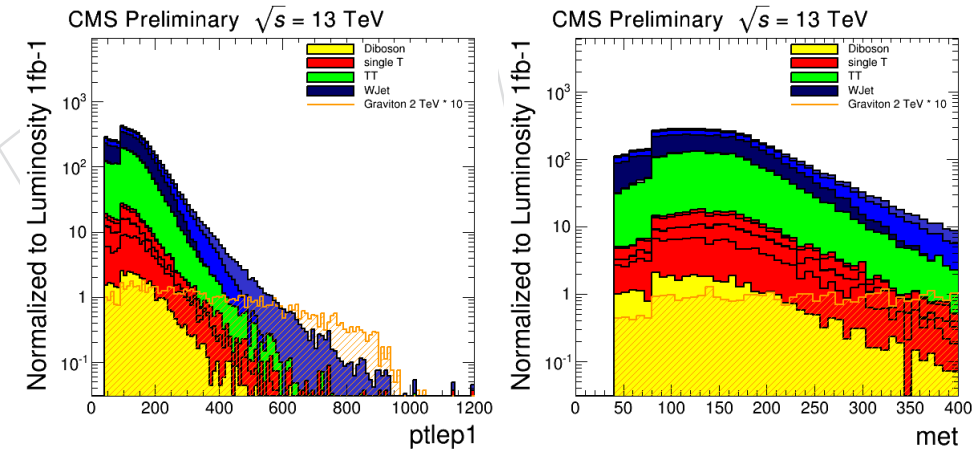


Figure 26: Distribution of the transverse momentum of lepton (left) and the E_T^{miss} (right).

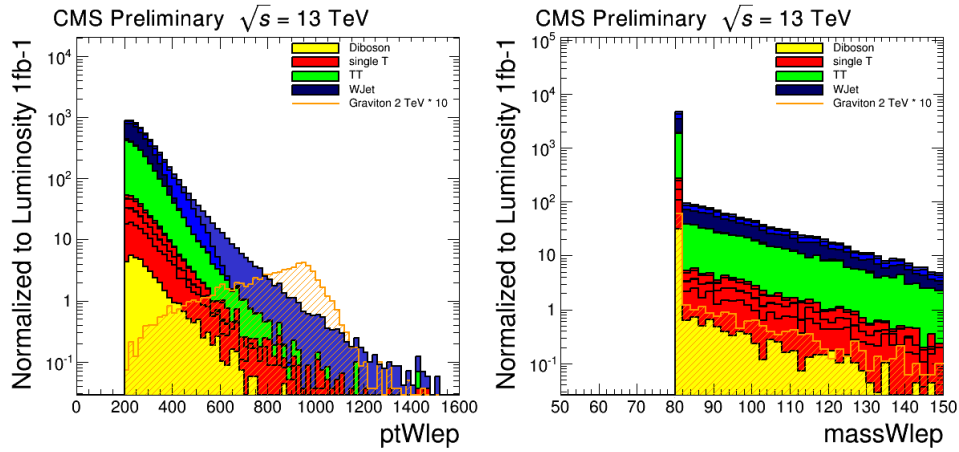


Figure 27: Distribution of the transverse momentum (left) and invariant mass (right) of the leptonic W boson.

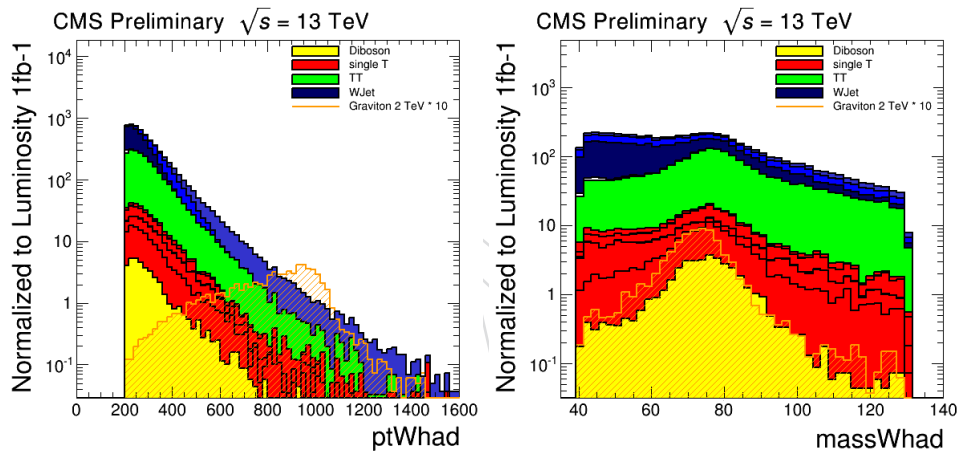


Figure 28: Distribution of the transverse momentum (left) and invariant mass (right) of the hadronic V boson.

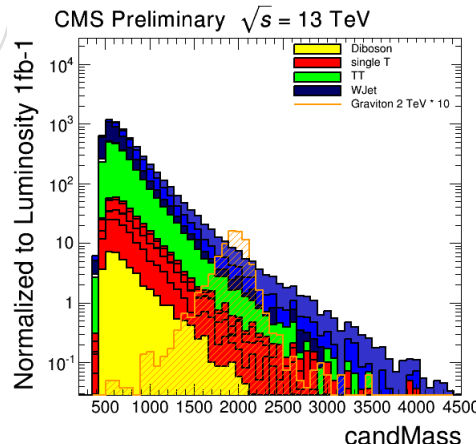


Figure 29: Distribution of the invariant mass of the reconstructed candidate after the preselection.

6.4 Dijet channel Preselection

Events in the all hadronic channel are selected by requiring at least two jets with $p_T > 30 \text{ GeV}$ and $|\eta| < 2.4$, where the two highest p_T jets in the event are selected as potential vector boson candidates. The p_T and η distributions for signal and for background can be seen in Figure 30 showing how the jet increase in p_T and become more central as the resonance mass increases.

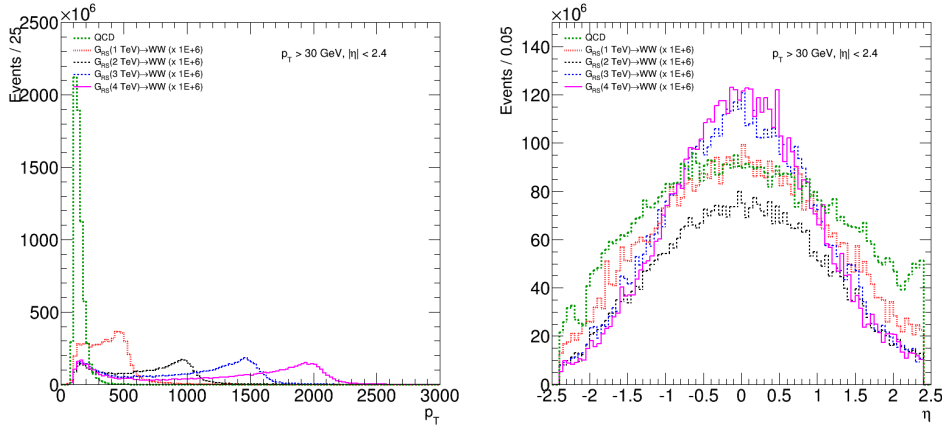


Figure 30: Jet p_T (left) and η (right) for the two leading jets in the event after loose jet ID, p_T and η cuts are applied. A cross section of 1 pb is assumed for the signal.

703

704 Figure 31 shows the dijet invariant mass spectrum for signal and background after the preselec-tions are applied.

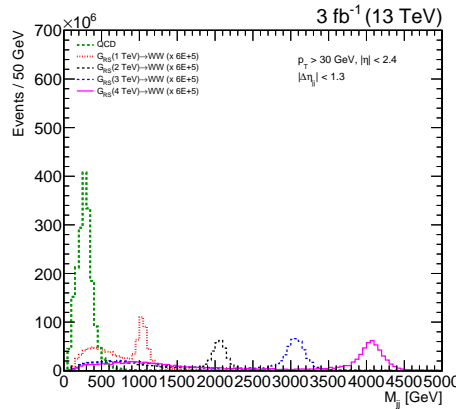


Figure 31: The dijet invariant mass for the two leading jets after preselections are applied. A cross section of 1pb is assumed for the signal.

705

706 To insure a low contribution to the overall systematic uncertainty due to triggering, the two
707 selected jets are required to have an invariant mass $M_{jj} > 1040 \text{ GeV}$ for a trigger efficiency of
708 at least 99%. The two jets with the highest p_T in the event are further required to have a sepa-
709 ration of $|\Delta\eta| < 1.3$ in order to reduce the QCD multijets background. The $|\Delta\eta_{jj}|$ spectrum for
710 signal and background events is shown in Figure 32. From this distribution a slightly higher
711 $|\Delta\eta_{jj}|$ threshold than the previously used 1.3 seems to be preferred, but it needs to be pointed
712 out that these distributions are for the RS1 Graviton only and do not include the bulk Graviton
713 model. Also, these samples are simulated with PYTHIA and may not have a full-fledged mod-
714 elling of the angular distribution; the main samples foreseen for Run 2 use MADGRAPH, and

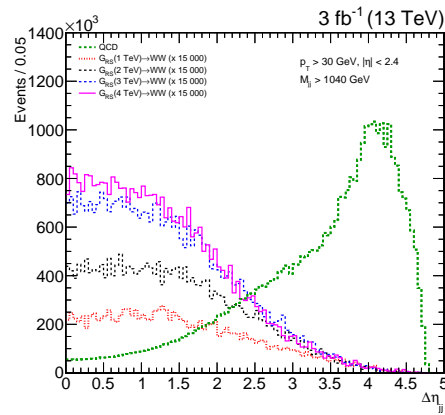


Figure 32: $\Delta\eta$ between the two leading jets for signal and for the QCD background. A cross section of 1pb is assumed for the signal.

715 a comparison between the two will be performed as soon as these samples become available.
 716 The jet angular distributions will also differ for a bulk Graviton model, G_{bulk} , as in this model
 717 the vector bosons are preferentially produced longitudinally polarised, while G_{RS} favours pro-
 718 duction of transversely polarised W/Z bosons. Also, the $|\Delta\eta_{jj}|$ threshold optimisation will be
 719 redone when bulk Graviton samples become available.

DRAFT

720 6.5 N-subjettiness Optimization

721 Discrimination between jets coming from hadronic decay of a V boson and those from QCD
 722 multijets processes is additionally enhanced by introducing selection on the 2- to 1-subjetness
 723 ratio τ_{21} . The optimisation of the selection on this variable has been performed for the 8 TeV
 724 analysis and yielded an event classification in two categories:

- 725 • **High Purity (HP)** events, where the hadronic V has τ_{21} values in the 0–0.5 range
- 726 • **Low Purity (LP)** events, where the hadronic V has τ_{21} values in the 0.5–0.75 range

727 For the 13 TeV iteration of the analysis we have performed similar optimisation for the selec-
 728 tion on τ_{21} again using Punzi's significance as figure of merit, using the VW channel structure.
 729 Additionally, the conclusions are confirmed with the full analysis chains including calculation
 730 for the expected limits on RS graviton cross section. Optimisation of the τ_{21} selection using
 731 Punzi's significance is performed after applying the signal selection as described in Section 6.3
 732 with additional requirement on the reconstructed m_{WW} to be within $\pm 15\%$ of the target reso-
 733 nance mass. Then the significance is calculated for each value of the τ_{21} in the range 0–1 with
 734 steps of 0.2. The calculation is shown on Figure 33 for graviton masses in the range 1 to 4 TeV,
 735 from which is clear that the optimal cut on τ_{21} depends on the RS graviton mass. For the 13
 736 TeV analysis we plan to once again categorize the events in terms of τ_{21} ranges, thus for this
 737 Early Analysis document we investigate the possibility to use a fixed cut value on τ_{21} for a wide
 738 range of resonance masses; for future studies we would also like to consider a p_T -dependent
 739 τ_{21} threshold with flat efficiency, which could make the category sensitivity independent of the
 740 resonance mass considered. Figure 34 shows the comparison between a fixed upper value of
 741 τ_{21} and the optimal value (for the given RS graviton mass) in the form of ratio of the signifi-
 742 cances for the two cases. The upper cut value of 0.5 is optimal for low RS graviton masses, 0.75
 743 is best for higher masses, while 0.6 is the optimal one for the overall range.

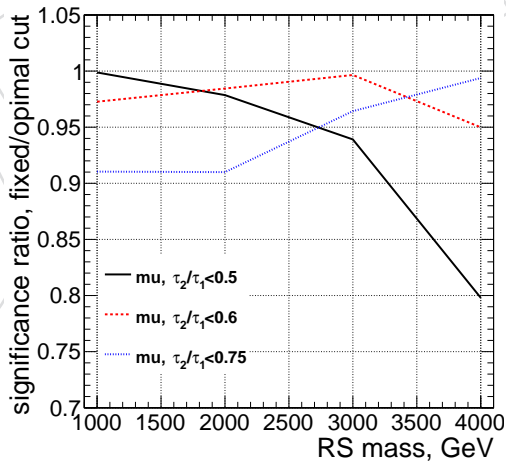


Figure 33: Punzi's significance as a function of upper cut on τ_{21} for RS graviton mass in the range 1–4 TeV. Muon channel is shown. Dependence is very similar for the electron channel.

744 Another study for the τ_{21} cuts optimisation was performed taking the expected limits on the RS
 745 graviton cross section as the figure of merit. This study investigates the possibility to use one or
 746 two categories in terms of selection on τ_{21} . In the case of two categories the combination is done
 747 at the limit setting step. Figure 35 shows the upper expected limits on the RS graviton cross
 748 section for a few cases of single category. Figure 36 and Table 5 summarise the comparison
 749 between several single and two categories cases. The optimal choice would be to use combi-

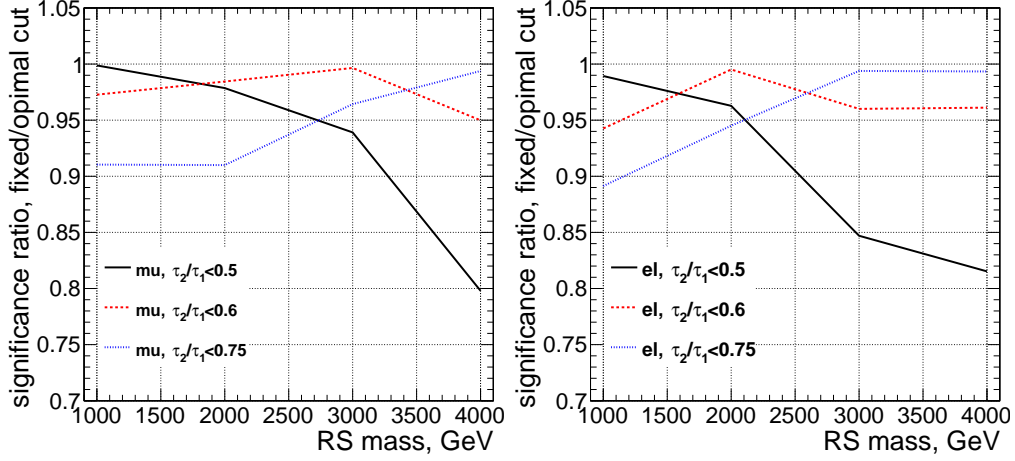


Figure 34: Ratio of Punzi's significance for a fix and mass-dependent optimal upper cut on the τ_{21} as a function of RS graviton mass for muon (left) and electron (right) channels.

750 nation of high purity [0,0.5] and low purity (0.5,0.75] categories for 1–2 GeV RS graviton mass
751 range and combination of [0,0.6] and (0.6,0.8] for 3–5 TeV RS graviton mass range.

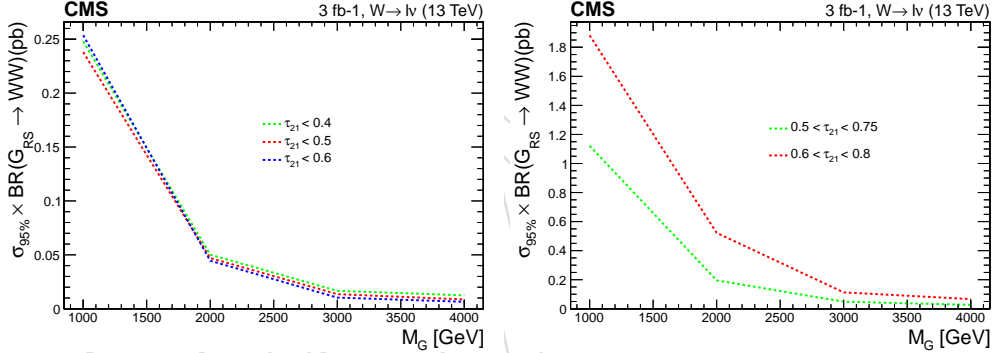


Figure 35: Expected upper limit on RS graviton cross section for several High Purity(left) and Low Purity(right) categories for τ_{21} variable.

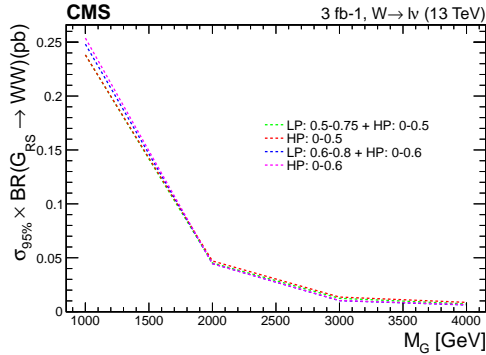


Figure 36: Expected upper limit on RS graviton cross section for several categories for τ_{21} variable. Several choices of single category and combination of two categories are shown.

Table 5: Expected upper limit on RS graviton cross section for several categories for τ_{21} variable. Several choices of single category and combination of two categories are shown.

Expected Limit	HP:0.5	HP:0.5 + LP:0.5-0.75	HP:0.6	HP:0.6 + LP:0.6-0.8
1 TeV	0.2381	0.2381	0.2538	0.2481
2 TeV	0.0470	0.0452	0.0445	0.0445
3 TeV	0.0136	0.0124	0.0104	0.0102
4 TeV	0.0086	0.0072	0.0065	0.0062

752 6.6 VZ channel Optimization and Final Selection

753 The jet substructure quantity $\tau_{21} = \tau_2/\tau_1$ is an important discriminator between V -jets and
 754 QCD jets. According to Figure 37, the background distribution of τ_{21} has a peak in the region
 755 above 0.5, while the signal distribution reaches a maximum around 0.35. Moreover, the signal
 756 distribution is depopulated for values of $\tau_{21} > 0.75$. In view of this, the preselected events are
 757 classified in two categories:

- 758 • **High-purity category:** events with $\tau_{21} < 0.5$
- 759 • **Low-purity category:** events with $0.5 < \tau_{21} < 0.75$

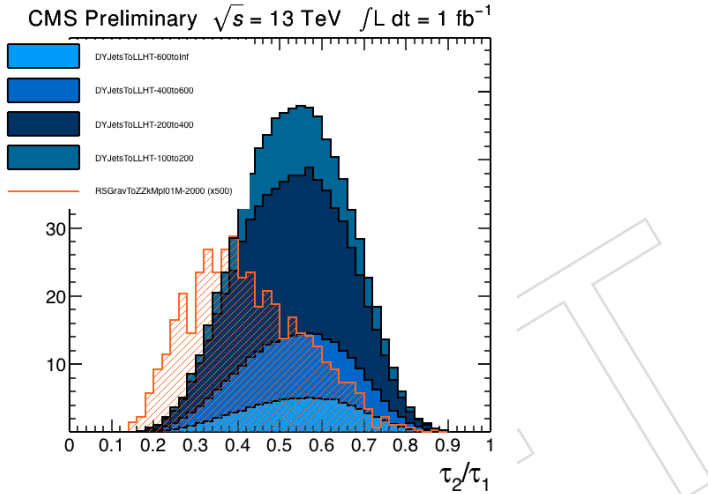


Figure 37: Subjettiness ratio τ_2/τ_1 for signal with $M_G = 2$ TeV and Z +jets background.

760 In Table 6, we present the efficiency of finding a preselected event in the high-purity or low-
 purity category.

Table 6: Efficiency of finding a preselected event in the high-purity or low-purity category.

Sample	High-purity	Low-purity
DYJetsToLL HT-100to200	0.38	0.59
DYJetsToLL HT-200to400	0.25	0.56
DYJetsToLL HT-400to600	0.39	0.57
DYJetsToLL HT-600toInf	0.36	0.56
RSGravToZZ M2000	0.72	0.27

761

762 For most of the optimisation studies, we will follow what is done in the VW channel, and
 763 described in the following sections.

764 6.7 VW channel Optimization and Final Selection

765 Optimization of the high pruned jet mass sideband

766 In the procedure of extraction of the W+jets normalization, the upper sideband in M_J is used
 767 in the fit on data, as will be demonstrated in Section . The definition of this upper sideband
 768 needs to be revisited, in order to deal with future extension of the analysis to the VH final state.
 769 Let's assume, for instance, the HVT model B as benchmark, where $W' \rightarrow WZ$ and $W' \rightarrow WH$
 770 have the same branching fractions. If the Higgs boson decays in the fully hadronic channel,
 771 its contribution enters in the mass window of the upper sideband used in the VW analysis
 772 (105–130 GeV), as one can see from fig. 38:

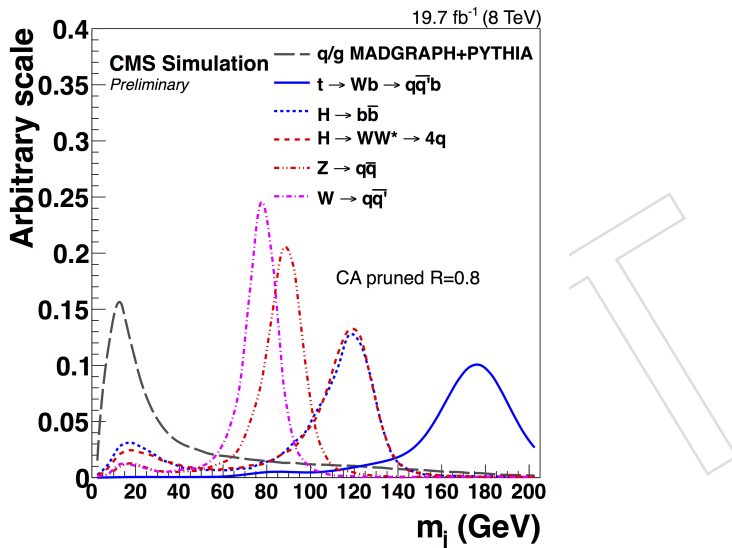


Figure 38: Contribution of the different hadronic decay channels for a W' boson. The contribution from the Higgs decay falls into the region around 110–140 GeV.

773 The contamination of the Higgs boson in the upper sideband can lead to some biases in the
 774 fit and in the extrapolation of the W+jets normalization into the signal region, so it is better to
 775 discard this region from the fit. An optimization study on this topic has been performed, trying
 776 different mass windows for this region. For each of them, we evaluate the impact on the fit and
 777 also on the final expected limit, in order to be sure that we do not lose sensitivity if we change
 778 the definition of the mass window. The expected limit has been computed for a RS Graviton
 779 with $M = 2$ TeV and using 1 fb^{-1} of statistics at 13 TeV.

780 In Table 7 all tried configurations are listed, compared to the default solution. For each one,
 781 the expected limit obtained is reported. In Fig. 39, examples of the sideband fit for different
 782 solutions are shown.

783 As can be seen, no strange features in the fit are observed, when defining a different upper
 784 sideband. The signal region lower limit has also been moved from 65 to 60 GeV, in order to
 785 better take into account the shift of the W peak to lower mass with respect to its nominal value.
 786 From this study, looking also at Table 7, one can conclude that we can avoid the Higgs re-
 787 gion choosing a different upper sideband (for example, [140–155] GeV) without losing analysis
 788 sensitivity.

Table 7: Summary of the different configurations tried for the sideband study. For each solution, the window of the lower sideband, of the signal region, and of the upper sideband is reported, together with the value of the expected combined limit obtained. The first configuration in the table is the default one.

Low SB (GeV)	SR (GeV)	Upper SB (GeV)	Combined limit (ele+mu)
35-60	60-105	105-130	1.05
35-60	60-95	95-110	0.98
35-60	60-95	95-105	0.98
35-60	60-105	140-155	1.04

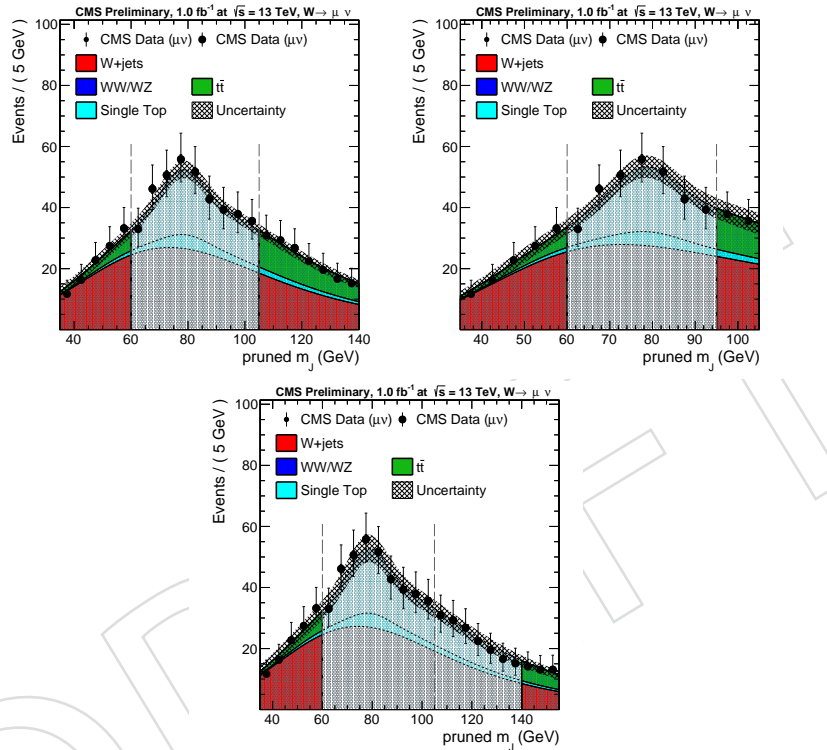


Figure 39: Examples of m_j fits to extract the W+jets normalization for the muon channel. Top left: default configuration (upper sideband: 105-130 GeV). Top right: configuration with upper sideband from 95 to 105 GeV. Bottom: upper sideband from 140 to 155 GeV.

789 Optimization of the low pruned jet mass sideband

790 In order to reduce the systematical uncertainty coming from the lack of statistics in the M_j
 791 sidebands used for the background estimation, we attempt to reduce it extending the low M_j
 792 sideband where a larger contribution from W+jets background is expected. In particular, we
 793 investigate here the option of extending the low M_j sideband from the default range [40,60]
 794 GeV to a range given by [20,60] GeV for both the LP ($\tau_{21} \in [0-0.5]$) and the HP ($\tau_{21} \in [0.5-$
 795 0.75]) categories. Figure 40 shows the M_j fits to extract the W+jets normalization in the LP and
 796 HP categories for the default and the extended M_j low sideband, while Figure 41 shows the
 797 comparison of the expected limits in 3 fb^{-1} of integrated luminosity for the two options. The
 798 results of the comparison are listed in Tables 8 and 9 for the HP and LP category respectively.
 799 The expected sensitivity does not show any significant variation and the M_j fits are stable when
 800 extending the sideband in both the HP and LP categories. The M_j fits are stable in both the
 801 categories for the two different options and the expected sensitivity in the HP category slightly

improves of about 9-14% at high masses when extending the low M_j sideband, while a less significant improvement of about 5-8% is expected in the LP category. One must remember that, as we move to softdrop for the V-tagging technology, these studies will have to be redone.

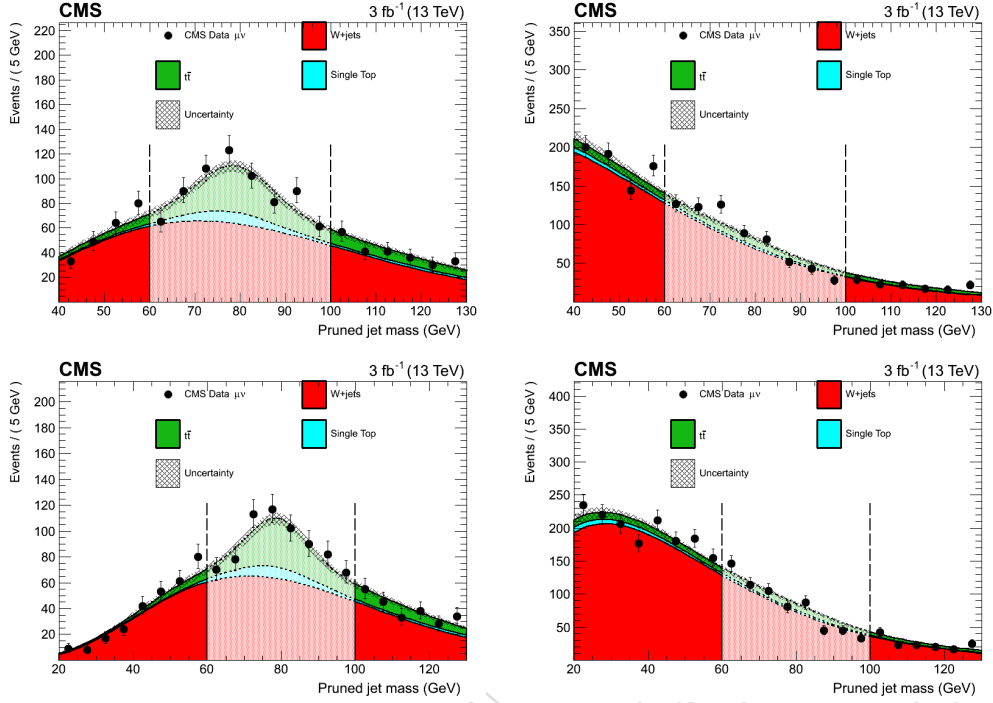


Figure 40: M_j fits to extract the $W+jets$ normalization. Top: default low sideband ($[40,60]$ GeV) in the HP (right) and LP (left) categories. Bottom: extended low sideband ($[20,60]$ GeV) in the HP (right) and LP (left) categories.

Table 8: Summary of the comparison between the sensitivity expected in 3 fb^{-1} of integrated luminosity in the HP category with the default low M_j sideband (first row) and the one expected when extending it to 20 GeV.

Low SB (GeV)	SR (GeV)	Upper SB (GeV)	Expected limits			
			1 TeV	2 TeV	3 TeV	4 TeV
40-60	60-100	100-130	0.238	0.047	0.014	0.009
20-60	60-100	100-130	0.238	0.043	0.012	0.008

805 Top mass veto optimization

In the analysis, we use a veto on the number of b-tag jets to suppress this contribution following the same strategy as in the Run 1 analysis. Nevertheless, the $t\bar{t}$ background contribution is expected to increase of a factor around 3.7 with respect to the 8 TeV analysis while the $W+jets$ background contribution increases of a factor around 1.7 only. Hence, given the particular and known signature of the top quark, other strategies have been studied to further reduce its contamination and gain additional sensitivity. In particular, following the same strategy as in Ref. [36], we exploit here the possibility to reconstruct the mass of both the hadronic and leptonic top quarks.

The hadronic and leptonic top quarks are easily identified exploiting the presence of one or more extra not b-tagged jets in most of the $t\bar{t}$ events (see Figure 42). In fact, given the selected “boosted” event topology, we expect the extra jet in the event to be close in the ϕ - η space to

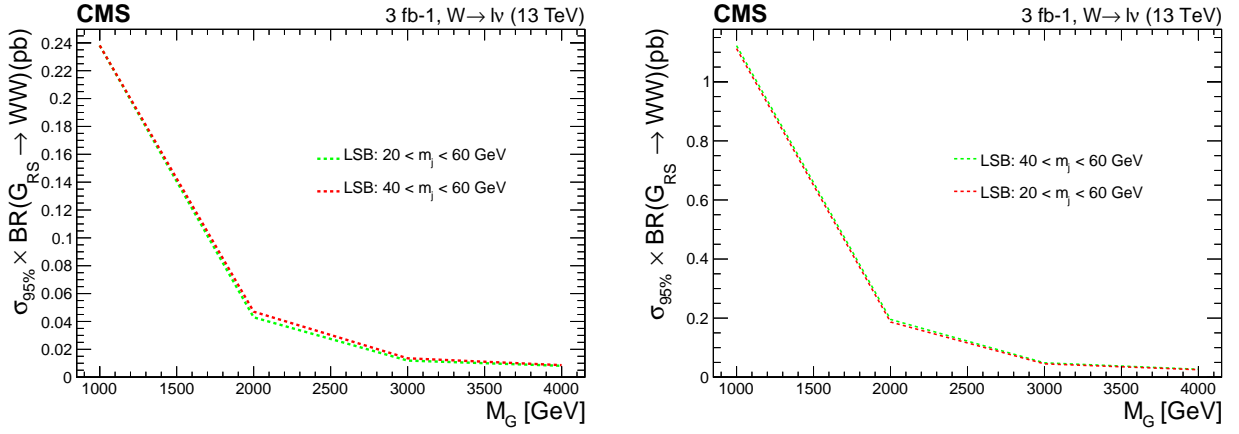


Figure 41: Comparison between the sensitivity expected in 3fb^{-1} of integrated luminosity in the HP (right) and LP (left) categories with the default low M_J sideband and the one expected when extending it to 20 GeV.

Low SB (GeV)	SR (GeV)	Upper SB (GeV)	Expected limits			
			1 TeV	2 TeV	3 TeV	4 TeV
40-60	60-100	100-130	1.123	0.196	0.049	0.027
20-60	60-100	100-130	1.113	0.187	0.045	0.025

Table 9: Summary of the comparison between the sensitivity expected in 3fb^{-1} of integrated luminosity in the LP category with the default low M_J sideband (first row) and the one expected when extending it to 20 GeV.

the selected hadronic W (but still outside the fat jet cone of 0.8) or to the selected lepton. In the first case we expect the hadronic top quark to be correctly reconstructed, while in the latter we expect the leptonic one to be the candidate. If more than one extra jet is present, the closest to the lepton is chosen to reconstruct the leptonic top quark, while the closest to the fat jet is chosen to reconstruct the hadronic one.

Once the top quarks are identified the invariant mass of the leptonic and/or hadronic top quark can be computed (see Section 5.6 for the reconstruction of the leptonic W), only when at least one extra jet is present in the event. Figure 43 shows the normalized distributions of the invariant mass of the hadronic (right) and leptonic (left) top mass, when the top reconstruction algorithm described above is applied to both signal and $t\bar{t}$ events after full selection. Since these distributions clearly exhibit a sharp peak around the top quark mass for the $t\bar{t}$ background, events can be rejected if the reconstructed invariant mass falls in a suitable window around the leptonic or the hadronic top quark peak.

The window is optimized scanning simultaneously the lower and the higher value for both the hadronic and leptonic top quark mass and for each configuration the Punzi's significance is calculated. In particular, the low value is chosen in the range [80,140] GeV in steps of 10 GeV, while the high value is chosen in the range [180,300] GeV in steps of 10 GeV. The optimization has been performed separately for different signal mass points applying a 15% window around the M_{WW} . Due to lack of statistics in the $t\bar{t}$ background sample for values of M_{WW} around and above 2 TeV the optimization was carried out for the 1 TeV signal mass point only. Figure 44 shows the Punzi's significance as a function of the signal efficiency in the muon and the electron categories for the 1 TeV signal mass point. The optimal working is chosen as follows:

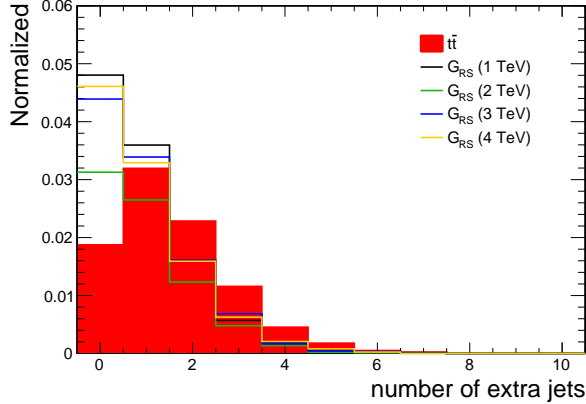


Figure 42: Normalized distribution of the number of extra not b-tagged jets in $t\bar{t}$ and signal events.

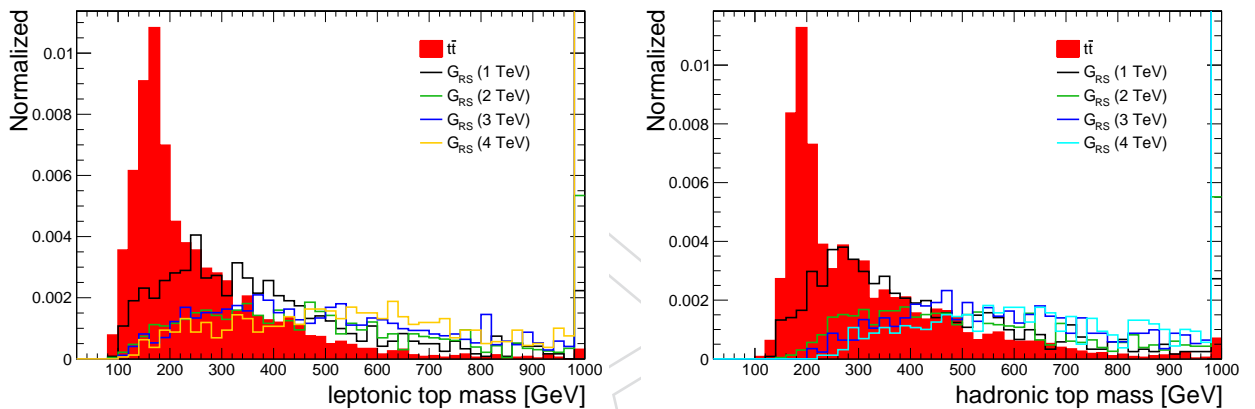


Figure 43: Normalized distributions of the reconstructed invariant mass of the leptonic (left) and hadronic (right) top quarks in $t\bar{t}$ and signal events.

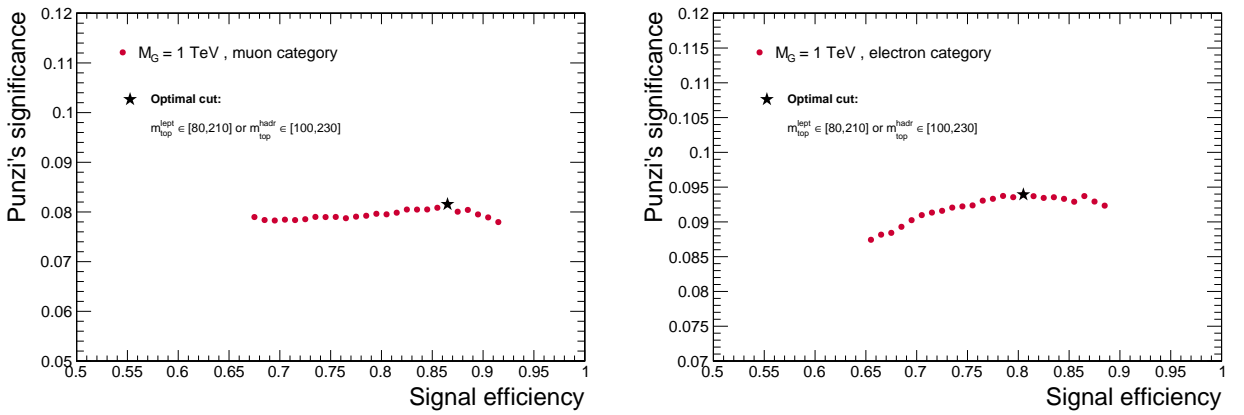


Figure 44: Punzi's significance as a function of the signal efficiency obtained for different windows around the hadronic and lepton top quark mass peaks. The chosen optimal working point is also shown.

$$80 < m_{top}^{lept} < 120 \text{ GeV} \text{ or } 100 < m_{top}^{hadr} < 230 \text{ GeV} \quad (16)$$

Figure 45 shows the effect of the veto on the top quark mass on the expected sensitivity in 3fb^{-1} of integrated luminosity and the results are summarized in Table 10. A gain in sensitivity of about 6% is expected at low masses (below 2 TeV) while the gain is negligible at high masses where a very small contribution from $t\bar{t}$ is expected.

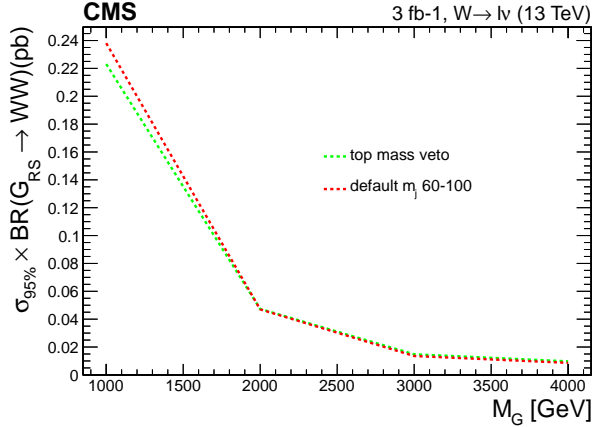


Figure 45: Comparison between the sensitivity expected in 3fb^{-1} of integrated luminosity with and without top mass veto applied after full selection.

	Expected limits			
	1 TeV	2 TeV	3 TeV	4 TeV
w/o top mass veto	0.238	0.047	0.0136	0.0086
w/ top mass veto	0.223	0.047	0.0148	0.0097

Table 10: Summary of the comparison between the sensitivity expected in 3fb^{-1} of integrated luminosity with and without (first row) top mass veto applied after full selection.

Summary of final selection

A summary of the final kinematic and jet substructure selection criteria is presented in Table 11.

6.8 Dijet channel Optimization and Final Selection

After all preselections are applied we take advantage of the W/Z tagging algorithm described in Section 5.7 to further separate boosted W/Z jets from the multijets background. Figure 46 shows the signal and background distribution for the two main variables used as input to the W/Z tagging algorithm, namely the pruned-jet mass (left) and the n-subjetiness τ_{21} variable. The signal pruned mass distribution peaks nicely around the W mass, while the multijets background spectrum is peaked at lower pruned masses. We therefore require the pruned-jet mass to be in a window around the W/Z mass between 60 and 100 GeV.

As the jet N-subjetiness and pruned mass are correlated, the discriminating power of τ_{21} is reduced after applying a cut on the pruned-jet mass. We therefore choose the τ_{21} cut that maximizes the signal significance for jets in the pruned mass window. As figure of merit we use the Punzi significance [37] defined as

$$P = \varepsilon_S \frac{1}{1 + \sqrt{B}} \quad (17)$$

Table 11: Summary of the VW channel final selection.

Selection	Value	Comments
Tight Lepton selection		
Electron p_T	$p_T > 90 \text{ GeV}$	
Muon p_T	$p_T > 50 \text{ GeV}$	
Electron η	$ \eta _{\text{SC}} < 2.5$ except [1.4442, 1.566] range	Avoid the ECAL gap.
Muon η	$ \eta < 2.1$	
Loose Lepton selection		
Electron p_T	$p_T > 35 \text{ GeV}$	
Muon p_T	$p_T > 20 \text{ GeV}$	
Electron η	$ \eta _{\text{SC}} < 2.5$ except [1.4442, 1.566] range	Avoid the ECAL gap.
Muon η	$ \eta < 2.4$	
AK8 jet selections		
Jet p_T	$p_T > 200 \text{ GeV}$	Used for hadronic W reconstruction
Jet η	$ \eta < 2.4$	
AK4 jet selections		
Jet p_T	$p_T > 30 \text{ GeV}$	Used for b-tag jet selection
Jet η	$ \eta < 2.4$	
E_T^{miss} selections		
E_T^{miss} (electron ch.)	$E_T^{\text{miss}} > 80 \text{ GeV}$	
E_T^{miss} (muon ch.)	$E_T^{\text{miss}} > 40 \text{ GeV}$	
Boson selections		
Pruned jet mass (signal)	$60 < m_{\text{jet}}^{\text{pruned}} < 100 \text{ GeV}$	
Pruned jet mass (low-mass sideband)	$40 < m_{\text{jet}}^{\text{pruned}} < 60 \text{ GeV}$	
Pruned jet mass (high-mass sideband)	$100 < m_{\text{jet}}^{\text{pruned}} < 130 \text{ GeV}$	
Leptonic W p_T	$p_T > 200 \text{ GeV}$	
Hadronic W p_T	$p_T > 200 \text{ GeV}$	
Back-to-back topology	$\Delta R(\ell, W_{\text{had}}) > \pi/2$, $\Delta\phi(W_{\text{had}}, E_T^{\text{miss}}) > 2$ $\Delta\phi(W_{\text{had}}, W_{\text{lep}}) > 2$	
Veto		
Number of loose electrons	0	in addition to tight lepton
Number of loose muons	0	in addition to tight lepton
Number of b-tag jets	0	CVS medium working point
Diboson selections		
2- to 1-subjettiness ratio (high purity)	$\tau_{21} < 0.50$	
2- to 1-subjettiness ratio (low purity)	$0.50 \leq \tau_{21} < 0.75$	

Figure 47 shows the τ_{21} distribution for jets after requiring the jet pruned mass to be between 60 and 100 GeV (left) and the corresponding Punzi significance as a function of τ_{21} cut for four different signal mass points.

The preferred τ_{21} cut for the four different signal mass points we have looked at is around 0.5 and we select “high purity” (HP) W/Z jets by requiring $0 < \tau_{21} \leq 0.5$. In order to enhance the overall sensitivity of the analysis, we add a low purity (LP) category for jets with $0.5 < \tau_{21} \leq 0.75$. As this analysis is sensitive to both (i) heavy resonances decaying into two vector bosons and (ii) excited quark resonances q^* decaying to qW and qZ, we look for events with both one single W/Z-tag and events with two W/Z-tags. Events with one W/Z tag are then defined according to these two categories. In the double W/Z tag category, events are always required to have one HP W/Z tag and are divided into LP and HP categories depending on whether the second jet is HP or LP. For this early analysis note, only expected results for the double tag category are shown. Figure 48 shows the expected limits with 10 fb^{-1} of Phys14 pseudo data using the HP (top left) or LP (top right) categories only and when adding the two (bottom) for double W/Z-tag events. A small gain in sensitivity is obtained when including the low purity category, especially for higher resonance masses.

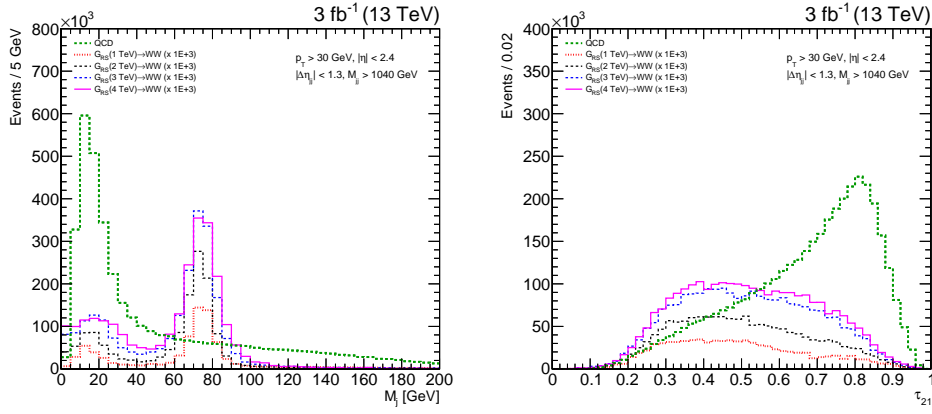


Figure 46: Pruned-jet mass (left) and τ_{21} distribution for signal and background for an integrated luminosity of 3 fb^{-1} . A 1 pb^{-1} cross section is assumed for the signal

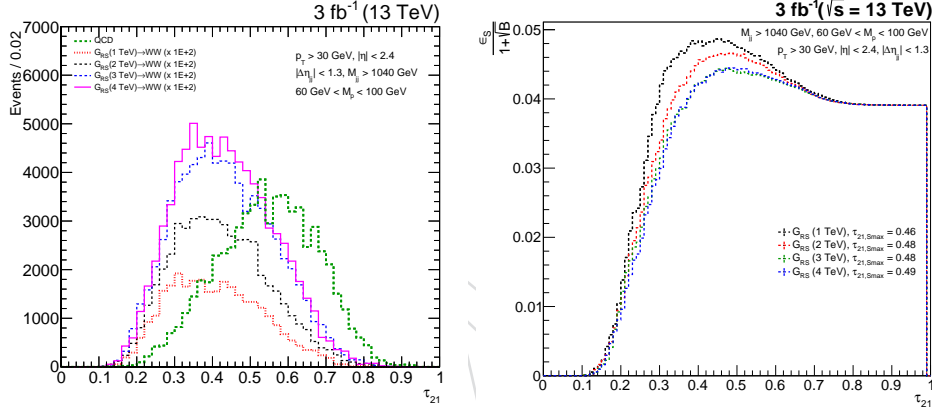


Figure 47: The left plot shows the τ_{21} distribution for jets in the pruned mass window. This is used as input for calculating the Punzi significance (right) for different cuts on the N-subjetiness ratio τ_{21} .

869 Figure 49 and 50 shows kinematic distributions for signal and background after all selections
 870 are applied for the HP category.

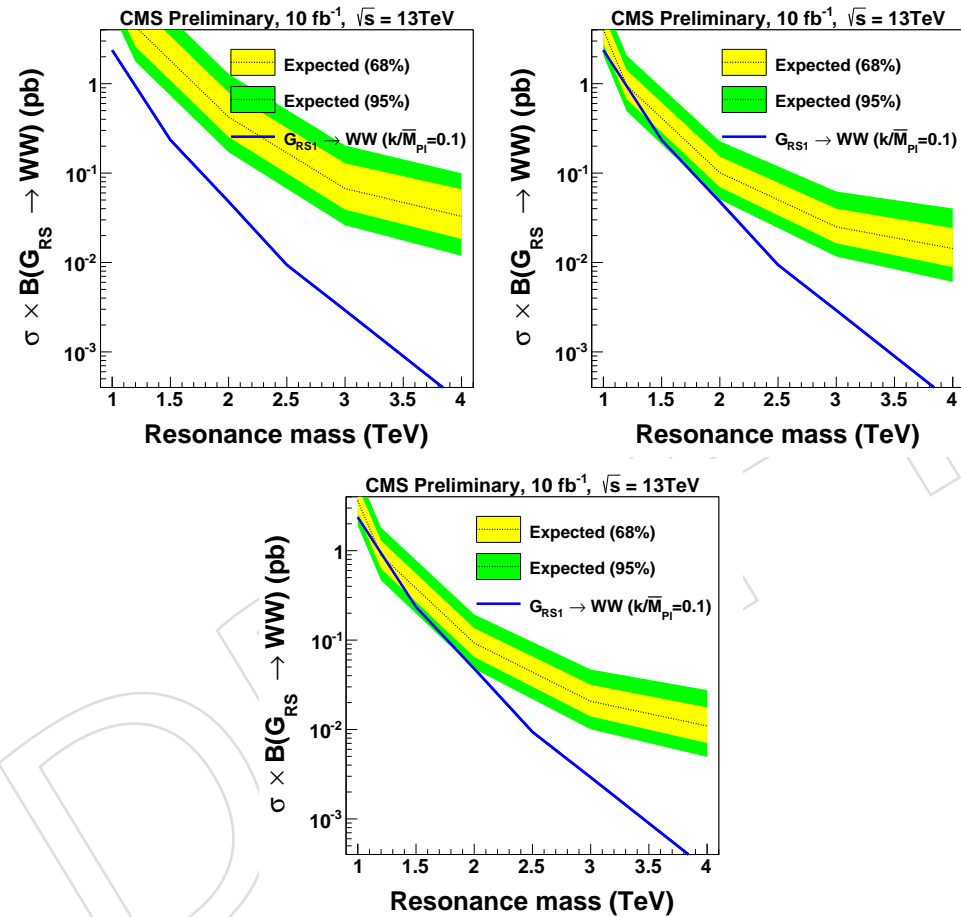


Figure 48: Expected limits for a luminosity of 10 fb^{-1} for the LP category (top left), HP category (top right) and when combining the two (bottom) on the resonance production cross section. Adding the LP category leads to a gain in sensitivity especially at higher masses.

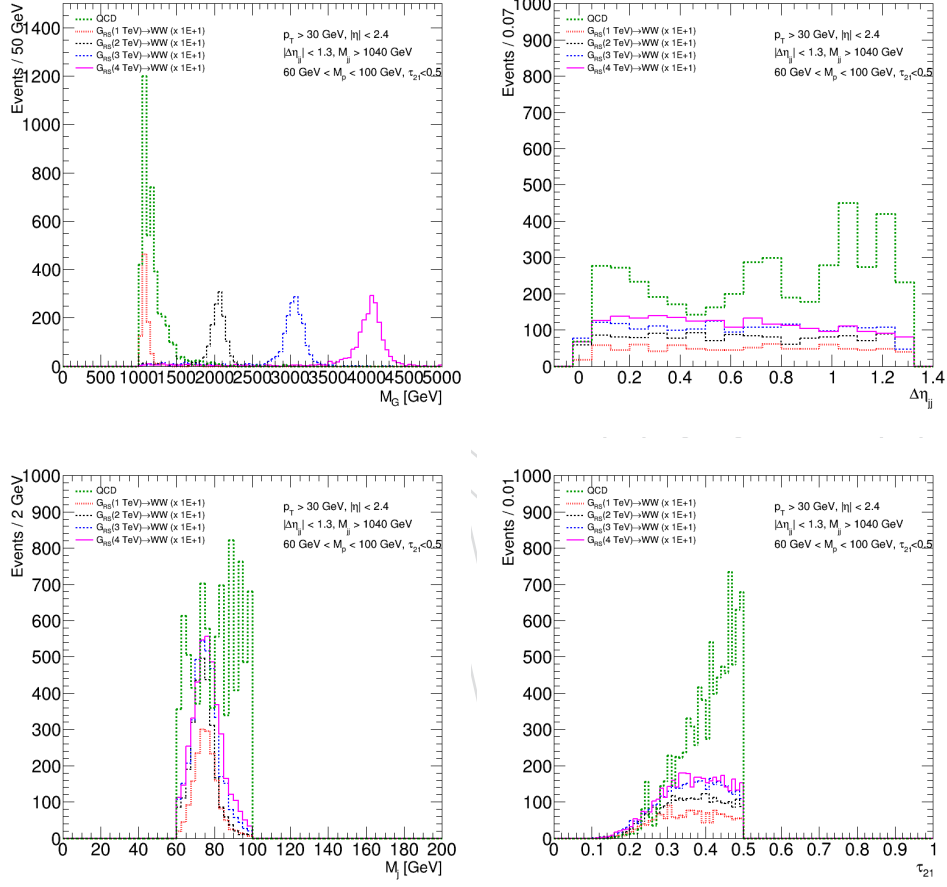


Figure 49: Control plots after full selection has been applied for the dijet invariant mass (top left), $\Delta\eta$ between the two V candidate jets (top right), jet pruned mass (bottom left) and jet τ_{21} (bottom right) for the HP category.

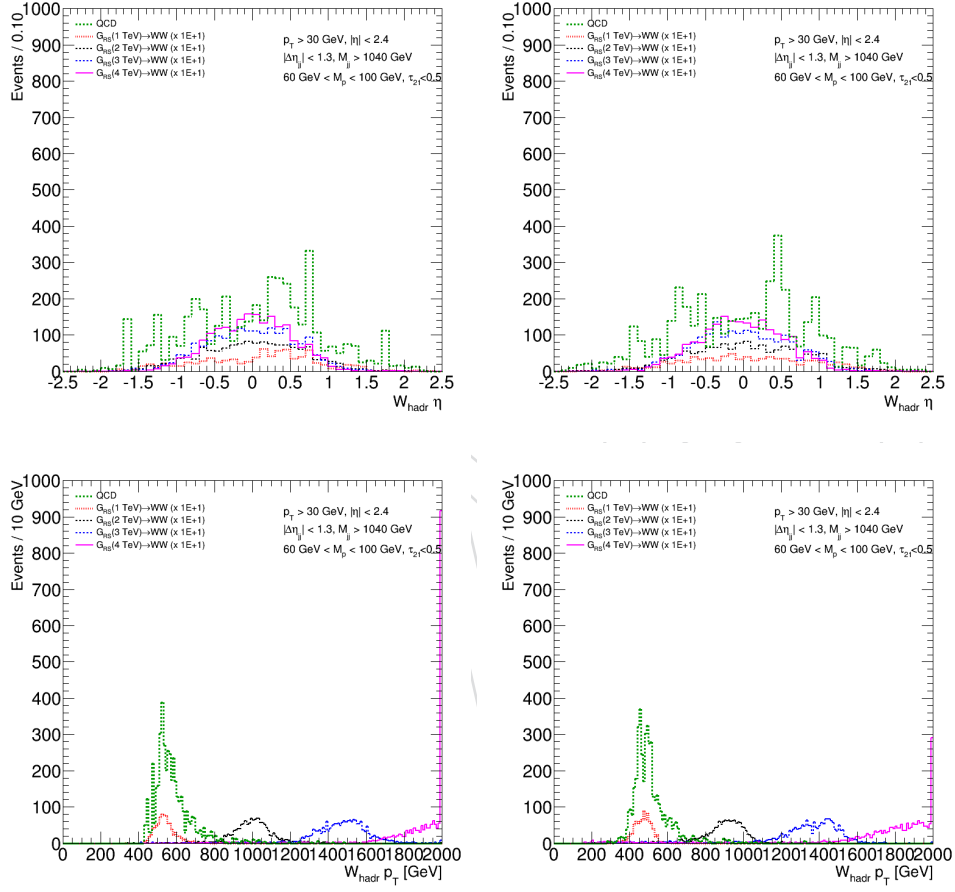


Figure 50: Control plots after full selection has been applied, here showing the jet η of the leading (top left) and second-leading (top right) jet in the event and jet p_T for the leading (bottom left) and second leading (bottom right) jet for the HP category.

871 7 Theoretical Framework

872 7.1 Theory Context Overview

873 There is strong theoretical support for diboson resonance searches. From the theory point of
 874 view the diboson channels are intrinsically related; in the SM the couplings of the W and Z
 875 bosons with fermions are related by the gauge group, while its masses and couplings to Higgs
 876 bosons are fixed by the Higgs mechanism. On the other hand, for a new heavy resonance X
 877 the relation among its couplings to W, Z and Higgs is completely fixed within a class of BSM
 878 models. A first classification to understand the possible BSM frameworks is the spin hypothesis
 879 for the resonance. We briefly discuss the motivations for all hypotheses among: neutral spin-0
 880 resonances, neutral spin-2 resonances and charged and neutral spin-1 resonances.

881 Spin-0 resonances can arise from either an extended Higgs sector or from scalar spacetime
 882 fluctuations (radion). We ignore the hypothesis of a spin-0 resonance as a heavy Higgs boson
 883 for the moment, since an extended Higgs sector where a light neutral Higgs boson has mass
 884 around 125 GeV and the other neutral particle is at the TeV scale would require a considerable
 885 amount of model fine tuning.

886 Spin-2 massive resonances can be generically motivated in strongly coupled and/or extra-
 887 dimensional models. The Warped Extra Dimensions class of models offers a complete frame-
 888 work where the properties of both spin-2 and spin-0 particles can be studied. Particularly, for
 889 the spin-2 particles we can have two different coupling limits to massless gauge bosons (and
 890 transverse modes of massive gauge bosons), the aforementioned “RS graviton” scenario and
 891 the “bulk graviton” scenario.

892 Spin-1 resonances can be motivated in both strongly or weakly coupled theories. Its couplings
 893 to the spin-1 SM bosons need to respect at least the SM gauge symmetry; therefore, instead of
 894 working with explicitly with benchmarks to fix the relative coupling of the heavy BSM reso-
 895 nances to the SM bosons³ we can focus on only two scenarios:

- 896 • the heavy resonances couples to W's and Z's as a SM triplet. In this case we should
 897 expect both its neutral and charged modes to be degenerate in mass. We refer to this
 898 framework as the Heavy Vector Triplet (HVT);
- 899 • the heavy resonance couples to W's and Z's as a SM singlet. In this case only a
 900 charged or a neutral resonance at a given mass is expected.

901 Table 12 summarises the allowed channels according to each spin hypothesis. In the following
 sections we discuss each one of the benchmarks and its predictions.

Table 12: Diboson decay modes to different spin hypotheses of a heavy resonance.

spin/charge	diboson channels
0 or 2	HH, ZZ, WW
1 charged	WH, ZW
1 neutral	WW, ZH

902

903 7.2 RS Graviton at 13 TeV

904 The original Randall-Sundrum Warped Extra Dimensions model [1, 2] is not particularly suited
 905 for searches through the $G^* \rightarrow VV$ decay channel, due to the low branching fraction of those

³If we want to relate the spin-1 diboson results with purely fermionic channels explicit benchmarks need to be considered.

decay modes ($\sim 7\%$ for ZZ and $\sim 15\%$ for WW). However, the fact that the model is i) one of the simplest resonance models that allow for both WW and ZZ decays and ii) directly implemented in PYTHIA, with no need to generate LHE files, leads us to consider it for initial benchmarking and setup of the generation machinery.

In practical terms, the model is defined in terms of two parameters: the mass of the first Kaluza-Klein graviton resonance – we refer to it from now on as simply the graviton – M_G , and the ratio of the curvature parameter k over the reduced Planck mass \overline{M}_{Pl} , which we denote as $k/\overline{M}_{\text{Pl}} \equiv \tilde{k}$. The constant \tilde{k} acts as the coupling constant of the model, with the production cross-sections and widths of the graviton depending quadratically on it. Figure 51 shows the cross-section of the process $\text{pp} \rightarrow G^*$ at a center of mass energy of 8 and 13 TeV.

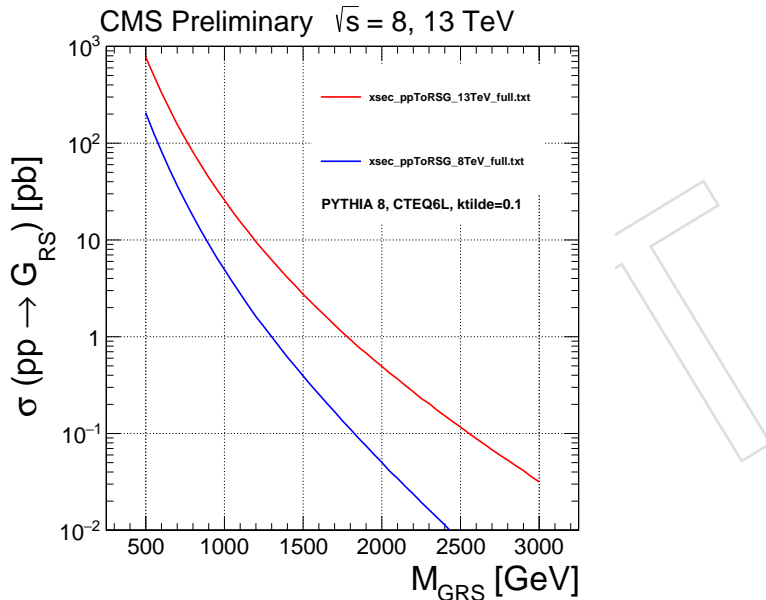


Figure 51: Cross-section of the process $\text{pp} \rightarrow G^*$ at a center of mass energy of 8 and 13 TeV, in the original RS model, for $\tilde{k} = 0.1$.

916 7.3 Bulk Graviton at 13 TeV

The bulk graviton model [3–5] is an extension of the Warped Extra Dimensions framework which proposes that the standard model fields also propagate on the extra spatial dimension (the “bulk”). Although this setup may lead to the existence of other new particles than the graviton, from the point of view of this analysis we focus solely on the $\text{pp} \rightarrow VV$ reaction. From the experimental point of view, the main differences of the bulk graviton with respect to the original RS model are:

- the much smaller production cross-section, by a factor of 10^4 .
- the much larger branching fractions to WW, ZZ and hh channels. Unlike the original RS graviton, the bulk graviton is not amenable to searches in the e^+e^- , $\mu^+\mu^-$ and $\gamma\gamma$ channels, due to its extremely low branching fractions in those channels.
- the polarization of the produced W and Z bosons. Given the $G^* \rightarrow ZZ$ process, the original RS graviton will decay to transverse polarized bosons 90% of the time, while the bulk graviton will decay to longitudinal polarized bosons more than 99% of the time (see Fig. 53–54). This leads to differences in the efficiency of the jet substructure techniques discussed earlier. Note the PYTHIA generator fails to describe correctly the distributions of angular correlations (see Fig. 55).

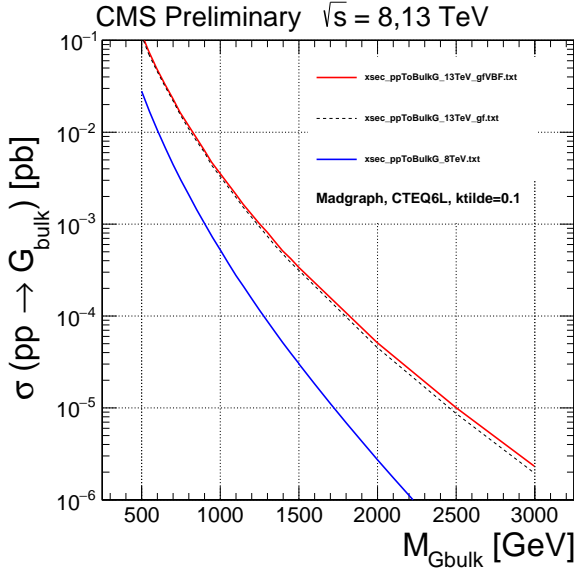


Figure 52: Cross-section of the process $\text{pp} \rightarrow G^*$ at a center of mass energy of 8 and 13 TeV, in the bulk graviton model, for $\tilde{k} = 0.1$.

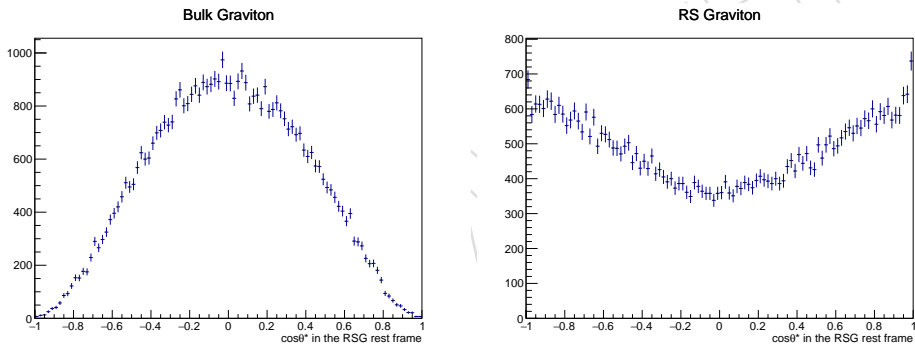


Figure 53: Comparison of the W angle in the graviton rest frame, $\cos \theta^*$, for the bulk graviton model (left) and RS graviton model (right). The sample is generated with MADGRAPH. In both cases the mass of the graviton is $M_G = 2 \text{ TeV}$ and its width is $\Gamma_G = 1 \text{ MeV}$.

933 7.4 HVT Model at 13 TeV

934 A phenomenological lagrangian describing the production and decay of spin-1 heavy
 935 resonances in the HVT hypothesis generalises a large class of explicit models predicting spin-1
 936 heavy resonances, such as heavy charged W' and neutral Z' . These type of resonances are pre-
 937 dicted by several extensions of the Standard Model such as Composite Higgs [38–40] and Little
 938 Higgs [41, 42] models or Sequential Standard Model (SSM) [43]. A convenient parameterisation
 939 of the HVT couplings based on n terms of few parameters was proposed by [6]:

- 940 • C_H : describes the interactions involving the Higgs boson or longitudinally polarized
 941 SM vector bosons
- 942 • C_f : describes the direct interactions of the new resonance with fermions
- 943 • g_V : is the typical strength of the new interaction
- 944 • M_V : mass of the new resonance

945 By scanning these parameters the generic Lagrangian describes a large class of models. The
 946 triplet field, which mixes with the SM gauge bosons, couples to the fermionic current through

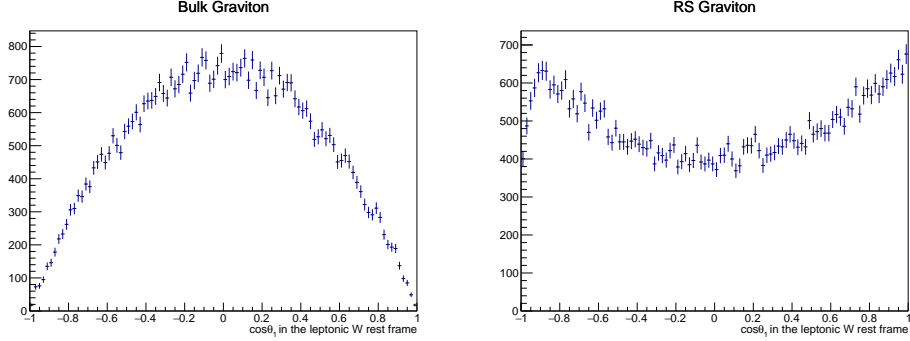


Figure 54: Comparison of the charged lepton angle in the W boson rest frame, $\cos \theta_1$, for the bulk graviton model (left) and RS graviton model (right). The sample is generated with MADGRAPH. The difference between them is due to the polarization of the W bosons: predominantly longitudinal for the former, predominantly transverse for the latter. In both cases the mass of the graviton is $M_G = 2$ TeV and its width is $\Gamma_G = 1$ MeV.

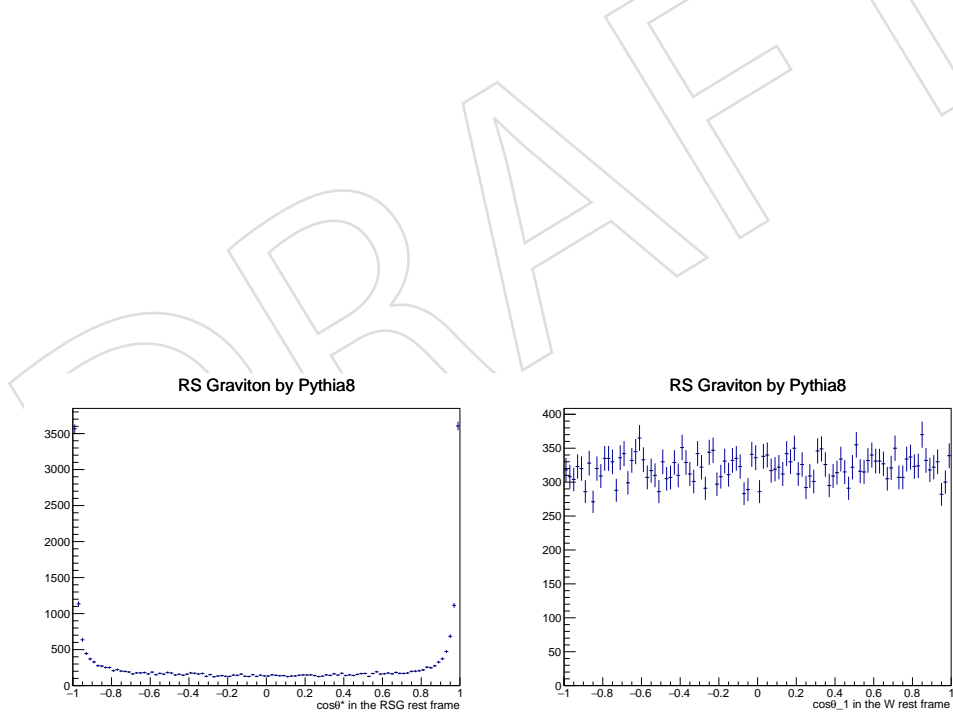


Figure 55: The W angle in the graviton rest frame (left), $\cos \theta^*$, and the charged lepton angle in the W boson rest frame (right), $\cos \theta_1$, for the RS graviton model. The sample is generated with PYTHIA. The mass of the graviton is $M_G = 2$ TeV.

the combination of parameters $g^2 C_F f / g_V$ and to the Higgs and vector bosons through $g_V C_H$, where g is the $SU(2)_L$ gauge coupling.

In particular, two benchmark models are provided in Ref.[6]. In Model A, weakly coupled vector resonances arise from an extension of the SM gauge group such as the SSM. In Model B, the heavy vector triplet is produced in a strongly coupled scenario, for example in a Composite Higgs model. In Model A, the branching fractions to fermions and gauge bosons are comparable, whereas for Model B, fermionic couplings are suppressed. Figure 56 shows the branching fractions for the two-body decays of the charged, W' , and neutral resonance, Z' , as a function of the resonance mass in Model B. As shown in the figure, the branching fractions of W' and Z' are expected to be of the same order of magnitude, since the charged and the neutral resonances are practically degenerate. Furthermore, $W' \rightarrow WH$ becomes dominant and almost degenerate with $W' \rightarrow WZ$.

Figure 57 shows the production cross sections of the neutral and charged resonances as a function of the resonance in Model B. For comparison the predicted cross sections at both the centre of mass energies of 8 TeV and 13 TeV are shown. The cross-sections for 13 TeV are computed with MADGRAPH using the model provided by the authors of Ref.[6], while the calculations at 8 TeV have been carried out using the online tools provided by the same authors and available in Ref.[44].

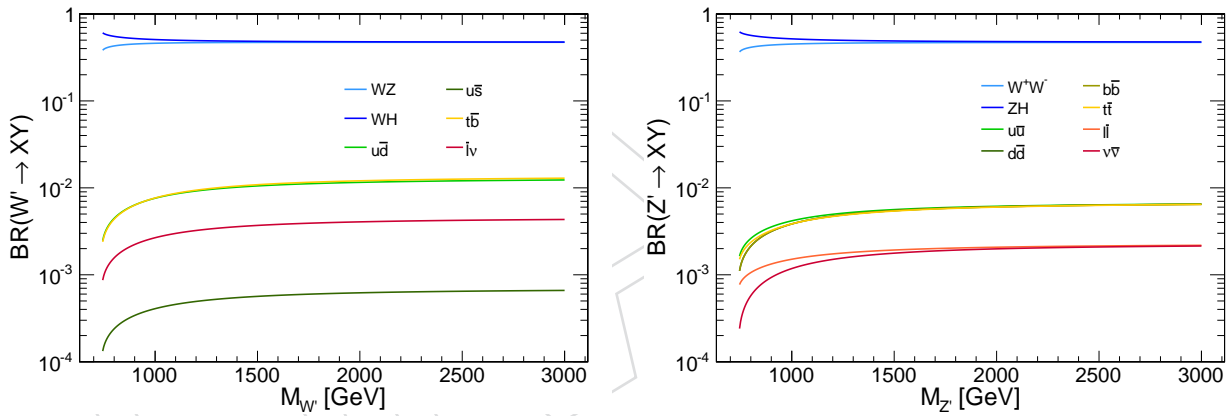


Figure 56: Branching Ratios for the two-body decays of the charged W' (left) and of the neutral resonance Z' (right) in Model B. The charged and the neutral resonances are practically degenerate.

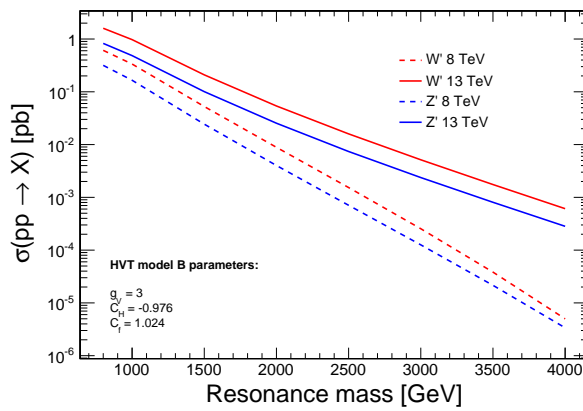


Figure 57: Production cross sections of the neutral and charged resonances as a function of the resonance mass in Model B. For comparison the predicted cross sections at both the centre of mass energies of 8 TeV and 13 TeV are shown.

965 8 Fits, Results and Strategy for Discovery

966 8.1 Background Estimation Overview

967 The gist of the analysis is the search for localised excesses (“bumps”) in the M_{VV} distribution.
 968 The M_{VV} distribution is understood to be dominated by one single process ($W+jets$ in the case
 969 of VW analysis, Drell-Yan+jets in the case of VZ analysis, QCD multijets in the case of the fully
 970 hadronic analysis), with other backgrounds amounting to subdominant contributions (usually
 971 smaller than < 10% of the total background). The *alpha method* was the background estimation
 972 method used for the Run 1 analyses in the VZ and VW channels, while the *dijet method* was
 973 used for the hadronic channel. Both methods will be used again for the respective channels,
 974 and cross-checks using the dijet method for the VW and VZ analysis are foreseen.

975 Alpha Method

First, let us consider the situation where only the dominant background is present. One considers the whole set of selections discussed previously to define a *Signal Region* (SIG), i.e., a region in the set of events which has high probability of containing signal events in case they are produced at the detector. One also defines a *Sideband Region* (SB), encompassing all the the same selections as the ones in the Signal Region except for that in a control variable; this last selection is instead inverted, such that the sets of events accepted into the Signal Region and the into the Sideband Region are non-overlapping. As is the usual case in searches for BSM physics, we do not fully trust the simulation prediction of the background M_{VV} distribution in the Signal Region by itself, due to many sources of systematic uncertainties that are hard to understand and control. The *ratio of the M_{VV} distributions* – the alpha ratio – is, however, deemed to be more trustworthy since many of those uncertainties would approximately cancel in the ratio. One can then use the simulation to estimate the alpha ratio, then multiply it by the Sideband Region M_{VV} observed in data to obtain an estimate of that background in the Signal Region. Thus, for a single background “bkg”:

$$\alpha(M_{VV}) = \frac{N_{\text{SIG}}^{\text{MC,bkg}}(M_{VV})}{N_{\text{SB}}^{\text{MC,bkg}}(M_{VV})} \quad (18)$$

and the background distribution in the Signal Region is thus estimated as

$$N_{\text{bkg}}(M_{VV}) = N_{\text{SB}}(M_{VV}) \times \alpha(M_{VV}) \quad (19)$$

976 Notice that in the above description there is no mention of the nature of the “inverted se-
 977 lection”; one would just pick a variable such that the distribution of M_{VV} in the Signal and
 978 Sideband regions are similar. In this analysis, we choose the pruned jet mass M_J as the control
 979 variable. Since the background in the Signal Region is dominated by real leptonic W/Z events
 980 + one jet which fakes the hadronic V boson, the following selection is suitable:

- 981 • **Signal Region:** events where the hadronic V candidate has M_J in a range around
 982 the mass of the V boson
- 983 • **Sideband Region:** events where the hadronic V candidate has M_J in range under
 984 the mass of the V boson

985 where the two ranges are different for the W or Z mass hypothesis. In general, the VW analysis
 986 uses a W mass hypothesis, whereas the VZ analysis uses a Z mass hypothesis, as discussed in
 987 the previous sections.

988 There are three subtleties in this approach. The first is that the background is not purely com-
 989 posed of one single process in neither the Signal nor the Sideband Region. To account for the
 990 subdominant contributions, the approach is based on the following steps:

- 991 • use only the dominant background for calculation of the alpha ratio.
- 992 • subtract the simulated subdominant contributions from the observed Sideband Re-
 993 gion. This defines a “pure dominant” Sideband Region, which is then multiplied by
 994 the alpha ratio.
- 995 • after the dominant background in the Signal Region is calculated through the alpha
 996 ratio, add back the simulated subdominant contributions in the Signal Region. The
 997 total background is then the sum of the dominant contribution (from alpha ratio)
 998 and the subdominants (directly from simulation).

The corrected equation for the background distributions is thus

$$N_{\text{bkg}}(M_{VV}) = \left(N_{\text{SB}}(M_{VV}) - N_{\text{SB}}^{\text{MC,others}}(M_{VV}) \right) \times \alpha(M_{VV}) + N_{\text{SIG}}^{\text{MC,others}}(M_{VV}) \quad (20)$$

The second subtlety is that the alpha ratio method, as described, predicts both the normalisation and the shape of the dominant M_{VV} distribution. It is generally considered better to use the data itself to constrain the normalisation. The approach is based on a fit to the sidebands of the distribution of the pruned jet mass, M_J . One uses a function of the form

$$F_{\text{ErfExp}}(x) = N_0 \cdot e^{c_1 x} \cdot \frac{1 + \text{Erf}((x - c_2)/c_3)}{2} \quad (21)$$

where N_0 , c_1 , c_2 and c_3 are free parameters determined by the fit. This functional form is chosen using the simulated M_J distribution. This function is used to fit the sidebands of the M_J distribution observed in data. The sidebands are defined as the union of M_J ranges [50, 70] GeV (lower M_J sideband) and [110, 130] GeV (upper M_J sideband). In the fit, the contributions of the subdominant backgrounds are kept fixed to the simulation predictions. The area in the signal region of the main background fitted function determines the yield N_{norm} of this source of background later used in the calculation of upper limits. A point to be taken into account is that, in view of future extensions of this search to VH final states, one should refrain to use the upper M_J sideband. Those studies are shown in Section 6.7. The final expression for the background distribution in the Signal Region is then:

$$\begin{aligned} N_{\text{SIG}}^{\text{main bkg}}(M_{VV}) &= \varkappa_{MJ} \times \left(N_{\text{SB}}(M_{VV}) - N_{\text{SB}}^{\text{MC,others}}(M_{VV}) \right) \times \alpha(M_{VV}) \\ N_{\text{bkg}}(M_{VV}) &= N_{\text{SIG}}^{\text{main bkg}}(M_{VV}) + N_{\text{SIG}}^{\text{MC,others}}(M_{VV}) \end{aligned} \quad (22)$$

999 where \varkappa_{MJ} is a normalisation factor chosen such that the integral of $N_{\text{SIG}}^{\text{main bkg}}(M_{VV})$ is equal to
 1000 the estimated yield N_{norm} .

1001 The third and final subtlety is that, for very high M_{VV} , the Sideband Region may be depleted
 1002 of events, in which case the first line of Equation 22 makes no sense. As was done in the Run 1
 1003 analyses, we choose to add the main background simulation to the total background prediction
 1004 – in this way it becomes a fully simulation-based background prediction. An inflated system-
 1005 atic uncertainty will be assigned to the background prediction when the search is performed
 1006 in this regime; the onset of this regime will be naturally defined by the highest M_{VV} event
 1007 observed in the Sideband Region data.

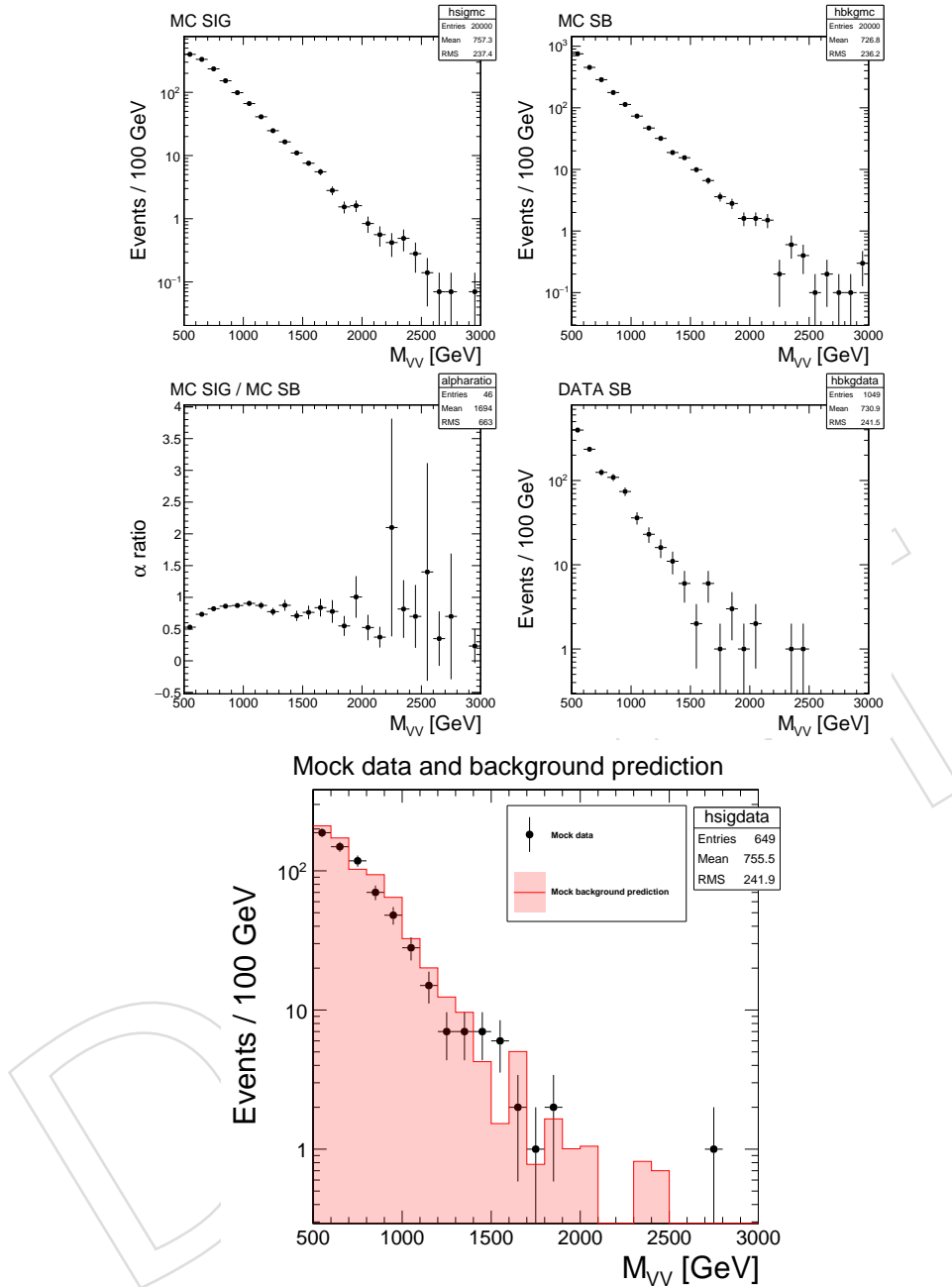


Figure 58: Demonstration of the basic workflow of the alpha method. In this workflow, predefined functions are used to randomly fill the Signal Region and Sideband Region histograms. The "mock simulation" histograms are filled with 20000 events each, and rescaled by 0.07 (for the Signal Region) and 0.1 (for the Sideband Region), representing a 7/10 expected ratio of events. The "mock data-like" histograms are filled with Poisson distributed numbers around 700 and 1000. Top left: Simulation in the Signal Region. Top right: Simulation in the Sideband Region. Middle left: alpha ratio, obtained by dividing the top left by the top right. Middle right: Data distribution in the Sideband Region. Bottom: multiplication of the alpha ratio by the data distribution in the Sideband Region, leading to the background prediction (red histogram), to be compared with the data distribution in the Signal Region (black points).

1008 **Dijet Method**

The dijet method is conceptually simpler, but it suffers from the impossibility of blinding the analysis. The method consists essentially in a smoothness test of the observed data. The background is assumed to be described by the “dijet function”, a smoothly decaying function of the form:

$$\frac{dN}{dm} = \frac{P_0(1 - m/\sqrt{s})^{P_1}}{(m/\sqrt{s})^{P_2}} \quad (23)$$

1009 where m is the dijet invariant mass, \sqrt{s} the centre of mass energy, P_0 is a normalisation pa-
 1010 rameter for the probability density function and P_1 and P_2 describe the shape. Similarly, the
 1011 signal is assumed to be described by a series of peak-like functions, depending on the signal
 1012 mass hypothesis. The hypothesis test is then comparing fits of the observed data with the
 1013 “background-only” function and “background + signal” function.

1014 **Categorization and Fitting**

1015 As was done in the Run 1 analyses, categorising the events in the Signal Region allows one
 1016 to recover signal efficiency by treating differently “high-background” and “low background
 1017 cases”. As discussed in Section 6.5, the baseline approach for Run 2 is to keep four categories:

- 1018 • two flavours of leptonic V bosons (electron and muon).
- 1019 • two purity categories of hadronic V bosons (low and high).

1020 For all analyses, the variable used for the purity categorisation is $\tau_{21} \equiv \tau_2/\tau_1$, the ratio of 2-
 1021 subjetiness to 1-subjetiness of the hadronic V candidate. The high-purity (HP) and low-purity
 1022 (LP) categories are, as mentioned previously:

- 1023 • High Purity: τ_{21} in the 0–0.5 range
- 1024 • Low Purity: τ_{21} in the 0.5–0.75 range

1025 As discussed previously, one of the possible extensions for this analysis would be to do further
 1026 categorisations. Those studies are shown in Section 6.5. All categories are non-overlapping,
 1027 which allows for their combination in the final statistical analysis.

The final background distributions are fitted independently for each category. As in Run 1, the distribution used for the fit in the VW and VZ channels is the leveled exponential, a smoothly decaying function parameterised as

$$P(M_{VV}) = \exp \left[\frac{-(M_{VV} - m_0)}{\sigma + p_0(M_{VV} - m_0)} \right] \quad (24)$$

1028 and the fit is unbinned. For the dijet function, we use the dijet function described in Eq. 23.
 1029 After the fit, the resulting functions are reparameterised in order to have the all parameters
 1030 decorrelated, through a diagonalization of the covariance matrix.

1031 The fit of the signal shapes is done separately for each channel VW, VZ and VV, and will be
 1032 treated in each of the corresponding subsections.

1033 **8.2 VZ Channel fits**

1034 For the estimation of the DY+jets background we use the alpha method, with the levelled ex-
 1035 ponential as the M_{ZZ} shape function and the F_{ErfExp} function as M_J shape. In Figure 59, we
 1036 present the fits on the jet mass distribution in the sideband for separate categories.

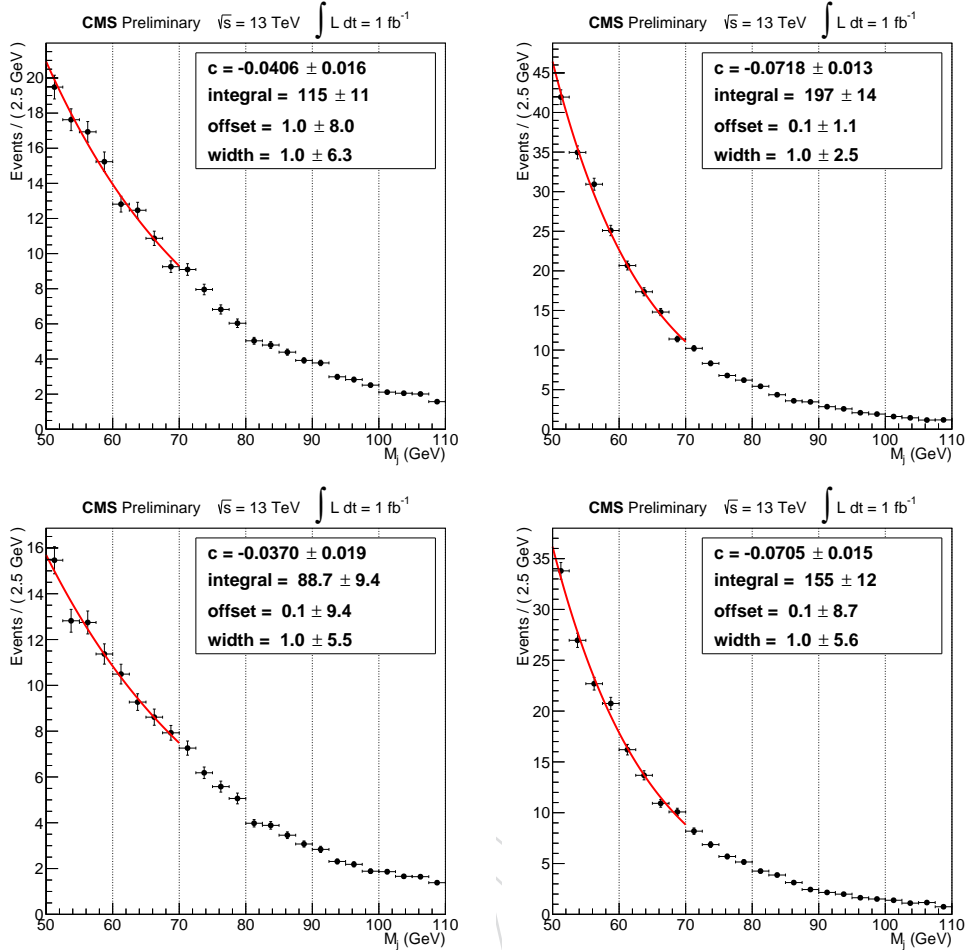


Figure 59: Fit of the jet mass (M_j) in the signal region for separate categories: electron high-purity (top-left), electron low-purity (top-right), muon high-purity (bottom-left), and muon low-purity (bottom-right). The red line corresponds to the fitting function F_{ErfExp} and the points are pseudo-data equivalent to 1fb⁻¹ of integrated luminosity.

1037 The expected number of events in the signal region is obtained by extrapolation of the fitted
 1038 M_j function beyond the sideband. In Figure 59, we can see the value of the integral in the
 1039 sideband. Since the fitting function decreases with the jet mass, the expected number of events
 1040 in the signal region is less than in the sideband.

1041 The results of the alpha method are shown in Figure 60.

1042 To model the signal peak we use the Double Crystal function, as shown in Figure 61.

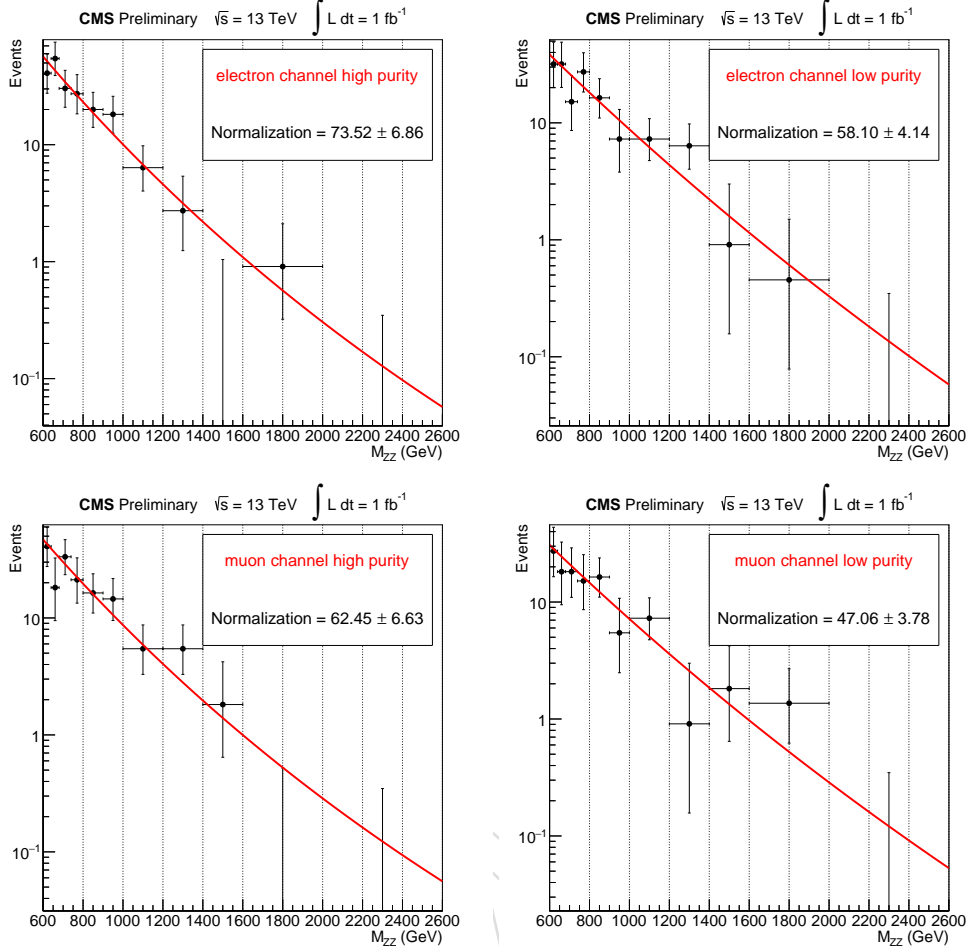


Figure 60: Determination of the $Z + \text{jets}$ background for four separate categories: electron high-purity (top-left), electron low-purity (top-right), muon high-purity (bottom-left), and muon low-purity (bottom-right). The red line corresponds to the shape obtained by the alpha method, and the dots are pseudo-data equivalent to 1 fb^{-1} of integrated luminosity.

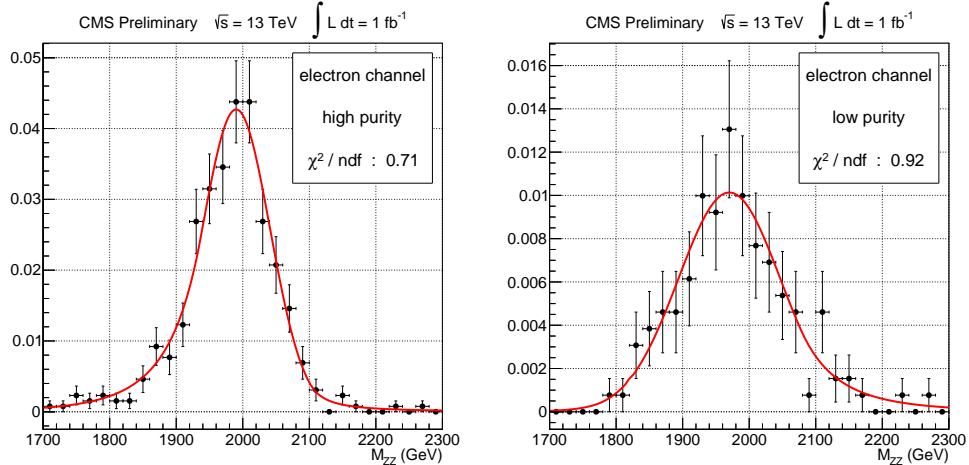


Figure 61: Fitting of the RS Graviton invariant mass. The red line corresponds to the fitted function, and the points are simulated events from the 2 TeV RS Graviton Phys14 sample.

8.3 VW Channel fits

Extraction of W+jets Normalisation

The normalisation of the W+jets in the signal region is extracted from an unbinned fit of the m_J variable, looking only at the events in the sideband region ([40-65, 105-130] GeV). The W+jets, top and VV contributions are described with functional forms determined with pre-fits on the simulated samples. The extrapolation of the W+jets normalisation to the signal region is performed through the functional model. The single top, VV and $t\bar{t}$ samples are fixed to the simulation, and their contributions will be corrected with scale factors with the arrival of data-taking. As opposed to the VZ channel, here we have a higher contribution of the different backgrounds, so we treat all of them separately, in an extension of what has been described in Section 8.1. Different empirical functions are used to fit each contribution, and they are summarised in Table 13.

$$\begin{aligned} F_{\text{ErfExp}}(x) &= e^{c_0 x} \cdot \frac{1 + \text{Erf}((x - a)/b)}{2} \\ F_{\text{ErfExp2Gaus}}(x) &= \frac{1 + \text{Erf}((x - a)/b)}{2} \cdot e^{-(x - x_0)^2 / 2\sigma^2} \\ F_{2\text{Gaus}}(x) &= c_0 \cdot G_0(x, x^0, \sigma^0) + c_1 \cdot G_1(x, x^1, \sigma^1) \\ F_{\text{ErfExp2Gaus}}(x) &= e^{c_0 x} \cdot \frac{1 + \text{Erf}((x - a)/b)}{2} \cdot (c_0 \cdot G_0(x, x^0, \sigma^0) + c_1 \cdot G_1(x, x^1, \sigma^1)) \end{aligned} \quad (25)$$

- 1045 In Figure 62, MC fits for the non-dominant background and for the W+jets are shown for the
 1046 muon channel.

Table 13: Summary of the shapes used for fit the m_J spectra of each background component.

W+jets	$t\bar{t}$	Single Top	VV
F_{ErfExp}	$F_{\text{ErfExp2Gaus}}$	$F_{\text{ErfExpGaus}}$	$F_{2\text{Gaus}}$

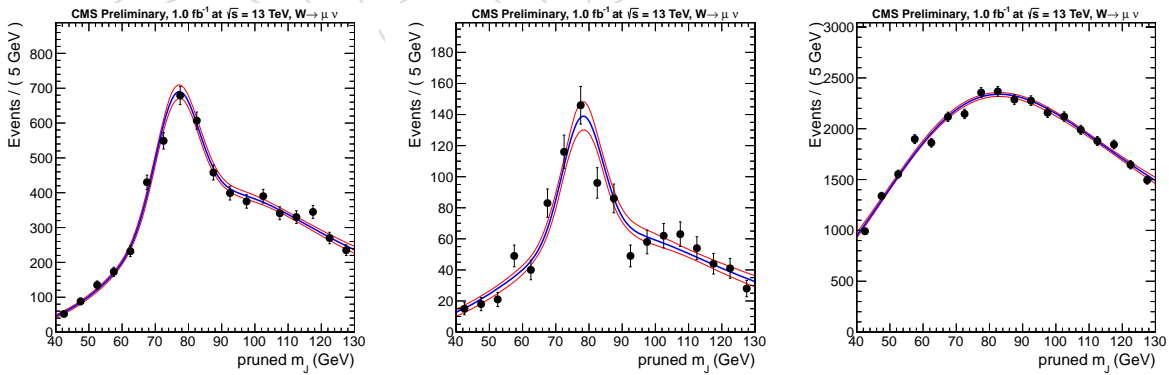


Figure 62: Simulation fits on m_J spectra, for the muon channel. From the left: $t\bar{t}$, single top, W+jets.

- 1047 The final fits in the m_J sideband to extract the W+jets normalisation are shown in Figure 63
 1048 for the muon and the electron channels. In all the plots presented, the points correspond to
 1049 pseudo-data equivalent to 1 fb^{-1} .

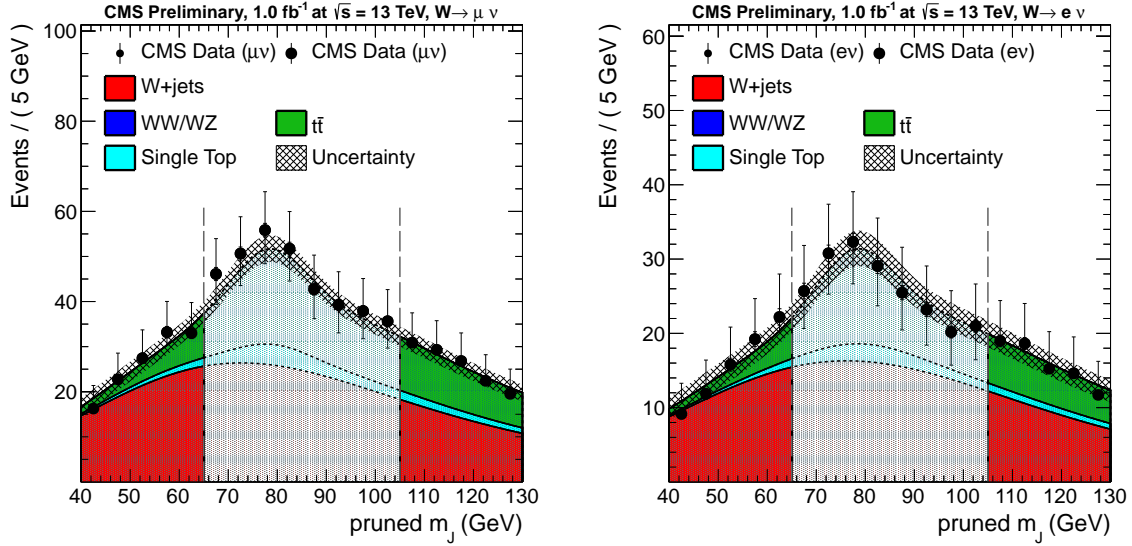


Figure 63: Examples of m_j fits to extract the W+jets normalization for the muon (left) and electron (right) channels.

1050 W+jets Shape Extraction

1051 The m_{WW} spectrum for the all backgrounds is parameterised by a levelled exponential, as de-
 1052 scribed in Section 8.1. In the sideband region, the contribution of the non-dominant back-
 1053 grounds is extracted from fit on simulation. Then, a fit on data in the Sideband Region is
 1054 performed to extract the W+jets shape, subtracting the contribution of the other backgrounds.
 1055 The sideband fits are shown in Figure 64 for the muon and the electron channel. The uncertain-
 1056 ties on the fits are also included in the plot, based on the parametric errors estimation. Again,
 1057 the points correspond to pseudo-data equivalent to 1 fb⁻¹.

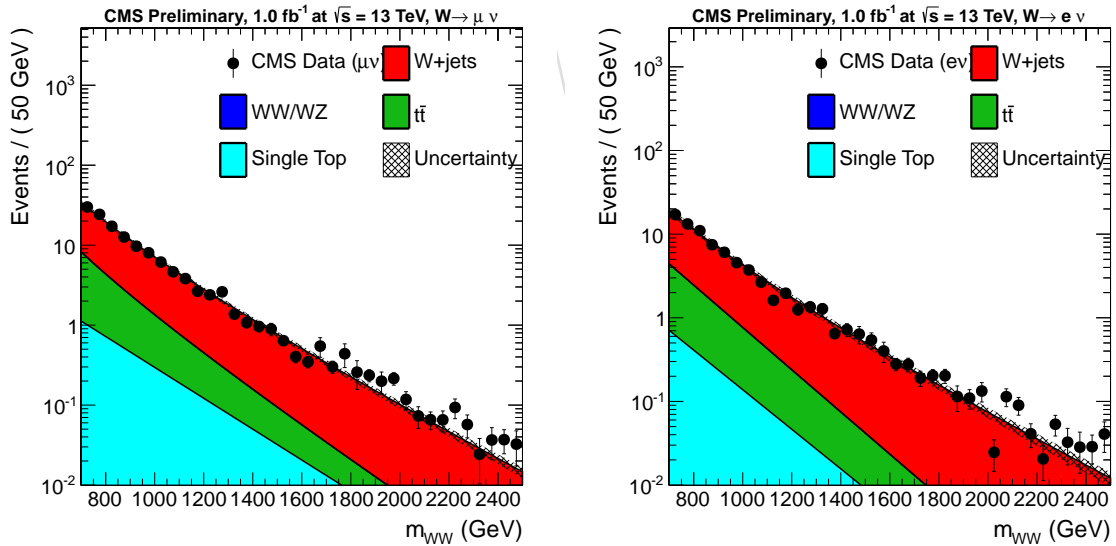


Figure 64: Examples of m_{WW} sideband fits to extract the W+jets shape for the muon (left) and electron (right) channels

1058 In order to extrapolate the W+jets shape into the Signal Region, we use the alpha method. The
 1059 α functions are shown in Figure 65.

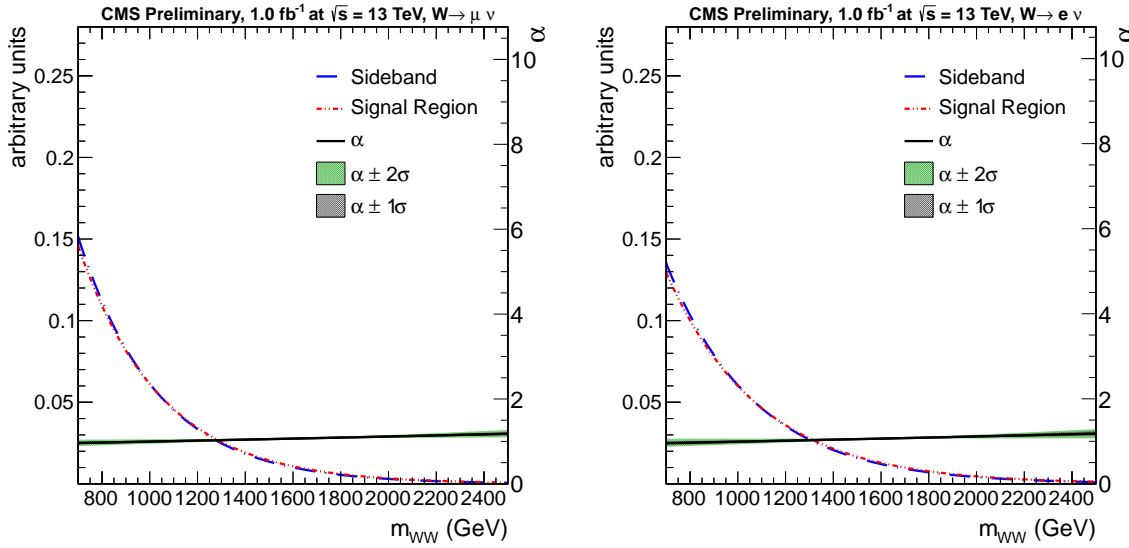


Figure 65: Examples of m_f fits for the W+jets extrapolation function α for the muon (left) and electron (right) channels.

Final Background Extraction

The contribution of the non-dominant background to the Signal Region is taken straight from the simulation, with a fit on to the $m_{\ell\nu j}$ spectrum. In Figure 66, the fits on $t\bar{t}$ and single top are shown for the muon channel.

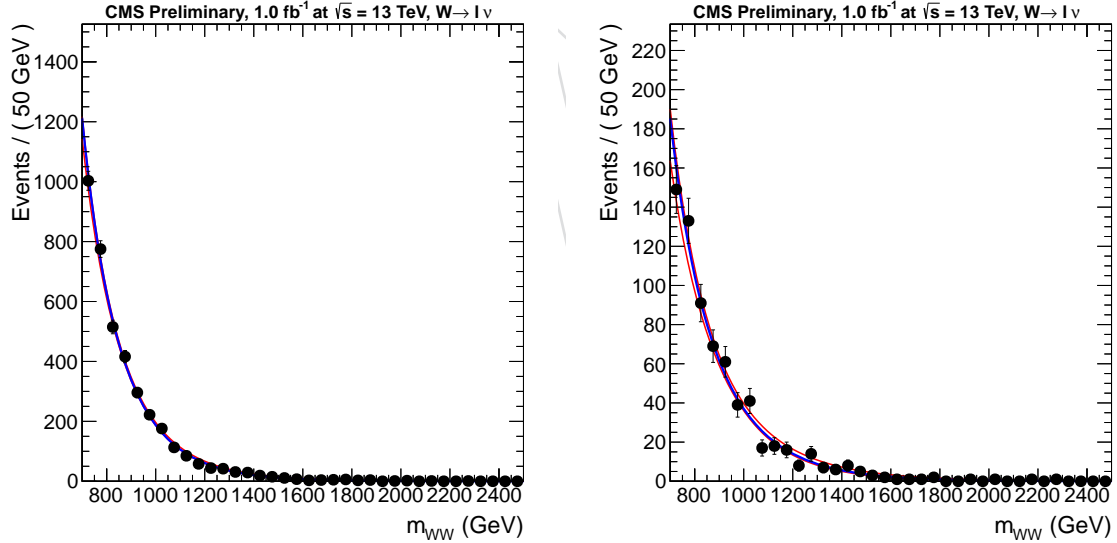


Figure 66: Simulation fits of non-dominant background $m_{\ell\nu j}$ spectra for events inside the signal region for muon channel, for $t\bar{t}$ process (left) and single top process (right).

Finally, the extrapolation of the W+jets $m_{\ell\nu j}$ shape into the Signal Region is given in Figure 67.

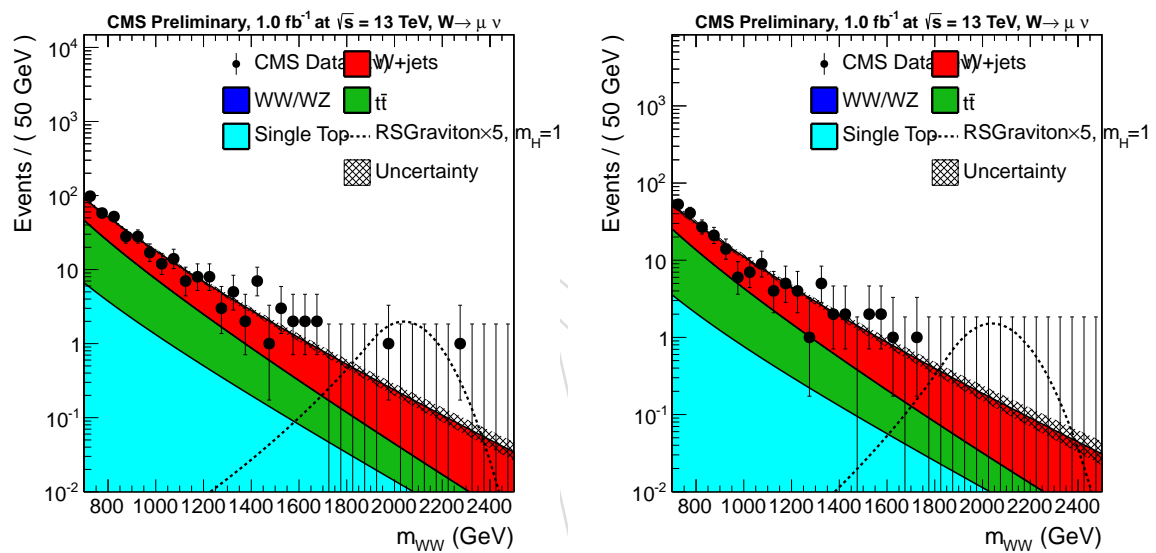


Figure 67: Examples of m_J extrapolation of the $m_{\ell\nu j}$ shape into the Signal Region for the muon (left) and electron (right) channels.

8.4 Dijet Channel fits

To model the QCD multijets background shape in the dijet invariant mass spectrum, we use the dijet function as described in Eq. 23. Figure 68 shows an example of fitting the background to 3 fb^{-1} pseudo data taken from Phys14 QCD multijet samples. Here a background only fit

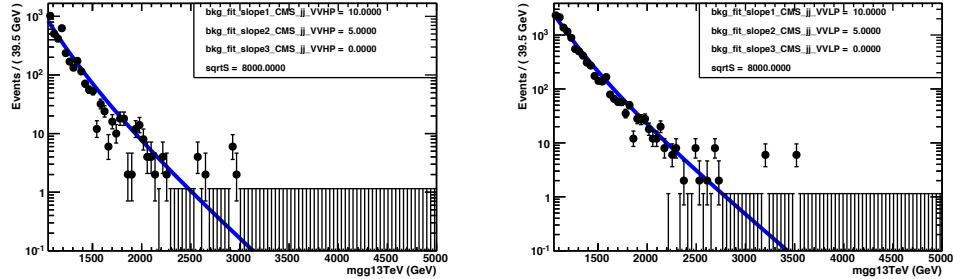


Figure 68: Background fit to mock data points using 3 fb^{-1} of 13 TeV Phys14 pseudodata.

is shown, while for the limit extraction, a signal plus background fit is performed leaving all background parameters floating. The signal shape is extracted from Phys14 signal MC in 1 TeV steps from 1 to 4 TeV and a linear interpolation provides shapes for the mass points in between. From these shapes P.D.F models are constructed as composite models with a Gaussian core due to detector resolution and an exponential tail to account for parton distribution function effects. Parametric shape uncertainties due to jet energy scale and resolution uncertainties are inserted by variations of the Gaussian peak position and width. The fitted signal shapes for an RS Graviton of 2 TeV are shown in Figure 69 in the HP (left) and LP (right) category. The signal and background components are then simultaneously fitted to the data points.

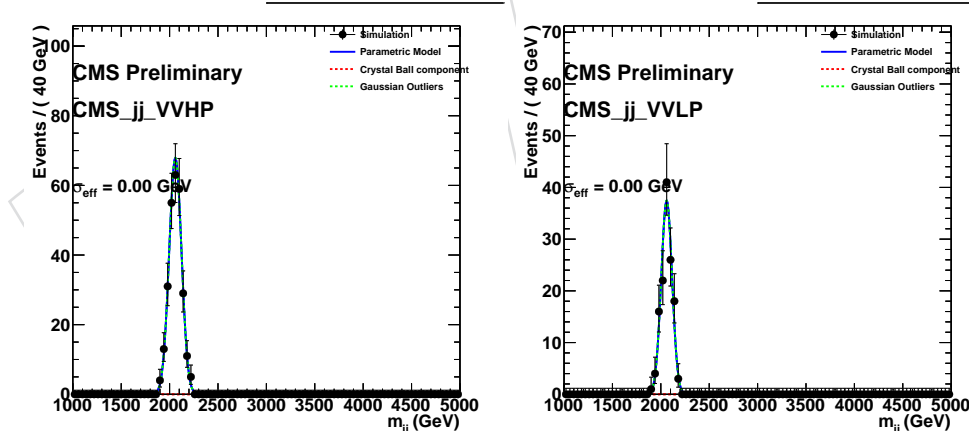


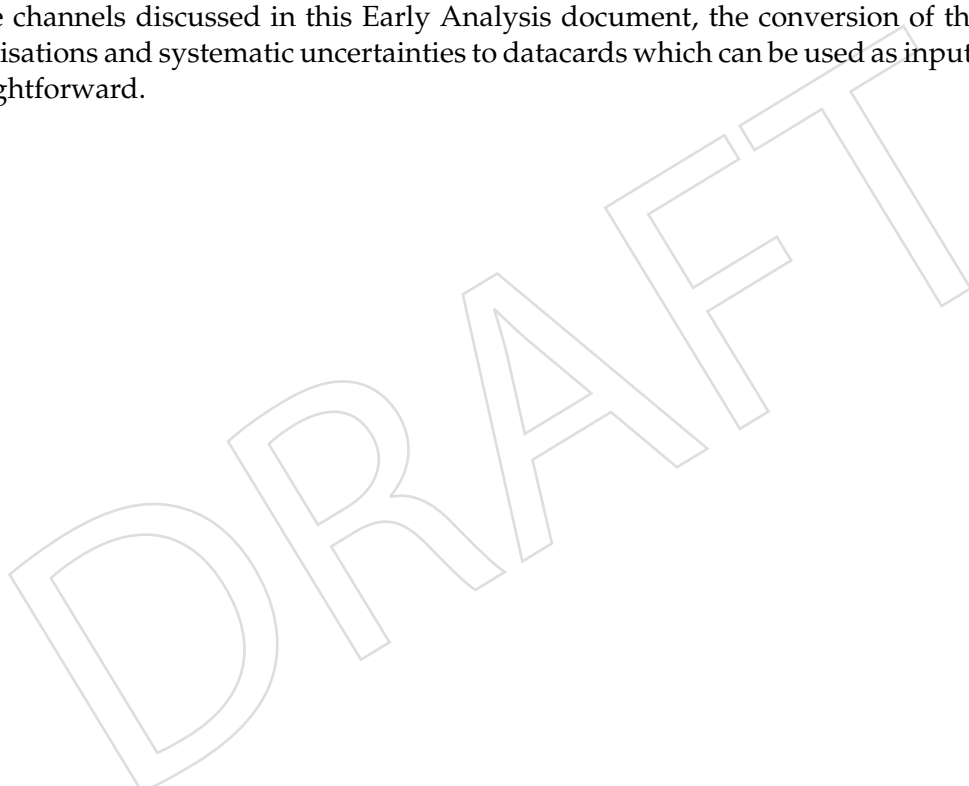
Figure 69: Fitted signal shape from Phys14 signal MC for the HP (left) and LP (right) category. Here for a 2 TeV RS Graviton.

1078 8.5 Limits**1079 Limit-setting Strategy: Overview**

1080 We use the `combine` tool [45] for all the statistical calculations in this study. The tool has been
1081 developed in the context of the Higgs searches in Run 1, and is one of the best-maintained
1082 pieces of software in CMS. Amongst its advantages we count:

- 1083 • It uses the RooFit and RooStats frameworks, which are integrated in ROOT and are
1084 fully supported in CMS.
- 1085 • It allows one to calculate expected and observed limits and significances both in the
1086 “cut-and-count” and the “shape-based” approaches.
- 1087 • It has support for treatment of systematic uncertainties in the fully frequentist ap-
1088 proach (“LHC type”) as well as hybrid frequentist-Bayesian approaches (“Tevatron
1089 type” and “LEP type”).

1090 For the background estimation methods where the final result is a properly normalised shape,
1091 like the channels discussed in this Early Analysis document, the conversion of those shapes,
1092 normalisations and systematic uncertainties to datacards which can be used as input for `combine`
1093 is straightforward.

A large, faint watermark consisting of the word "DRAFT" in a bold, sans-serif font. The letters are oriented diagonally, sloping upwards from the bottom-left towards the top-right. The watermark is rendered in a very light gray color, making it less prominent against the white background of the page content.

1094 **VZ Channel Limits**

1095 Expected limits for a RS Graviton in the mass range 1.0–4.0 TeV, with 13 TeV simulated data
 1096 for the VZ channel, are reported. The results for both a cut-and-count approach and shape
 1097 analysis are shown in Figures 70 and 71, respectively. The cut-and-count is done in the follow-
 1098 ing regions of m_{ZZ} :

- 1099 • $M_{RS} = 1$ TeV: integrate events in the 800–1200 GeV range.
- 1100 • $M_{RS} = 2$ TeV: integrate events in the 1700–2300 GeV range.
- 1101 • $M_{RS} = 3$ TeV: integrate events in the 2400–3500 GeV range.
- 1102 • $M_{RS} = 4$ TeV: integrate events in the 3200–4800 GeV range.

1103 We observed a slight improvement in the shape analysis with respect to cut & count.

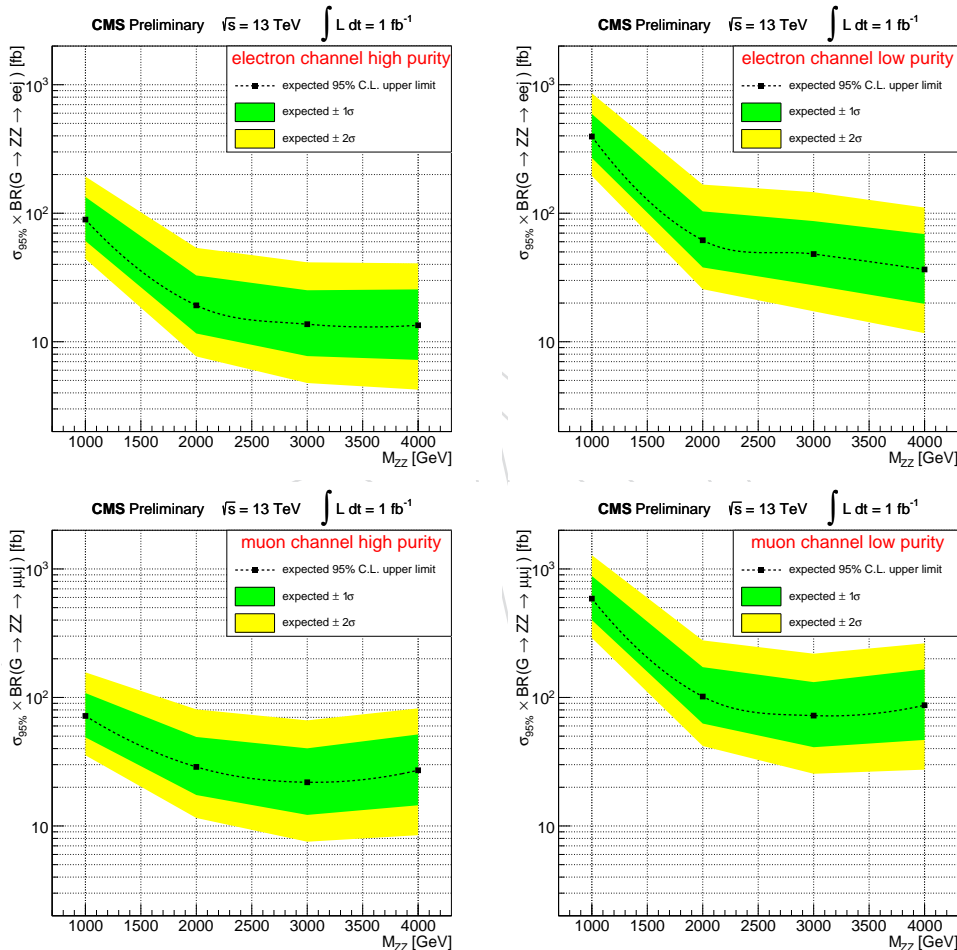


Figure 70: Expected limits obtained by cut & count in the four categories: electron high-purity (top-left), electron low-purity (top-right), muon high-purity (bottom-left), and muon low-purity (bottom-right).

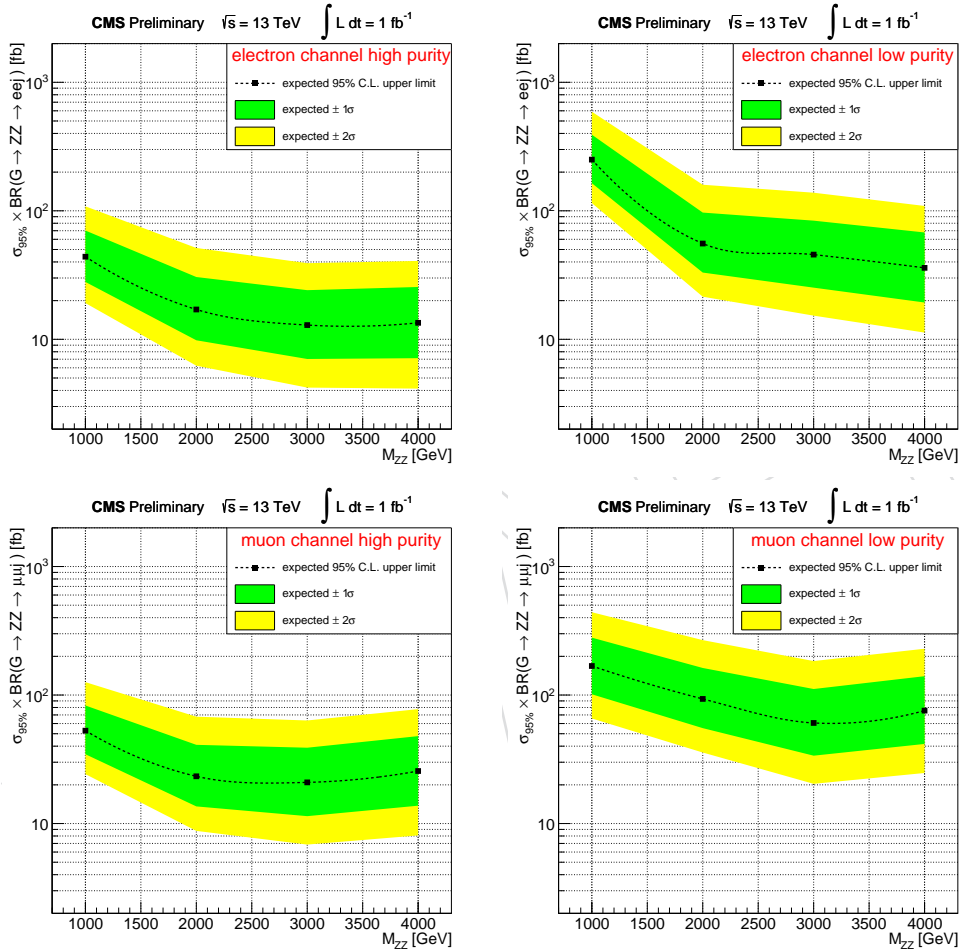


Figure 71: Expected limits obtained by shape analysis in the four categories: electron high-purity (top-left), electron low-purity (top-right), muon high-purity (bottom-left), and muon low-purity (bottom-right).

1104 **VW Channel Limits**

1105 In this section, the expected limit for a RS Graviton in the mass range 1.0–4.0 TeV, with 13
 1106 TeV simulated data for the VW channel, is reported. The limits are reported for 1 fb^{-1} of
 1107 pseudodata statistics. Figure 72 shows the expected limit for the high-purity and the low-purity
 1108 category, combining muon and electron channels. In Figure 73, the expected limit for the muon
 1109 channel and for the electron channel (combining HP+LP) is shown. Finally, the combination of
 1110 the all channels/categories is reported in fig. 74.

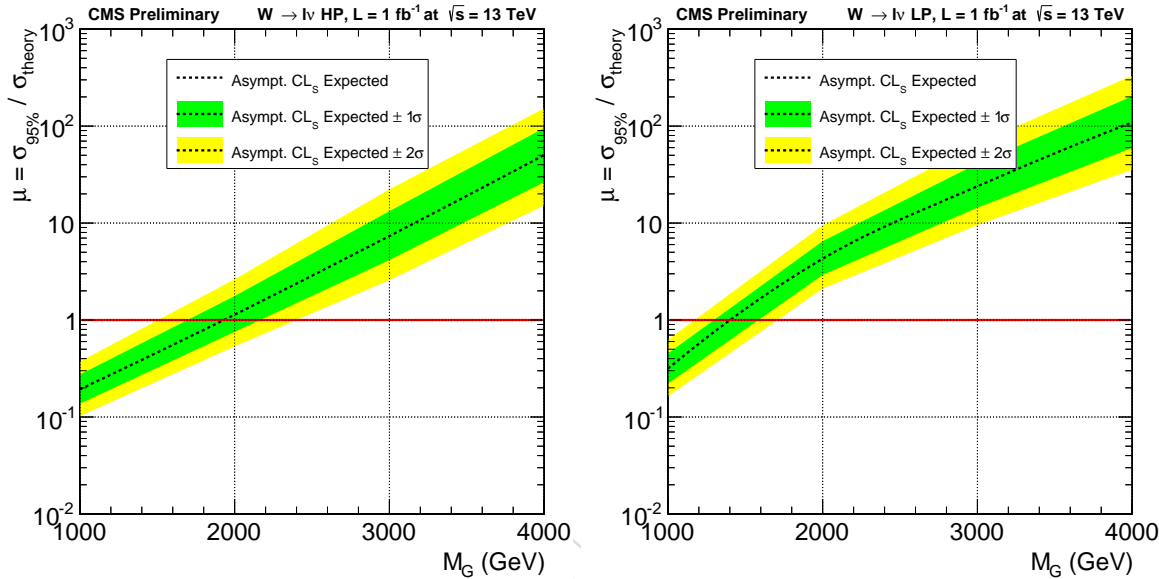


Figure 72: Expected combined limit (mu+ele) for a luminosity of 1 fb^{-1} with 13 TeV data. Left: high-purity category, right: low-purity category.

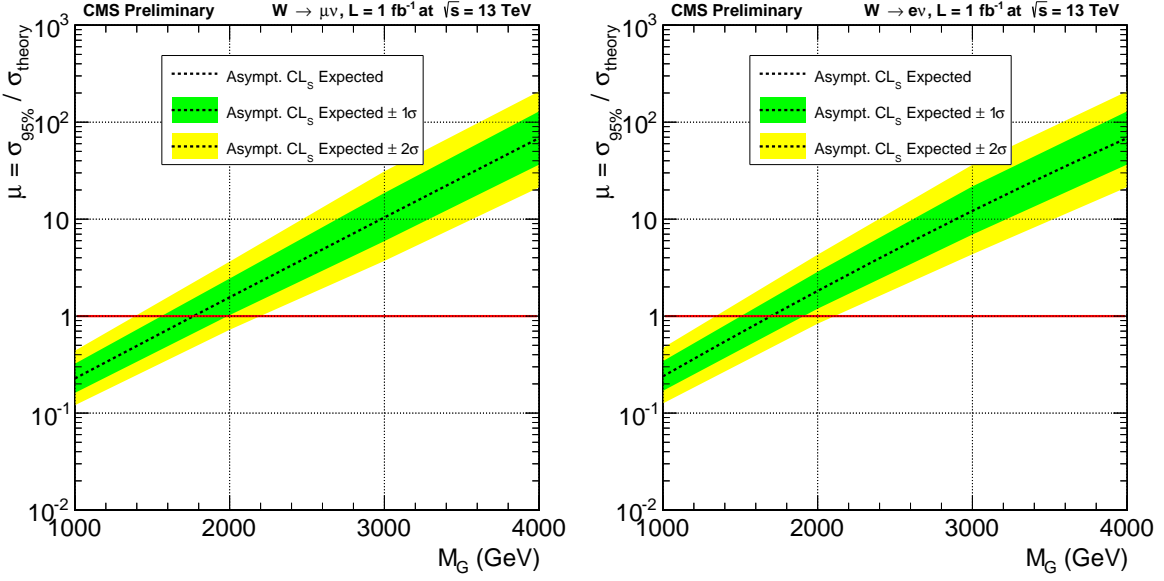


Figure 73: Expected combined limit (HP+LP) for a luminosity of 1 fb^{-1} with 13 TeV data. Left: muon channel, right: electron channel.

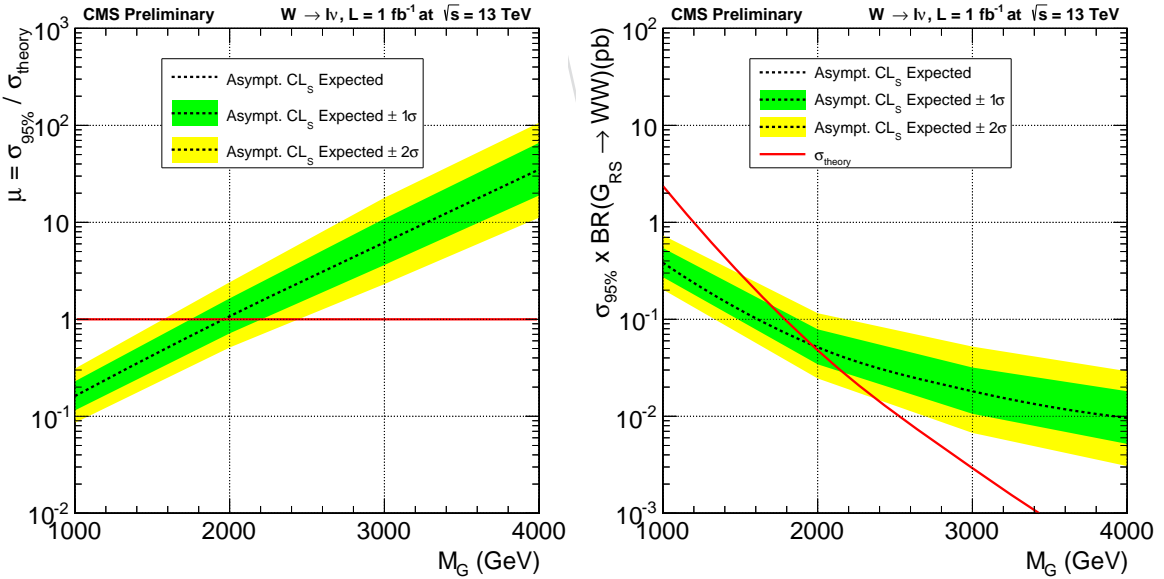


Figure 74: Combination of the all categories, for a luminosity of 1 fb^{-1} with 13 TeV data. Left: limit on the signal strength, right: limit on the cross section.

1111 Dijet Channel Limits

Limits in the cross section of the process $G^* \rightarrow WW$ in the hadronic channel are obtained using the asymptotic CL_S method. The binned likelihood is defined as

$$L = \prod_i \frac{\mu_i^{n_i} e^{-\mu_i}}{n_i!} \quad (26)$$

with

$$\mu_i = \sigma \cdot N_i(S) + N_i(B) \quad (27)$$

1112 Here σ is the signal strength scaling the expected number of signal events in the i -th dijet invariant mass bin $N_i(S)$, $N_i(B)$ is the expected number of background events in dijet invariant mass bin i and n_i is the observed number of events in the i th dijet invariant mass bin. The background per bin $N_i(B)$ is estimated from the background component of the best signal+background fit 1116 to the data points (here pseudo data from Phys14 simulation). Figures 75, 76 and 77 show the 1117 expected limits on the RS1 Graviton cross section using 1, 3 and 10 fb^{-1} of Phys14 pseudo data respectively.

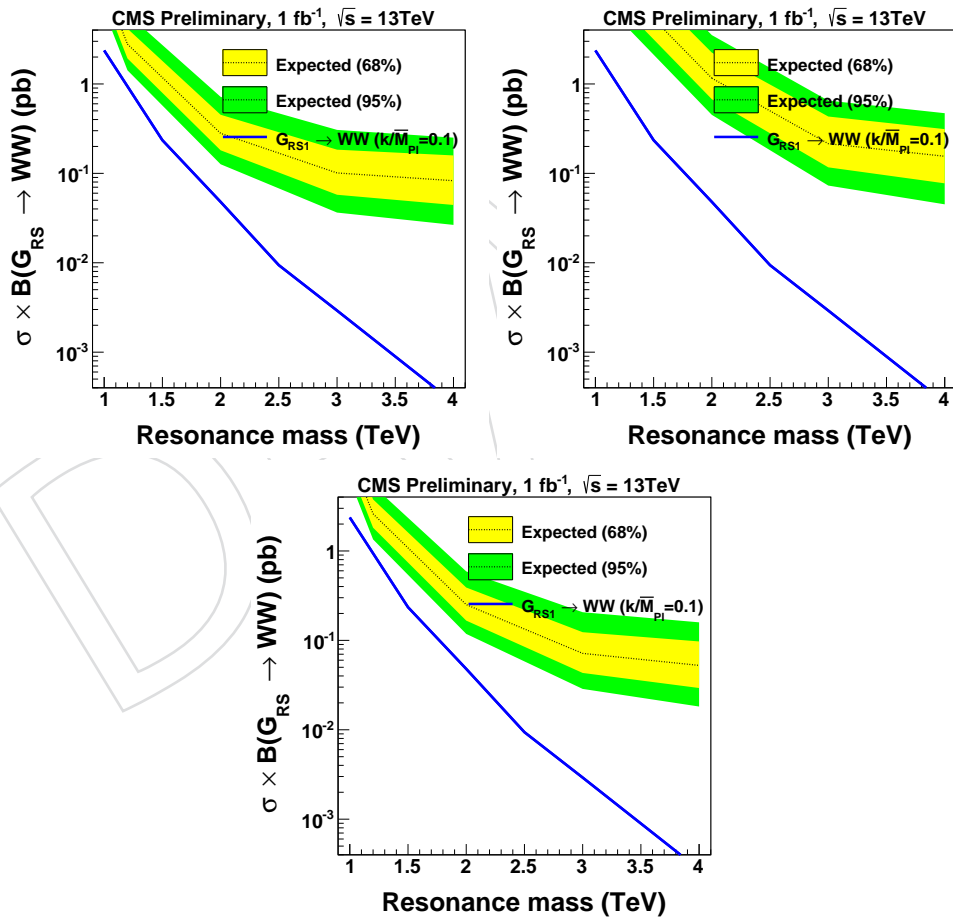


Figure 75: Expected limits for 1 fb^{-1} of Phys14 pseudo data in the dijet channel for the HP category (top left), LP category (top right) and for the combined HP+LP category (bottom).

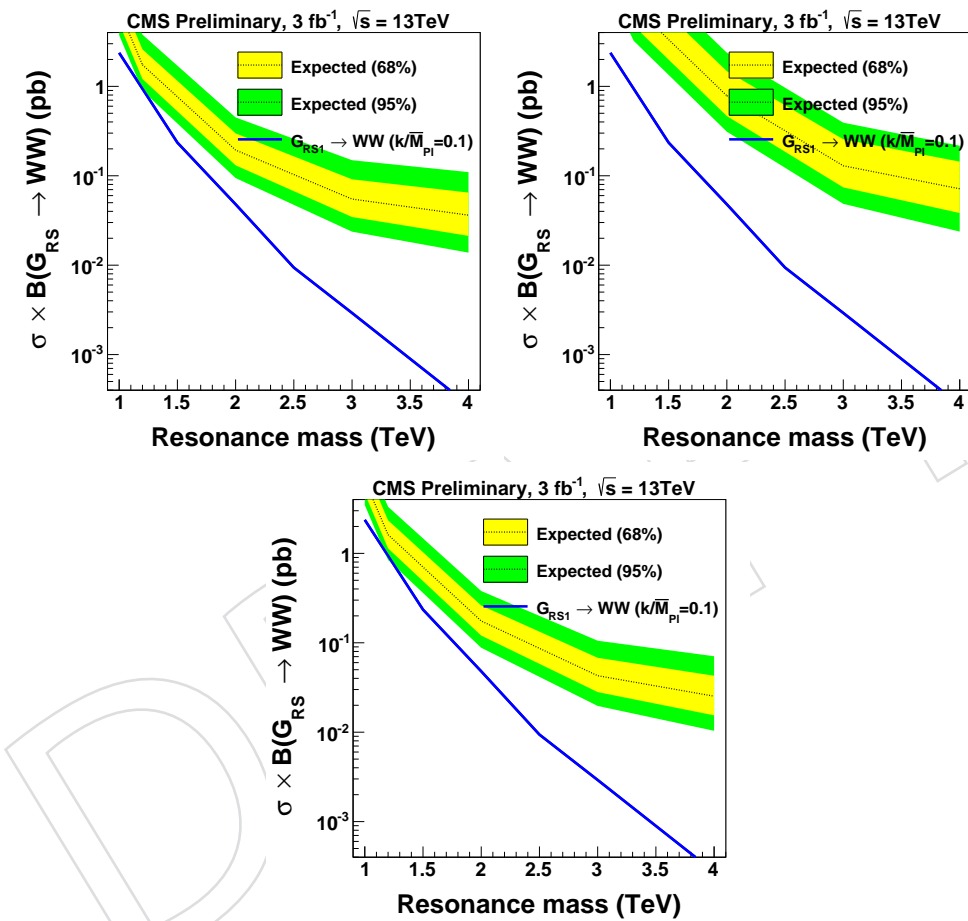


Figure 76: Expected limits for 3 fb^{-1} of Phys14 pseudo data in the dijet channel for the HP category (top left), LP category (top right) and for the combined HP+LP category (bottom).

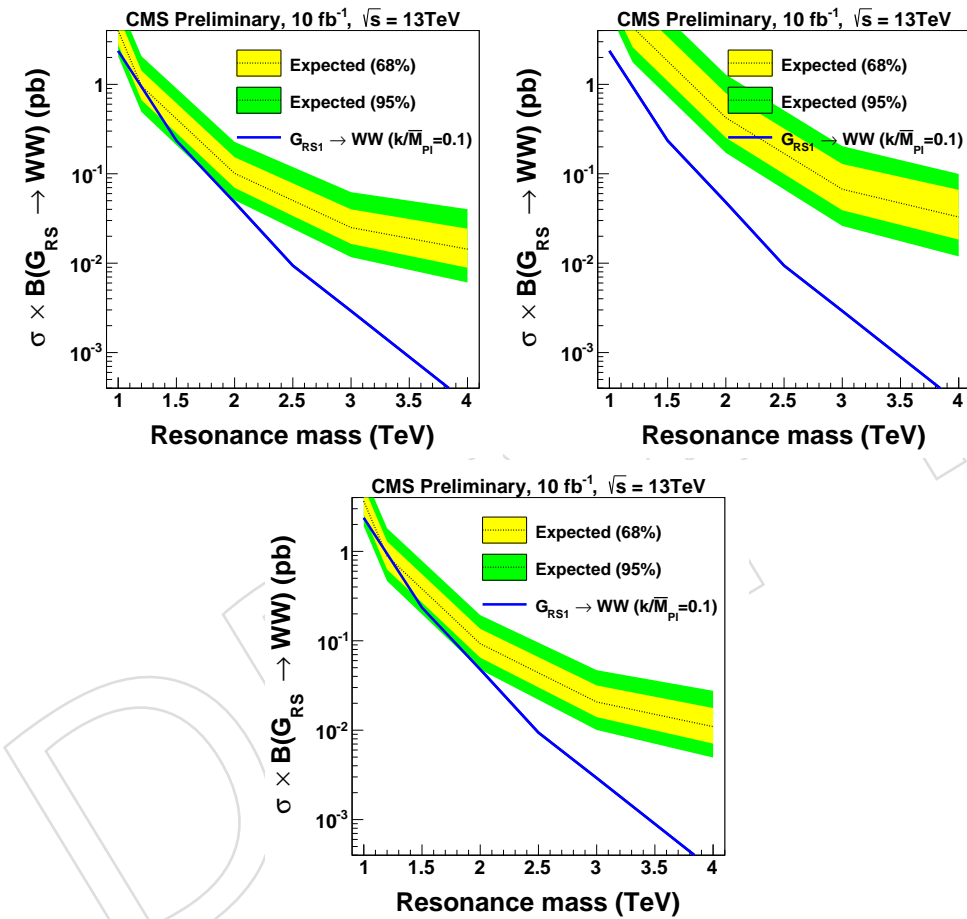


Figure 77: Expected limits for 10 fb^{-1} of Phys14 pseudo data in the dijet channel for the HP category (top left), LP category (top right) and for the combined HP+LP category (bottom).

1119 8.6 Combination of Run2 data

1120 Similarly to the Run 1 result, we plan to statistically combine the results of the $\ell\nu qq$, $\ell\ell qq$ and
 1121 dijet analyses. For Run 1, only the Bulk graviton model was considered; however, for Run 2,
 1122 we plan a combination at least in both the Bulk graviton and the HVT model. For the Bulk
 1123 graviton model, the $\ell\nu qq$ channel contributes $G \rightarrow WW$ events, the $\ell\ell qq$ channel contributes
 1124 $G \rightarrow ZZ$ events and the dijet channel contributes both $G \rightarrow WW$ and $G \rightarrow ZZ$ events. For the
 1125 HVT model, the $\ell\nu qq$ channel contributes $Z' \rightarrow WW$ and $W' \rightarrow WZ$ events, the $\ell\ell qq$ channel
 1126 contributes $W' \rightarrow ZW$ events and the dijet channel contributes both $Z' \rightarrow WW$ and $W' \rightarrow WZ$
 1127 events.

1128 Figure 78 shows a combination based on pseudo data from Phys14 simulation samples. Since
 1129 we did not have Bulk graviton samples in Phys14, we performed the combination in the context
 1130 of the RS1 graviton model instead. For comparison we also show the combination in the context
 1131 of the RS1 graviton model for the public 8 TeV analyses.

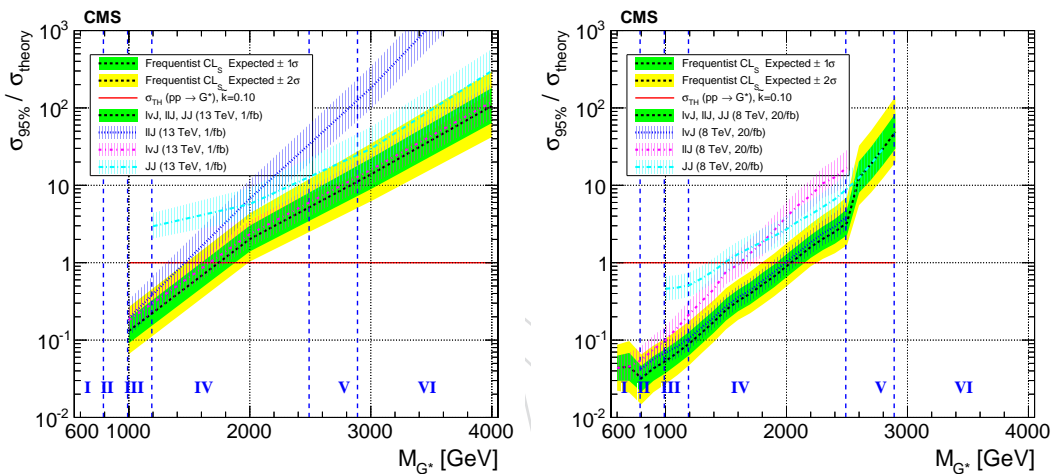


Figure 78: Combination of the $\ell\nu qq$, $\ell\ell qq$ and dijet analyses using 1 fb^{-1} of 13 TeV pseudodata (left) and 19.7 fb^{-1} 8 TeV data (right). The limit on the signal strength is shown in the context of the RS1 graviton model.

1132 8.7 Combination of Run1 and Run2 data

1133 A combination of the 8 and 13 TeV results is useful starting with the first 1 fb^{-1} of 13 TeV data.
 1134 At lower resonance masses, the 8 TeV results can stay most sensitive up to about 10 fb^{-1} , while
 1135 at high resonance masses, the 13 TeV results can be more sensitive with 1 fb^{-1} of data already.
 1136 In this section we show that the technical setup for the 8 and 13 TeV combination is ready to be
 1137 run, combining the public 8 TeV results, with 13 TeV pseudodata results. The exact numbers
 1138 should be taken with a grain of salt, because the 13 TeV pseudodata for the dijet analysis is
 1139 based on LO QCD multijet simulation samples, while the $\ell\nu qq$ analysis is based on simulated
 1140 $W+jets$ simulation samples; both samples are known to underestimate the data by order of
 1141 30%. Also, it should be noticed that in this exercise the 8 and 13 TeV uncertainties are treated
 1142 fully uncorrelated, while for the real data analysis, partial correlations e.g. between object and
 1143 theory-driven uncertainties at 8 and 13 TeV need to be evaluated.

1144 Figure 79 shows combinations of the $\ell\nu qq$, $\ell\ell qq$ and dijet analyses with 19.7 fb^{-1} of 8 TeV data
 1145 and 1 fb^{-1} of 13 TeV data in the context of the RS1 graviton model. Since we did not have Bulk
 1146 graviton samples in Phys14, we performed the combination in the context of the RS1 graviton

instead of the Bulk graviton. A combination, with 3 fb^{-1} and 10 fb^{-1} of 13 TeV data are shown in Figures 80 and 81.

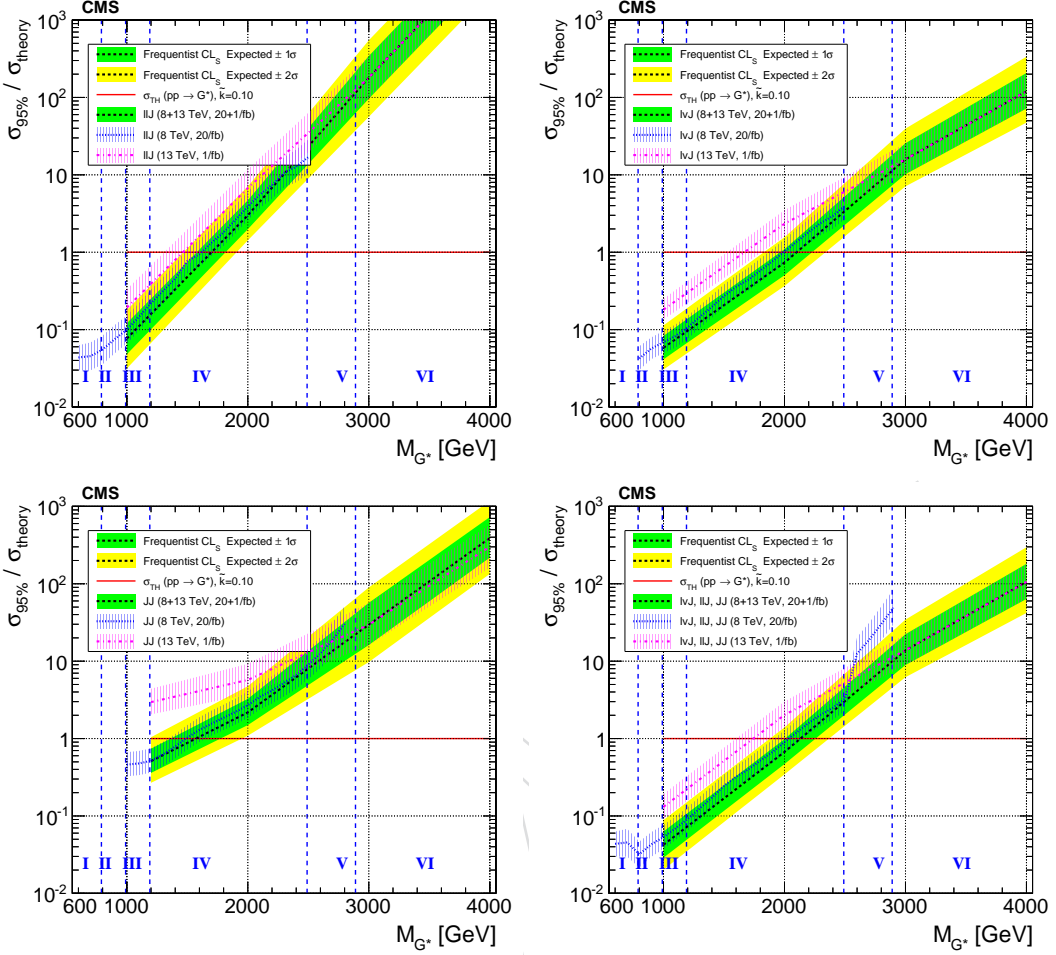


Figure 79: (top-left) Combination of the llqq analyses using 19.7 fb^{-1} of 8 TeV data and 1 fb^{-1} of 13 TeV pseudodata. (top-right) Combination of the lvqq analyses using 19.7 fb^{-1} of 8 TeV data and 1 fb^{-1} of 13 TeV pseudodata. (bottom-left) Combination of the dijet analyses using 19.7 fb^{-1} of 8 TeV data and 1 fb^{-1} of 13 TeV pseudodata. (bottom-right) Combination of the lvqq, llqq and dijet analyses using 19.7 fb^{-1} of 8 TeV data and 1 fb^{-1} of 13 TeV pseudodata. The limit on the signal strength is shown in the context of the RS1 graviton model.

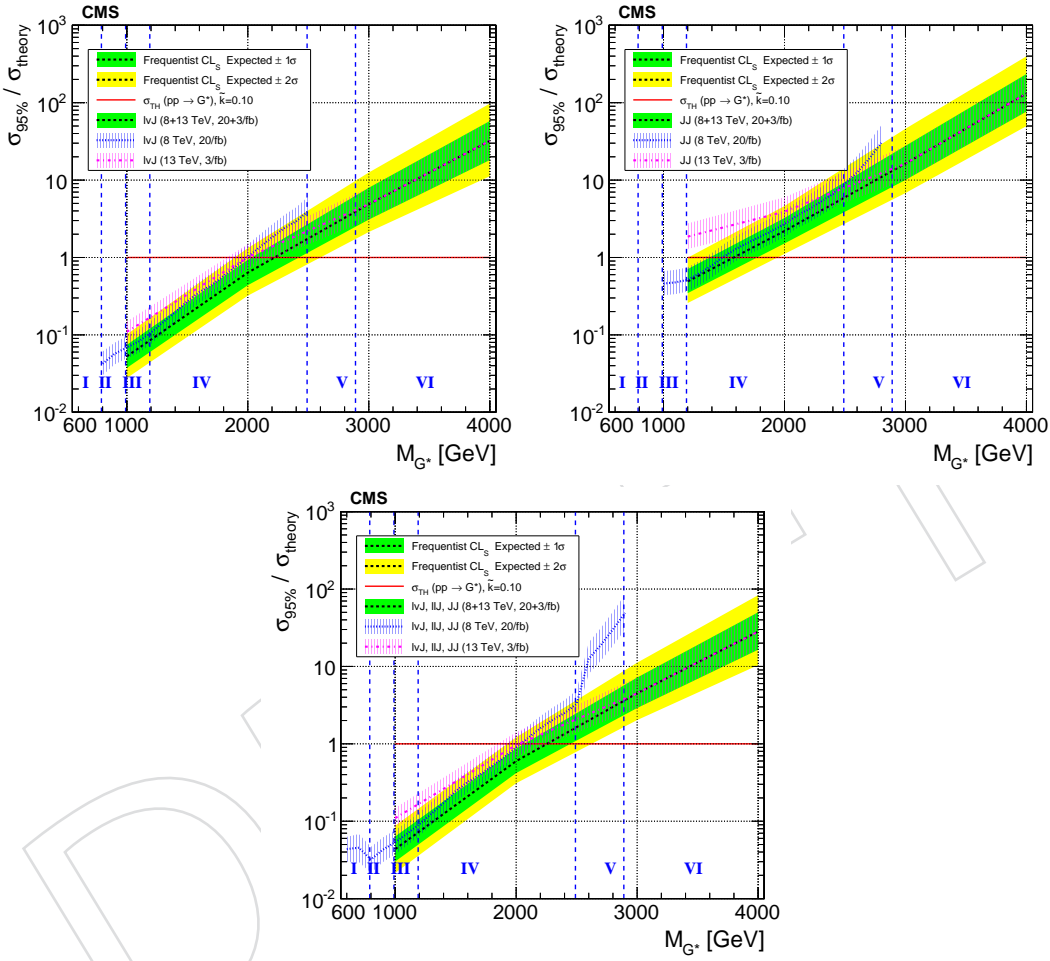


Figure 80: (top-left) Combination of the lvqq analyses using 19.7 fb^{-1} of 8 TeV data and 3 fb^{-1} of 13 TeV pseudodata. (top-right) Combination of the dijet analyses using 19.7 fb^{-1} of 8 TeV data and 3 fb^{-1} of 13 TeV pseudodata. (bottom) Combination of the lvqq, llqq and dijet analyses using 19.7 fb^{-1} of 8 TeV data and 3 fb^{-1} of 13 TeV pseudodata. The limit on the signal strength is shown in the context of the RS1 graviton model.

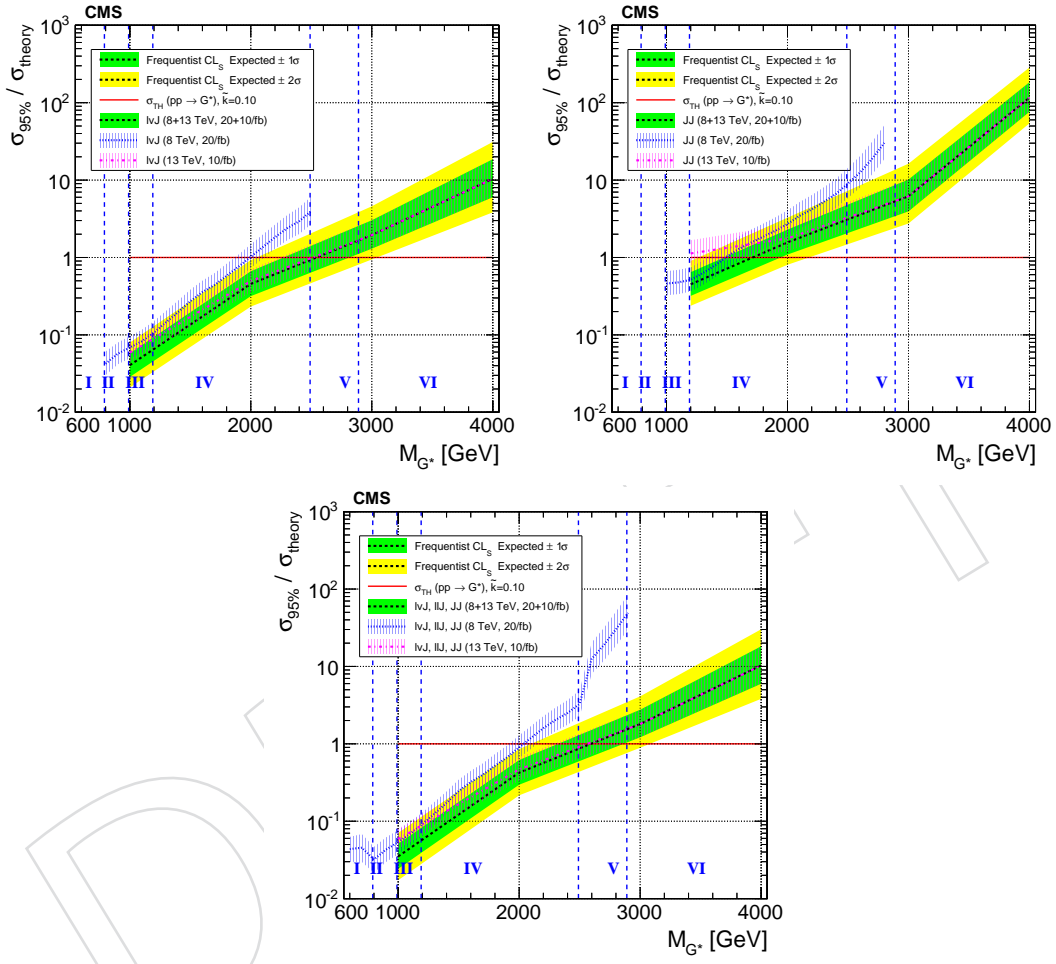


Figure 81: (top-left) Combination of the $l\nu qq$ analyses using 19.7 fb^{-1} of 8 TeV data and 10 fb^{-1} of 13 TeV pseudodata. (top-right) Combination of the dijet analyses using 19.7 fb^{-1} of 8 TeV data and 10 fb^{-1} of 13 TeV pseudodata. (bottom) Combination of the $l\nu qq$, $llqq$ and dijet analyses using 19.7 fb^{-1} of 8 TeV data and 10 fb^{-1} of 13 TeV pseudodata. The limit on the signal strength is shown in the context of the RS1 graviton model.

1149 **8.8 Strategy for Discovery**

1150 The Run 1 analyses uncovered a small excess around the region of 1.8TeV in all three channels,
 1151 as seen in Figure 82. The excess is relatively consistent amongst the three analyses, and it is
 1152 the primary allure of the repetition of this study with the Run 2 data. In this section we will
 1153 detail a possible strategy for discovery, assuming the emergence of a similar excess in the VW
 1154 channel as a “smoking gun” of the excess, and accessing the combined significance of all three
 channels.

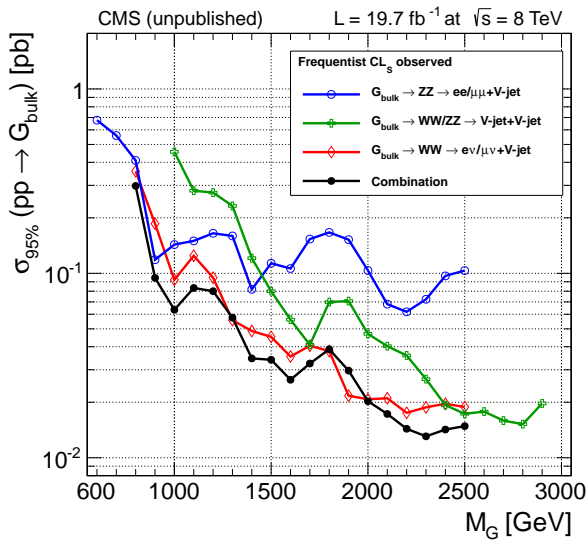


Figure 82: Observed limits for the three channels in the Run 1 analyses, interpreted in the context of the bulk graviton model. VZ channel in blue, VV channel in green and VW channel in red. All three channels show the excess in the region around 1.8 TeV.

1155

1156 **Mock evidence: VW channel**

1157 Assuming the excess at 1.8TeV is really driven by the presence of a signal, we can look at
 1158 the expected significance for such signal with 13 TeV data. For the purposes of this test, we
 1159 are going to use the 2 TeV RS Graviton sample as a surrogate for the purported signal. The
 1160 observed limit with 8 TeV data tells that this kind of signal must have a cross section larger
 1161 than 6 fb, at M_G = 2 TeV. From PDF considerations, and assuming that the production of the
 1162 signal is dominated by gluon fusion, this means this signal must have a cross section of ~ 60fb
 1163 at 13 TeV. Taking a signal with these properties, we can look at the expected significance with
 1164 13 TeV data. In Figure 83, the expected p-values are shown for 1 fb⁻¹, 3 fb⁻¹ and 5 fb⁻¹, for
 1165 the VW channel only. For a signal with M_G = 2 TeV, the plots show an expected significance
 1166 of 2.57, 4.47 and 5.76, respectively.

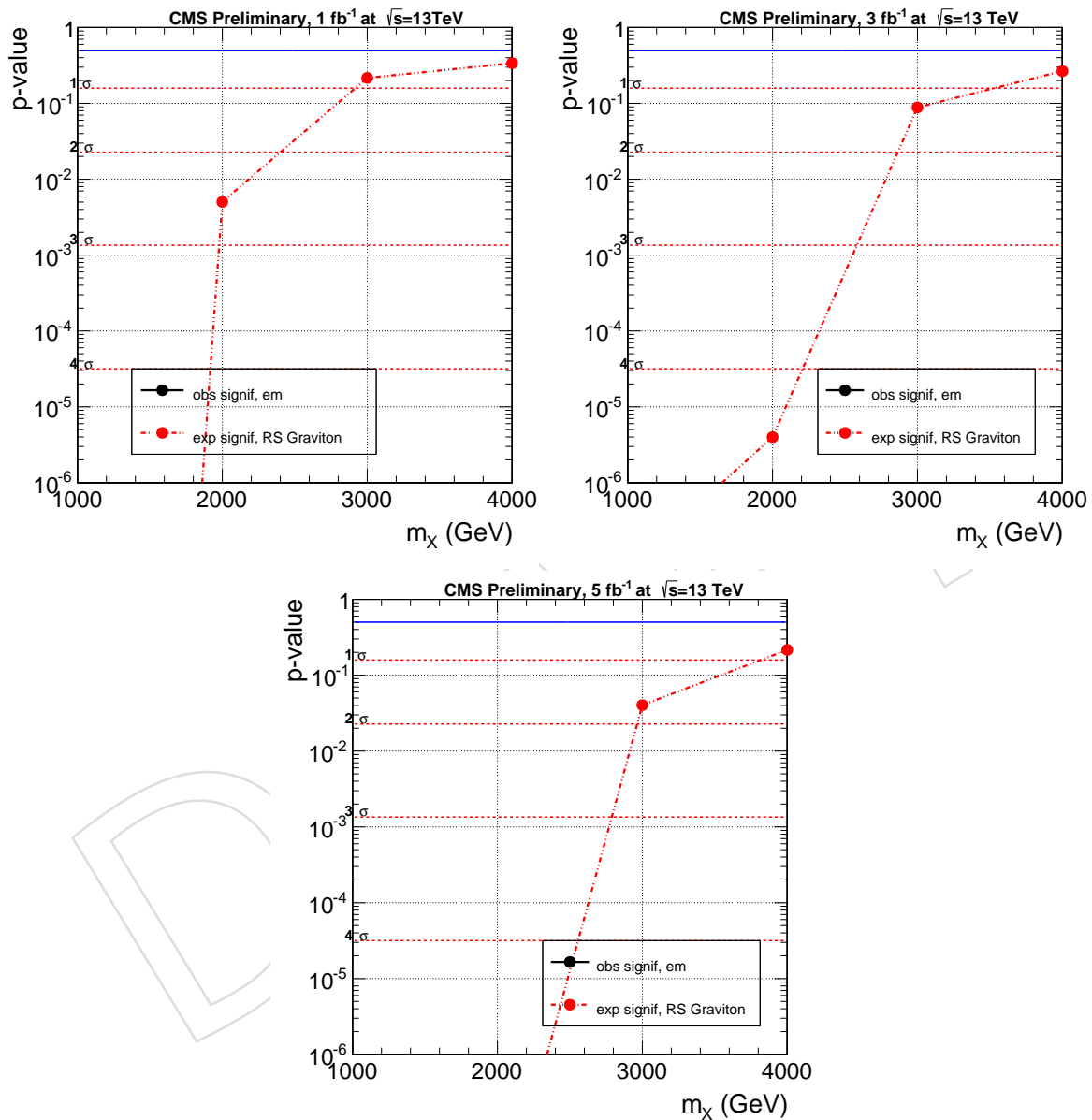


Figure 83: Expected p-value for a luminosity of 1 fb^{-1} (top left), 3 fb^{-1} (top right), and 5 fb^{-1} (bottom), with 13 TeV data.

1167 Accessing significance: combining VW, VZ and VV channels

1168 Assuming the scenario from the previous section is confirmed, the next step is to combine
1169 the channels to check if the excess is compatible amongst all three. Figure 84 shows combined
1170 expected significance of the $\ell\nu qq$, ℓqq and dijet analyses with 19.7 fb^{-1} of 8 TeV data and 1 fb^{-1}
1171 of 13 TeV data in the context of the RS1 graviton model. A similar combination with 3 fb^{-1} and
1172 10 fb^{-1} of 13 TeV data are shown in Figures 85 and 86.

1173 The RS1 graviton happens to predict an expected significance of about 2-2.5 sigma for the 8 TeV
1174 data at 2 TeV resonance mass, so we can use this model to see what happens with a 2-2.5 sigma
1175 excess, if we combine it with 13 TeV data. With 1 fb^{-1} of 13 TeV data, the significance of such
1176 an excess at 2 TeV can be increased from 2.2 to 2.8 sigma with the $\ell\nu qq$ channel, while the dijet
1177 analysis does not significantly contribute at 2 TeV with that integrated luminosity. With $10/\text{fb}$
1178 of 13 TeV, the significance of such an excess at 2 TeV can be increased from 2.2 to 3.9 sigma with
1179 the $\ell\nu qq$ channel.



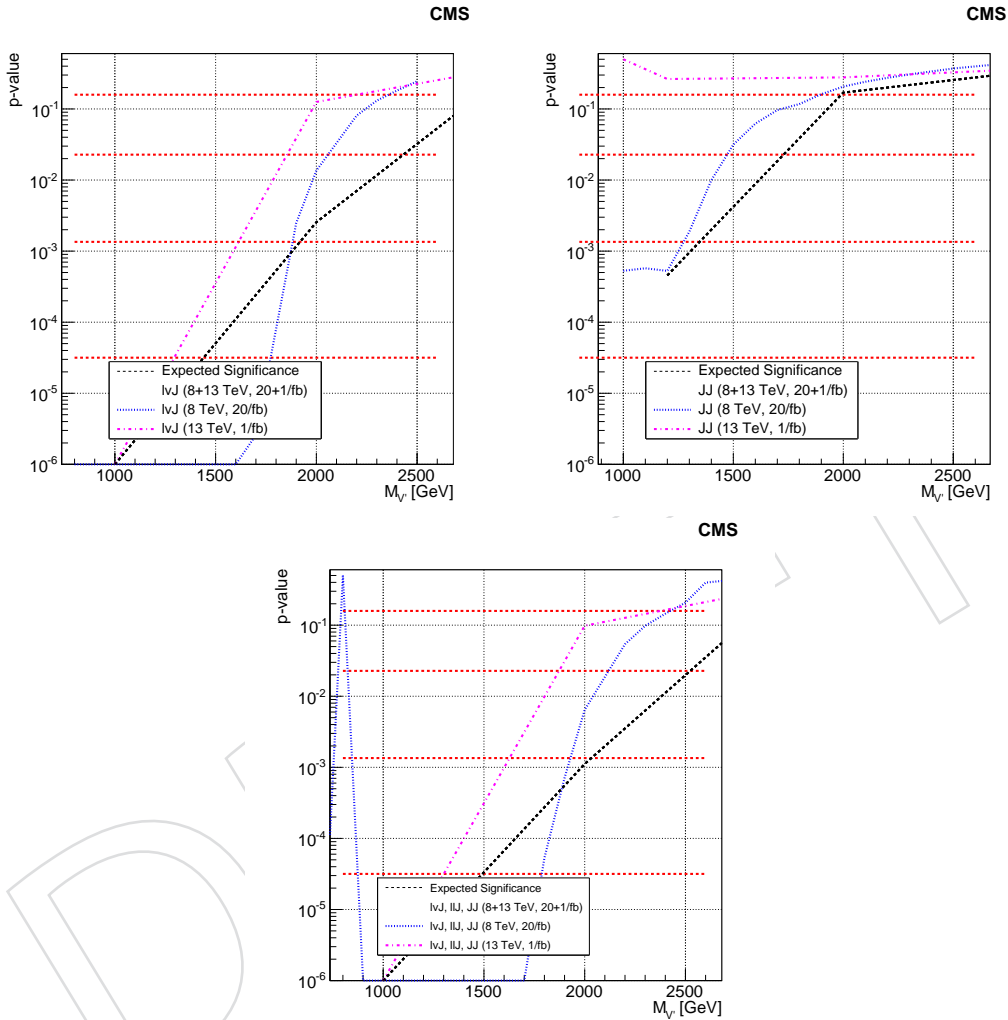


Figure 84: (top-left) Combined expected significance of the $l\nu qq$ analyses using 19.7/fb of 8 TeV data and 1/fb of 13 TeV pseudodata. (top-right) Combined expected significance of the dijet analyses using 19.7/fb of 8 TeV data and 1/fb of 13 TeV pseudodata. (bottom) Combined expected significance of the $l\nu qq$, $llqq$ and dijet analyses using 19.7/fb of 8 TeV data and 1/fb of 13 TeV pseudodata. The expected significance is shown in the context of the RS1 graviton model.

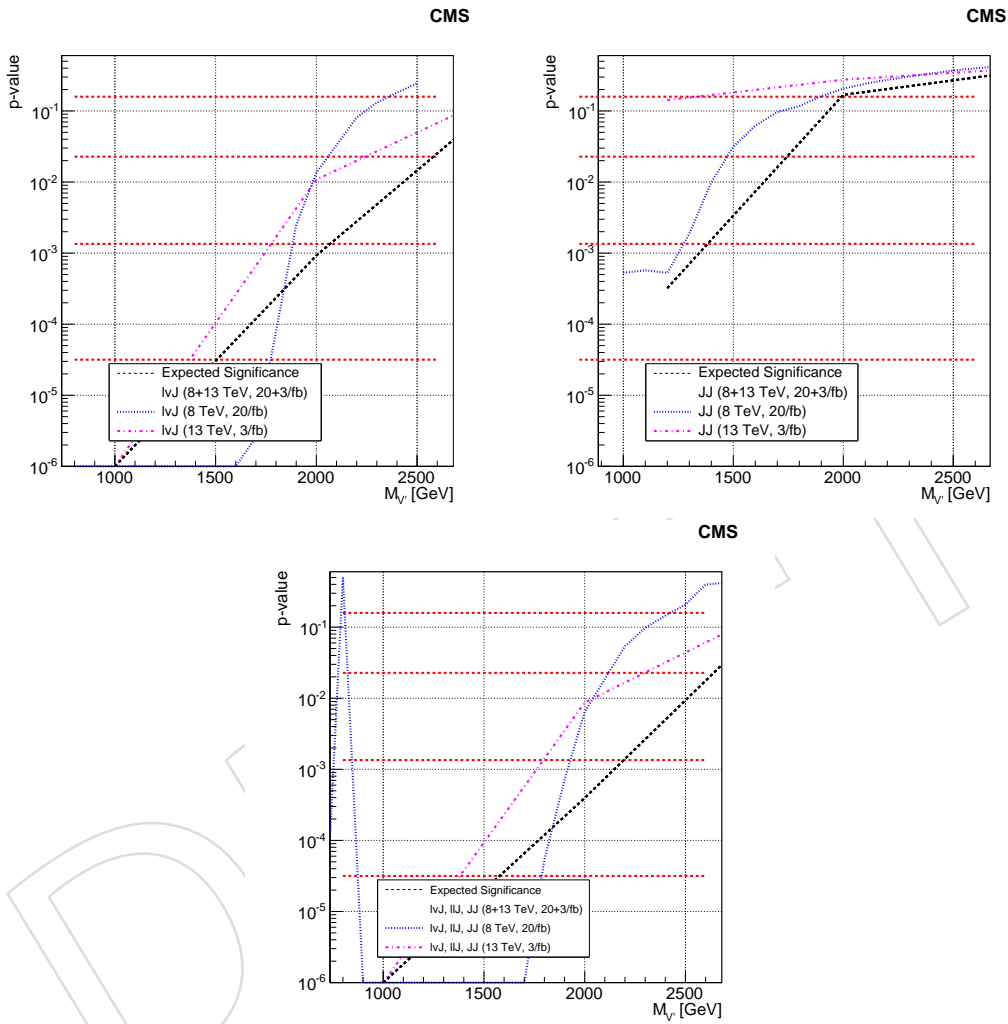


Figure 85: (top-left) Combined expected significance of the $l\nu qq$ analyses using 19.7/fb of 8 TeV data and 3/fb of 13 TeV pseudodata. (top-right) Combined expected significance of the dijet analyses using 19.7/fb of 8 TeV data and 3/fb of 13 TeV pseudodata. (bottom) Combined expected significance of the $l\nu qq$, $ll qq$ and dijet analyses using 19.7/fb of 8 TeV data and 3/fb of 13 TeV pseudodata. The expected significance is shown in the context of the RS1 graviton model.

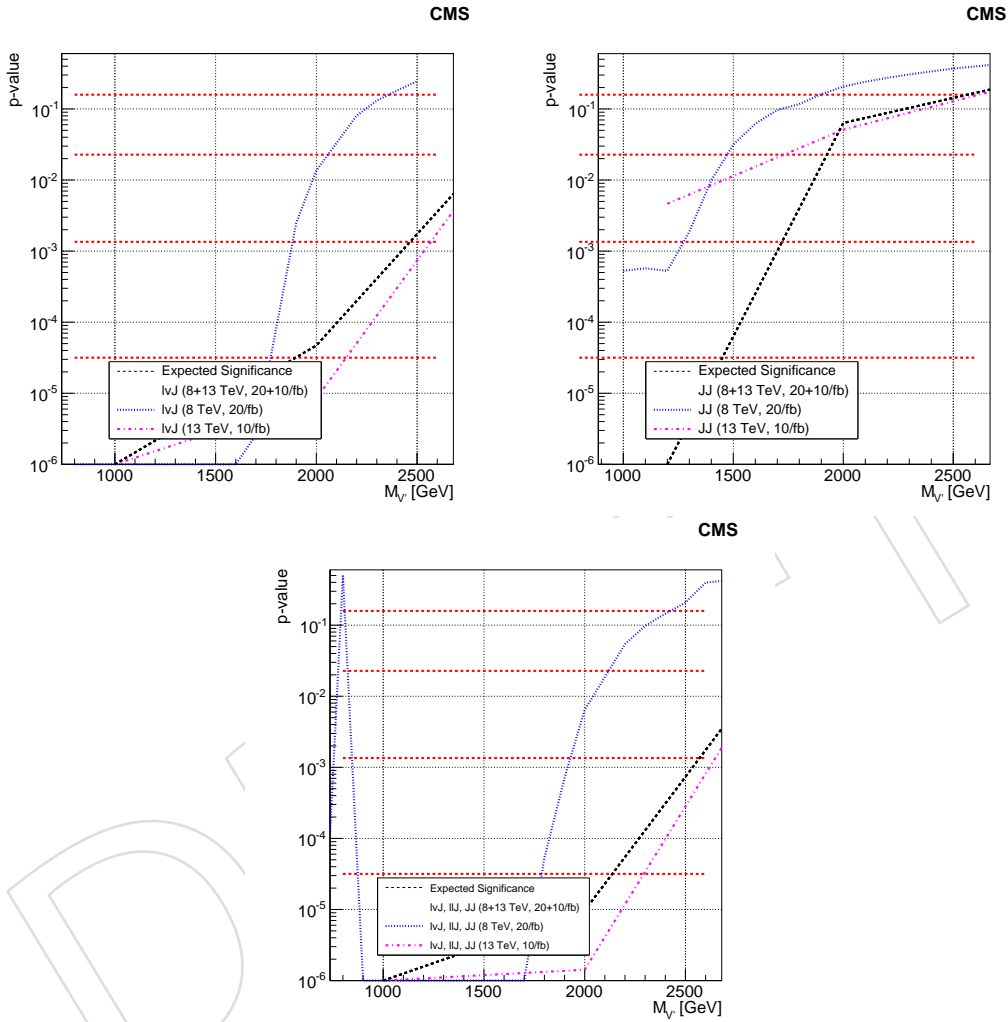


Figure 86: (top-left) Combined expected significance of the $l\nu qq$ analyses using 19.7/fb of 8 TeV data and 10/fb of 13 TeV pseudodata. (top-right) Combined expected significance of the dijet analyses using 19.7/fb of 8 TeV data and 10/fb of 13 TeV pseudodata. (bottom) Combined expected significance of the $l\nu qq$, $llqq$ and dijet analyses using 19.7/fb of 8 TeV data and 10/fb of 13 TeV pseudodata. The expected significance is shown in the context of the RS1 graviton model.

1180 9 Conclusion and Outlook

1181 This note demonstrates that the early analysis effort of the Exotica Diboson group, which
 1182 searches for heavy resonances that decay to a pair of bosons, is well underway. The studies
 1183 shown are based on 13 TeV MC-simulated Phys14 exercise data samples assuming between
 1184 1 fb^{-1} to 10 fb^{-1} . Samples that have not been available so far, in particular for different signal
 1185 models, have been requested. Relevant triggers have been identified and studied. For the all-
 1186 hadronic analysis, the use of jet-substructure triggers in addition to H_T -based triggers extends
 1187 sensitivity to lower resonance masses by about 100 GeV. For the leptonic analyses, non-isolated
 1188 lepton triggers are employed, where for the VZ analysis also dilepton triggers are under eval-
 1189 uation since they allow the use of lower thresholds. The lepton objects used in the analyses are
 1190 optimised for high transverse momenta and energies using the recommendations by the POGs.
 1191 In both leptonic channels, isolation and ID criteria are adjusted to recover efficiency losses in
 1192 the vicinity of another lepton. For trigger, lepton ID, and isolation efficiencies, preparations
 1193 are being made to measure scale factors to correct differences in data and simulation. Jet re-
 1194 construction and b-jet identification profit from the developments performed during LS1, thus
 1195 their working points were re-evaluated. In the VW analysis, events with additional b-tagged
 1196 jets are vetoed in order to reduce $t\bar{t}$ and single top contributions in the signal region. In addition
 1197 a top mass veto is introduced, that can improve sensitivity compared to the Run 1 analysis.

1198 The leptonic W boson candidate is reconstructed by solving the lepton-neutrino system for
 1199 the longitudinal component of the neutrino's momentum exploiting the known W mass. The
 1200 hadronic V candidate is identified using W/Z-tagging, making use of the substructure of the
 1201 jet formed from the merged quark pair. Both jet pruning and the soft drop algorithms are under
 1202 evaluation to reconstruct the V boson mass; the latter brings better properties from the theo-
 1203 retical point of view, while giving similar performance. Furthermore, N-subjettiness is used to
 1204 suppress QCD multijet background, which is optimised for the different analyses. Steps are
 1205 being taken in order to measure the W/Z tagging performance in a $t\bar{t}$ enriched sample in data.
 1206 Sidebands in the hadronic V mass are used to either cross-check or estimate the background
 1207 contributions in the signal region. Both low and high sideband regions have been optimised.
 1208 Particular care is taken not to unblind the Higgs boson mass region when defining signal and
 1209 sideband regions in order to allow for later combination with analyses considering interme-
 1210 diate Higgs bosons. Since this note only documents the early analysis efforts, no long term
 1211 prospects are discussed. However, adding VBF categorisation and also the VH and HH chan-
 1212 nels are planned for Run 2, and are being worked on.

1213 For the background estimation, the alpha method, which is based on the ratio of the resonance
 1214 invariant mass distributions in signal and sideband region, is the method of choice of the lep-
 1215 tonic analyses. The hadronic analysis – and also the leptonic analyses as cross check – use the
 1216 so-called dijet method, which is essentially a smoothness test of the observed data. For the
 1217 interpretation of results, particular focus is being put on the theoretical context. Limits will be
 1218 provided in three different models, namely the RS graviton, the Bulk graviton and the Heavy
 1219 Vector Triplet models. In the long run, model-independent limits, and also resonance-width
 1220 dependent limits will be provided. Tools are in place to combine the Run1 results with Run2
 1221 data and also to combine the different analysis channels. This is of paramount importance in
 1222 case of evidence for an excess with a few fb^{-1} of data. A strategy has been defined for that
 1223 scenario, and also in the likely case that 25 ns and 50 ns have to be combined. Finally, we draw
 1224 attention again to the fact that the Run 1 analyses uncovered a small excess around the region
 1225 of 1.8TeV in all three channels. The excess is relatively consistent amongst the three analyses,
 1226 and is the primary allure of the repetition of this study with the Run 2 data. The possibility to
 1227 combine all available data may indeed be the difference between another excess in a limit plot
 1228 and a real evidence/discovery scenario.

1229 References

- 1230 [1] L. Randall and R. Sundrum, "Large Mass Hierarchy from a Small Extra Dimension",
1231 *Phys.Rev.Lett.* **83** (1999) 3370–3373, doi:10.1103/PhysRevLett.83.3370,
1232 arXiv:hep-ph/9905221.
- 1233 [2] L. Randall and R. Sundrum, "An Alternative to Compactification", *Phys.Rev.Lett.* **83**
1234 (1999) 4690–4693, doi:10.1103/PhysRevLett.83.4690, arXiv:hep-th/9906064.
- 1235 [3] K. Agashe, H. Davoudiasl, G. Perez, and A. Soni, "Warped Gravitons at the LHC and
1236 Beyond", *Phys.Rev.* **D76** (2007) 036006, doi:10.1103/PhysRevD.76.036006,
1237 arXiv:hep-ph/0701186.
- 1238 [4] A. L. Fitzpatrick, J. Kaplan, L. Randall, and L.-T. Wang, "Searching for the Kaluza-Klein
1239 Graviton in Bulk RS Models", *JHEP* **0709** (2007) 013,
1240 doi:10.1088/1126-6708/2007/09/013, arXiv:hep-ph/0701150.
- 1241 [5] O. Antipin, D. Atwood, and A. Soni, "Search for RS gravitons via W(L)W(L) decays",
1242 *Phys.Lett.* **B666** (2008) 155–161, doi:10.1016/j.physletb.2008.07.009,
1243 arXiv:0711.3175.
- 1244 [6] D. Pappadopulo, A. Thamm, R. Torre, and A. Wulzer, "Heavy Vector Triplets: Bridging
1245 Theory and Data", (2014). arXiv:1402.4431.
- 1246 [7] CMS Collaboration, "The CMS experiment at the CERN LHC", *JINST* **3** (2008) S08004,
1247 doi:10.1088/1748-0221/3/08/S08004.
- 1248 [8] H. Brun, "Follow-Up on the di-muon trigger measurement with the reference trigger
1249 method", presentation, 2013.
- 1250 [9] CMS Collaboration, "Search for massive resonances decaying into pairs of boosted
1251 bosons in semi-leptonic final states at $\sqrt{s} = 8$ TeV", *JHEP* **1408** (2014) 174,
1252 doi:10.1007/JHEP08(2014)174, arXiv:1405.3447.
- 1253 [10] CMS Collaboration Collaboration, "Search for a massive resonance decaying into a Higgs
1254 boson and a W or Z boson in hadronic final states in proton-proton collisions at $\sqrt{s} =$
1255 8 TeV", Technical Report CMS-PAS-EXO-14-009, CERN, Geneva, 2015.
- 1256 [11] E. POG, "HEEP Electron ID and isolation", twiki page, 2015.
- 1257 [12] E. POG, "Cut Based Electron ID for Run 2", twiki page, 2015.
- 1258 [13] E.-V. team, "Search for a BSM resonance decaying to Z vector bosons in the semileptonic
1259 final state", CMS Note 2013/040, 2013.
- 1260 [14] S. Yu, "Configuration file for the muon re-reconstruction", python, 2014.
- 1261 [15] M. POG, "Baseline muon selections", twiki page, 2015.
- 1262 [16] CMS Collaboration Collaboration, "Particle-Flow Event Reconstruction in CMS and
1263 Performance for Jets, Taus, and MET", Technical Report CMS-PAS-PFT-09-001, CERN,
1264 2009. Geneva, Apr, 2009.
- 1265 [17] CMS Collaboration, "Pileup Removal Algorithms".

- [18] M. Cacciari, G. P. Salam, and G. Soyez, "The Anti-k(t) jet clustering algorithm", *JHEP* **0804** (2008) 063, doi:10.1088/1126-6708/2008/04/063, arXiv:0802.1189.
- [19] M. Cacciari, G. P. Salam, and G. Soyez, "FastJet User Manual", *Eur.Phys.J.* **C72** (2012) 1896, doi:10.1140/epjc/s10052-012-1896-2, arXiv:1111.6097.
- [20] JME POG, "Jet Identification: Recommendations for 13TeV data analysis".
- [21] Y. L. Dokshitzer, G. D. Leder, S. Moretti, and B. R. Webber, "Better jet clustering algorithms", *JHEP* **08** (1997) 001, doi:10.1088/1126-6708/1997/08/001, arXiv:hep-ph/9707323.
- [22] M. Wobisch and T. Wengler, "Hadronization corrections to jet cross sections in deep-inelastic scattering", (1998). arXiv:hep-ph/9907280.
- [23] S. D. Ellis, C. K. Vermilion, and J. R. Walsh, "Techniques for improved heavy particle searches with jet substructure", *Phys.Rev.* **D80** (2009) 051501, doi:10.1103/PhysRevD.80.051501, arXiv:0903.5081.
- [24] S. D. Ellis, C. K. Vermilion, and J. R. Walsh, "Recombination Algorithms and Jet Substructure: Pruning as a Tool for Heavy Particle Searches", *Phys.Rev.* **D81** (2010) 094023, doi:10.1103/PhysRevD.81.094023, arXiv:0912.0033.
- [25] M. Dasgupta, A. Fregoso, S. Marzani, and G. P. Salam, "Towards an understanding of jet substructure", *JHEP* **1309** (2013) 029, doi:10.1007/JHEP09(2013)029, arXiv:1307.0007.
- [26] M. Dasgupta, A. Fregoso, S. Marzani, and A. Powling, "Jet substructure with analytical methods", *Eur.Phys.J.* **C73** (2013), no. 11, 2623, doi:10.1140/epjc/s10052-013-2623-3, arXiv:1307.0013.
- [27] A. J. Larkoski, S. Marzani, G. Soyez, and J. Thaler, "Soft Drop", *JHEP* **1405** (2014) 146, doi:10.1007/JHEP05(2014)146, arXiv:1402.2657.
- [28] J. Thaler and K. Van Tilburg, "Maximizing Boosted Top Identification by Minimizing N-subjettiness", *JHEP* **1202** (2012) 093, doi:10.1007/JHEP02(2012)093, arXiv:1108.2701.
- [29] CMS Collaboration, "Determination of Jet Energy Calibration and Transverse Momentum Resolution in CMS", *JINST* **6** (2011) P11002, doi:10.1088/1748-0221/6/11/P11002, arXiv:1107.4277.
- [30] M. Cacciari, G. P. Salam, and G. Soyez, "The Catchment Area of Jets", *JHEP* **04** (2008) 005, doi:10.1088/1126-6708/2008/04/005, arXiv:0802.1188.
- [31] B. POG, "b-Tagging Offline Guide", twiki page, 2014.
- [32] J. Bauer, "Prospects for the Observation of Electroweak Top-Quark Production with the CMS Experiment", phd thesis, 2010.
- [33] J. Ngadiuba, "Code for neutrino longitudinal momentum estimation", c++ code, 2015.
- [34] M. Gouzevitch et al., "Scale-invariant resonance tagging in multijet events and new physics in Higgs pair production", arXiv:1303.6636.

- 1304 [35] CMS Collaboration, “Study of Jet Substructure in pp Collisions at 7 TeV in CMS”, CMS
1305 Physics Analysis Summary CMS-PAS-JME-10-013, 2010.
- 1306 [36] CMS Collaboration Collaboration, “Search for massive WH resonances decaying to $\ell\nu b\bar{b}$
1307 final state in the boosted regime at $\sqrt{s} = 8 \text{ TeV}$ ”, Technical Report CMS-PAS-EXO-14-010,
1308 CERN, Geneva, 2015.
- 1309 [37] G. Punzi, “Sensitivity of Searches for New Signals and Its Optimization”, in *Statistical
1310 Problems in Particle Physics, Astrophysics, and Cosmology*, L. Lyons, R. Mount, and
1311 R. Reitmeyer, eds., p. 79. 2003. arXiv:physics/0308063.
- 1312 [38] B. Bellazzini, C. Csiki, and J. Serra, “Composite Higgses”, *Eur.Phys.J.* **C74** (2014), no. 5,
1313 2766, doi:10.1140/epjc/s10052-014-2766-x, arXiv:1401.2457.
- 1314 [39] R. Contino, D. Pappadopulo, D. Marzocca, and R. Rattazzi, “On the effect of resonances
1315 in composite Higgs phenomenology”, *Journal of High Energy Physics* **2011** (2011), no. 10,
1316 doi:10.1007/JHEP10(2011)081.
- 1317 [40] D. Greco and D. Liu, “Hunting composite vector resonances at the LHC: naturalness
1318 facing data”, *JHEP* **1412** (2014) 126, doi:10.1007/JHEP12(2014)126,
1319 arXiv:1410.2883.
- 1320 [41] M. Schmaltz and D. Tucker-Smith, “Little Higgs review”, *Ann.Rev.Nucl.Part.Sci.* **55**
1321 (2005) 229–270, doi:10.1146/annurev.nucl.55.090704.151502,
1322 arXiv:hep-ph/0502182.
- 1323 [42] N. Arkani-Hamed, A. Cohen, E. Katz, and A. Nelson, “The Littlest Higgs”, *JHEP* **0207**
1324 (2002) 034, doi:10.1088/1126-6708/2002/07/034, arXiv:hep-ph/0206021.
- 1325 [43] G. Altarelli, B. Mele, and M. Ruiz-Altaba, “Searching for new heavy vector bosons in $p\bar{p}$
1326 colliders”, *Zeitschrift fr Physik C Particles and Fields* **45** (1989), no. 1, 109–121,
1327 doi:10.1007/BF01556677.
- 1328 [44] D. Pappadopulo, A. Thamm, R. Torre and A. Wulzer, “Tools for the study of heavy vector
1329 triplets”,
- 1330 [45] H. PAG, “Documentation of the RooStats-based statistics tools for Higgs PAG”, twiki
1331 page, 2015.